

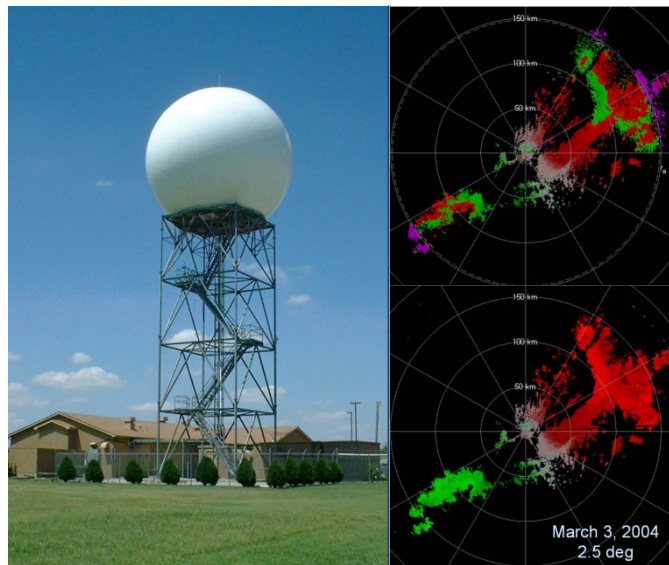
# Signal Design and Processing Techniques for WSR-88D Ambiguity Resolution

## Staggered PRT Updates

### National Severe Storms Laboratory Report

*prepared by:* Sebastian Torres, David Warde, and Dusan Zrnic

**Part 13**  
**January 2010**



National Oceanic and Atmospheric Administration  
National Severe Storms Laboratory  
Norman, Oklahoma 73072



# **SIGNAL DESIGN AND PROCESSING TECHNIQUES FOR WSR-88D AMBIGUITY RESOLUTION**

## **Part 13: Staggered PRT Updates**

National Severe Storms Laboratory Report  
prepared by: Sebastián Torres, David Warde, and Dusan Zrníc

January 2010

NOAA, National Severe Storms Laboratory  
120 David L. Boren Blvd., Norman, Oklahoma 73072



# SIGNAL DESIGN AND PROCESSING TECHNIQUES FOR WSR-88D AMBIGUITY RESOLUTION

## Part 13: Staggered PRT Updates

### Contents

1. Introduction.....	5
2. The Staggered PRT Technique.....	7
3. Recovery of Range-Overlaid Echoes in Staggered PRT .....	9
3.1. Doppler Estimates Beyond $r_{d1}$ .....	9
3.2. Doppler Overlaid Echoes for Segment I and Segment III .....	12
3.3. Threshold Determination for 2/3 SPRT Overlaid Doppler Estimates .....	14
3.3.1. SPRT Velocity Estimate Threshold.....	14
3.3.2. SPRT Spectrum Width Estimate Threshold .....	22
3.4. Real Data Example of Overlaid Recovery of Doppler Estimates in SPRT .....	25
4. Updates to the Staggered PRT Algorithm .....	31
4.1. Incorporating the SACHI Ground Clutter Filter.....	31
4.2. Incorporating Recovery of Range-Overlaid Echoes.....	36
4.2.1. Segment-III Data Reconstruction .....	36
4.2.2. Summary of changes.....	41
5. Volume Coverage Patterns for Staggered PRT .....	43
5.1. Designing VCPs for Staggered PRT.....	43
5.2. Choosing the PRTs .....	44
5.3. Choosing the Dwell Times.....	46
5.4. Examples of VCP Design for Staggered PRT .....	47

5.4.1.	VCP 211 .....	47
5.4.2.	VCP 212 .....	48
5.4.3.	VCP 221 .....	49
5.5.	Summary of Performance and Recommendations.....	56
6.	References.....	59
Appendix A. Staggered PRT Algorithm Description (July 2009).....		65
A.1.	Preface.....	65
A.2.	Assumptions.....	66
A.3.	Inputs.....	66
A.4.	Outputs.....	67
A.5.	Functions and Conventions.....	67
A.6.	High-level Algorithm description.....	69
A.7.	Step-by-step algorithm description.....	70
Appendix B. Bias in differential reflectivity due to cross-coupling through the radiation patterns in the simultaneous horizontal/vertical polarization mode .....		87
B.1.	Abstract .....	87
B.2.	Introduction.....	87
B.3.	Effects of the bias on Rain Rate Measurements.....	91
B.4.	Coupling through the radiation patterns.....	93
B.5.	Alternate Transmit and Simultaneous Receive (AHV) mode.....	109
B.6.	Summary .....	112
B.7.	Appendix: Cross-polar radiation induced by the parabolic reflector .....	114
B.8.	References .....	116
B.9.	List of Figures .....	118
Appendix C. Publications .....		123

# SIGNAL DESIGN AND PROCESSING TECHNIQUES FOR WSR-88D AMBIGUITY RESOLUTION

## **Part 13: Staggered PRT Updates**

### **1. Introduction**

The Radar Operations Center (ROC) of the National Weather Service (NWS) has funded the National Severe Storms Laboratory (NSSL) to address data quality improvements for the WSR-88D. This is the thirteenth report in the series that deals with range and velocity ambiguity resolution in the WSR-88D (other relevant reports are listed at the end). It documents NSSL accomplishments in FY09.

We start in section 2 by providing a brief review of the evolution of the staggered pulse-repetition-time (SPRT) algorithm. Section 3 describes the recovery of range overlaid echoes for the SPRT algorithm. By means of a simple extension, the algorithm can retrieve Doppler estimates to longer ranges. This facilitates the use of shorter PRTs which results in an overall performance improvement and makes the staggered PRT technique operationally feasible for the WSR-88D.

Section 4 is devoted to the latest algorithmic changes to the staggered PRT (SPRT) that were needed to accommodate the SACHI filter for ground clutter suppression and incorporate the recovery of range overlaid echoes. A revised set of criteria that trades-off range coverage for better performance is proposed in section 5 to define effective

scanning strategies that exploit SPRT and contribute to an efficient complete range-and-velocity ambiguity mitigation solution.

This report also includes three appendices. Appendix A contains the latest description of the staggered PRT algorithm that uses the SACHI ground clutter filter and is able to recover range-overlaid echoes. This algorithm description was officially submitted to the ROC in July of 2009. Appendix B examines the bias in differential reflectivity and its effect on estimates of rain rate and hydrometeor classification due to coupling of the vertically and horizontally polarized fields through the radiation patterns. Appendix C includes four relevant conference papers on range and velocity ambiguity mitigation that were presented during this past fiscal year.

Once again, the work performed in FY09 exceeded considerably the allocated budget; hence, a part of it had to be done on other NOAA funds.

## 2. The Staggered PRT Technique

The staggered pulse repetition time (SPRT) algorithm has been shown to mitigate range and velocity ambiguities in Doppler weather radars by decreasing velocity aliasing while extending the radar coverage (Sirmans 1976). Since then, the practical aspect of implementing the SPRT algorithm centered around three major issues: (1) providing adequate clutter filter suppression, (2) resolving overlay echoes, and (3) obtaining quality estimates with low variance. Resolution of the first and third issues (clutter suppression and quality estimates) are detailed in NSSL report 3 (1999) with the introduction of the Spectral Algorithm for Clutter Harmonics Identification (SACHI) filter for a 2/3 PRT ratio. The second issue was mitigated by ensuring the unambiguous range of the shortest PRT ( $r_{a1} = cT_1/2$ ) encompassed the range extent of expected weather.

In subsequent years (NSSL reports 4 through 12), NSSL scientists refined the SPRT algorithm and the SACHI filter to its present state and characterized the algorithm performance and operational suitability for WSR-88D implementation. During this time, the SPRT algorithm took on two forms: time domain processing with a DC-removal filter (Torres 2004, NSSL report 8 2004) and spectral processing with the SACHI filter. In the time-domain algorithm, overlaid power estimates were shown to be resolvable to the unambiguous range of the longest PRT ( $r_{a2} = cT_2/2$ ) as long as the range extent of expected weather was within  $r_{a2}$ . These power estimates could then be used to censor overlaid Doppler estimates within  $r_{a1}$ , while Doppler estimates in the segment between  $r_{a1}$  and  $r_{a2}$  could not be resolved. Meanwhile, the SPRT spectral processing algorithm with the SACHI filter did not allow any overlaid echo resolution.

In this report, section 3 introduces a new technique to resolve Doppler estimates to the maximum extent of  $r_{a2}$  allowing use of shorter PRT sets which in turn provides improved estimate quality. Additionally, section 3 provides overlaid threshold recommendations for Doppler estimates to ensure WSR-88D estimate accuracy. Section 4 merges the two forms of the SPRT algorithm and addresses overlay resolution within the SPRT spectral processing algorithm.

### 3. Recovery of Range-Overlaid Echoes in Staggered PRT

#### 3.1. Doppler Estimates Beyond $r_{a1}$

The current SPRT algorithm uses alternate pulses transmitted at two PRTs ( $T_1$  and  $T_2$ ) with a PRT ratio of  $\kappa = 2/3$  ( $T_1 = \kappa T_2$ ). With the proper choice of  $T_1$  and  $T_2$ , overlaid weather echoes can be avoided as shown in Fig. 3.1a. Overlaid echoes are allowed to extend beyond the receive time of  $T_1$  (Fig. 3.1b), but not beyond the receive time of  $T_2$  (Fig. 3.1c). The two receive times can be broken into segments that are half of the receive time of  $T_1$ . Thus, two segments (I and II) are created within the  $T_1$  receive time, and three segments (I, II, and III) are created within the  $T_2$  receive time. Note in Fig. 3.1b that during receive time for segment II in both  $T_1$  and  $T_2$  there are no overlaid echoes. Additionally, in Fig. 3.1b, there are no overlaid echoes in segment I for  $T_1$  and segment III for  $T_2$ . This fact allows the weather signal power (reflectivity) to be recovered unambiguously in all three segments. That is, the signal power estimate is recoverable to the maximum extent of the unambiguous range of  $T_2$  ( $r_{a2}$ ) without overlaid echoes biasing the estimates. Consequently, power estimates are a useful means of determining the amount of overlay that occurs in segment I and segment III (Torres 2004).

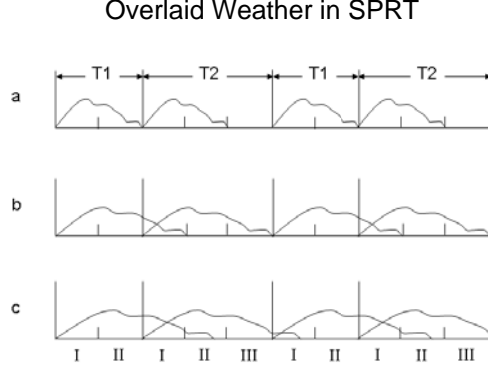


Fig. 3.1. The 2/3 SPRT sequence is divided into segments to show how overlaid echoes overlay into the two receive times ( $T_1$  and  $T_2$ ). (a) The weather extent is contained within  $r_{a1}$  and no echoes are overlaid. (b) The weather extent is contained within  $r_{a2}$  and some overlaid echoes are present in segment I of  $T_2$ . (c) The weather extent is beyond  $r_{a2}$  and overlaid echoes are present in segment I of  $T_1$  as well as segments I and II of  $T_2$ .

In the SPRT algorithm, Doppler moments for segments I and II are calculated from the lag-one autocorrelation between matching range gates occurring in the receive times of  $T_1$  and  $T_2$ . The two autocorrelations are constructed as:

$$R_{T_1, T_2}(n, 1) = \frac{2}{M} \sum_{m=0}^{M/2-1} V^*(n, 2m) V(n, 2m+1) \quad (1.1)$$

$$R_{T_2, T_1}(n, 1) = \frac{2}{M-2} \sum_{m=0}^{M/2-2} V^*(n, 2m+1) V(n, 2m+2) \quad (1.2)$$

Where the  $xx$  in  $R_{xx}$  is the lag-one autocorrelation from pulse to pulse (i.e., equation (3.1) is from pulse  $T_1$  to pulse  $T_2$  and equation (3.2) is from pulse  $T_2$  to pulse  $T_1$ ),  $n$  is the range gate index within  $r_{a1}$ ,  $M$  is the number of pulse samples,  $V$  is the received complex voltage, and  $m$  is the pulse index. For the sake of simplicity, we assume that the sequence of pulses starts with  $T_1$  and  $M$  is even.

Observing that the overlaid echoes (i.e., echoes from  $T_1$  transmitted pulses are returned during  $T_2$  receive time) in segment I of  $T_2$  and the received echoes in segment III of  $T_2$  are from the same weather event, Warde and Torres (2009) show how segment III Doppler estimates can be recovered using another set of lag-one autocorrelations constructed in range and across receive times of  $T_2$  as:

$$R_{T_2, T_2}(n, 1) = \frac{2}{M-2} \sum_{m=0}^{M/2-2} V^*(n - N_1, 2m+1)V(n, 2m+1) \quad (1.3)$$

$$R_{T_2, T_2}(n, 1) = \frac{2}{M-4} \sum_{m=0}^{M/2-3} V^*(n, 2m+1)V(n - N_1, 2m+3) \quad (1.4)$$

Here, all variables are as in equations (3.1) and (3.2), except that  $n$  is restricted to range gates occurring in segment III of receive time  $T_2$  and  $N_1$  is the total number of range gates in  $T_1$  (not necessarily the number of gates available for processing). Note that equation (3.3) is an autocorrelation in range (segment I to segment III of  $T_2$  receive times); whereas, equation (3.4) is an autocorrelation in range and across  $T_2$  receive times (segment III to segment I of consecutive  $T_2$  receive times). All four autocorrelations are illustrated in Fig. 3.2.

## Range Overlaid SPRT Autocorrelations

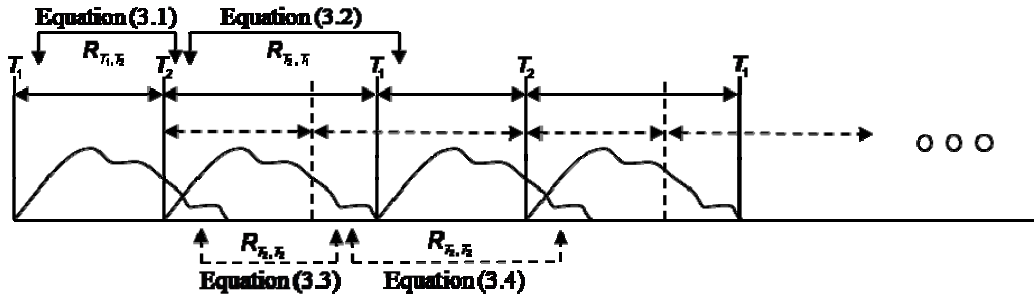


Fig. 3.2. Illustration of the 2/3 SPRT autocorrelations with overlaid echoes. Typical autocorrelations (e.g. equations 3.1 and 3.2) are formulated between consecutive pulses as shown at the top. SPRT range-overlaid autocorrelations (e.g. equations 3.3 and 3.4) are formulated in range and across  $T_2$  pulses as shown at the bottom.

### 3.2. Doppler Overlaid Echoes for Segment I and Segment III

From Fig. 3.1b, it is seen that only the segment I pulses from  $T_2$  can be overlaid. In the segment I autocorrelations from (3.1) and (3.2), the odd pulses ( $2m$  and  $2m + 2$  with zero-based indexing) are from segment I of  $T_1$  and the even pulses are from segment I of  $T_2$ . In the segment III autocorrelations from equations (3.3) and (3.4), all the pulses are from  $T_2$  with overlaid echoes occurring only in the range gates in segment I ( $n - N_1$ ) but not the range gates in segment III ( $n$ ). An instructive way to visualize overlaid echoes in SPRT using a 2/3 PRT ratio is to consider two overlaid kernels. Recall that the SPRT kernel  $[1, 0, 1, 0, 0]$  represents the smallest periodic sampling of the weather signal voltages with PRTs  $T_1$  and  $T_2$  when placed in the appropriate time slots corresponding to uniform sampling with PRT  $T_u = T_2 - T_1$  (e.g., Sachidananda and Zrnić 2003). In the SPRT kernel, a 1 represents the presence of a sample and a 0 represents the absence of a sample. In this way, the SPRT time-series data can be seen as the product of the periodic extension of

the SPRT kernel with a sequence of uniformly sampled voltages at a PRT equal to  $T_u$ . Likewise, from equations (3.1) and (3.3) we can construct one overlaid kernel as  $[0, 0, 1, 0, 0]$  and from equations (3.2) and (3.4) we can construct another overlaid kernel as  $[1, 0, 0, 0, 0]$ . In these overlaid kernels, a 1 represents the presence of an overlaid echo; whereas, a 0 represents no overlaid echo or the absence of a sample.

Next, we can compare the overlaid kernels to the SPRT kernel. It is easy to see that only half the power of overlaid echoes contaminates the Doppler estimates (i.e. every other pulse is contaminated by overlaid echoes). Further, comparing the power spectra of the three kernels, it is seen that both overlaid kernel spectra are evenly distributed across the SPRT kernel spectrum. In Fig. 3.3, the SPRT kernel spectrum (blue) is contrasted against the two overlaid kernel spectra (red). Note that both overlaid kernels have the same power spectrum and that the power in the central coefficient of the SPRT kernel is 6 dB greater than any of the overlaid kernel coefficients.

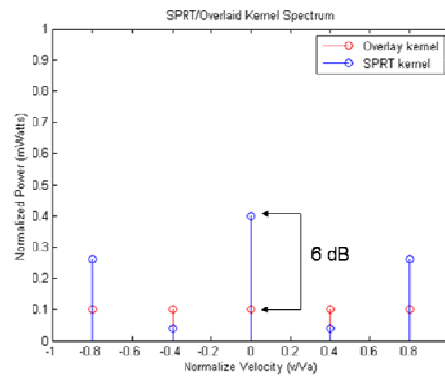


Fig. 3.3. Power spectra of SPRT kernel  $[1, 0, 1, 0, 0]$  (blue) and overlaid kernels  $[1, 0, 0, 0, 0]$  and  $[0, 0, 1, 0, 0]$  (red). Note that the power spectra of the overlaid kernels are the same and are evenly distributed across the Nyquist co-interval; whereas most of the SPRT kernel power spectra is concentrated at the true velocity (0 in this case) and is 6 dB greater than the overlaid echo spectra.

### 3.3. Threshold Determination for 2/3 SPRT Overlaid Doppler Estimates

#### 3.3.1. SPRT Velocity Estimate Threshold

Consider the fractional velocity bias ( $\varepsilon$ ), fractional velocity difference ( $\Delta v$ ), and composite normalized velocity estimate ( $E[v]/v_a$ ) associated with overlaid echoes in a uniformly sampled environment as (Sirmans and Bumgarner 1990):

$$\varepsilon = \left| \frac{\bar{v}_1 - E[v]}{v_a} \right|, \quad (1.5)$$

$$\Delta v = \left| \frac{\bar{v}_1 - \bar{v}_2}{v_a} \right| \quad (1.6)$$

$$\frac{E[v]}{v_a} = \frac{1}{\pi} \tan^{-1} \left[ \frac{\rho_1 \sin\left(\frac{\bar{v}_1}{v_a} \pi\right) + \rho_2 \sin\left(\frac{\bar{v}_2}{v_a} \pi\right)}{\rho_1 \cos\left(\frac{\bar{v}_1}{v_a} \pi\right) + \rho_2 \cos\left(\frac{\bar{v}_2}{v_a} \pi\right)} \right] \quad (1.7)$$

where a subscript of 1 indicates the signal with the stronger power, a subscript of 2 indicates the signal with the weaker power,  $\bar{v}_x$  is the mean velocity of the signal,  $E[v]$  is the estimate of the velocity for the composite signal,  $v_a$  is the Nyquist velocity,  $\rho_x = e^{-\left(\frac{\pi w_x}{\sqrt{2} v_a}\right)}$  is the correlation coefficient, and  $w_x$  is the spectrum width of the signal. In equations (3.5) through (3.7), it can be seen that the fractional velocity bias is dependent on the velocity difference, the power ratio, the spectrum width of the two overlaid signals, and, indirectly, the PRT which determines the Nyquist velocity. In their report, Sirmans and Bumgarner used a Nyquist velocity of 25 m/s as a benchmark. As an

example, Fig. 3.4 shows the theoretical velocity bias (left) and fractional velocity bias (right) as a function of the fractional velocity difference for overlaid power ratios (strongest to weakest) of 0.1, 1.0, 3.0, 5.0, 10.0, and 15 dB. In this example, an overlaid power ratio of at least 10 dB is needed to maintain the velocity bias below 1 m/s. Note that the velocity bias for any overlaid situation of equal spectrum widths would produce the same curves as in Fig. 3.4. In fact, the curves in Fig. 3.4 match exactly the curves in Fig. 1 of Sirmans and Bumgarner's report (1990) for equal spectrum widths of 2 m/s. Additionally, it should be noted that a higher Nyquist velocity (i.e., shorter PRTs) requires higher thresholds to maintain the same bias levels. Even so, Sirmans and Bumgarner concluded that reasonable Doppler velocity estimates could be obtained as long as the stronger signal was between 5 dB and 10 dB stronger than the weaker signal. Accordingly, the overlaid threshold value used in the WSR-88D for uniformly sampling was established at 5 dB. Observe in Fig. 3.4 that for a power ratio of 5 dB, the maximum velocity bias is about 2.5 m/s when the Nyquist is 25 m/s.

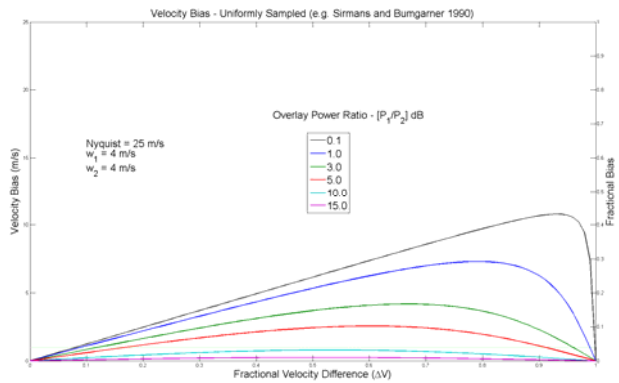


Fig. 3.4. Velocity bias for overlaid echoes with uniform sampling as a function of the fractional velocity difference:  $\left|(\bar{v}_1 - \bar{v}_2)/v_d\right|$ . The fractional bias is shown on the right and an example of velocity bias with a Nyquist velocity of 25 m/s is shown on the left. The velocity bias for power ratios (strongest to weakest) of 0.1, 1.0, 3.0, 5.0, 10.0 and 15.0 dB are given.

Sirmans and Bumgarner did not assess the standard deviation of velocity ( $SD[v]$ ) associated with overlaid echoes. Nevertheless, simulations shown in Fig. 3.5 point out that the  $SD[v]$  increases to about 2.3 m/s for the maximum absolute velocity difference for the benchmark Nyquist of 25 m/s and a power ratio of 5 dB when each echo has the same spectrum width of 4 m/s. Fig. 3.5 shows the plots of the velocity bias (top),  $SD[v]$  (middle), and percent of alias velocity occurrence (bottom) for two simulated overlaid signals. The plots were created using normal distributions for both signals at different power ratios ( $P_1/P_2$ ) of 0.0, 5.0, and 10.0 dB. The first signal (subscript 1) is held stationary at 0 m/s with spectrum width of 4 m/s, while the second signal (subscript 2) is made to increase in velocity from 0 m/s to 25 m/s and has a spectrum width of 4 m/s. In this way, the absolute velocity difference increases from 0 m/s to 25 m/s. The estimated velocity biases (top) of Fig. 3.5 match the theoretical velocity biases in Fig. 3.4 for like power ratios. Note that the  $SD[v]$  (middle) shows an increase in error as the absolute velocity difference increases. As expected by the sampling theorem, the occurrence of velocity aliasing increases abruptly when the absolute velocity difference nears the Nyquist velocity of 25 m/s. This behavior is due to signal 2 aliasing as its mean velocity nears the Nyquist velocity and would occur at another point if signal 1 velocity were not at 0 m/s.

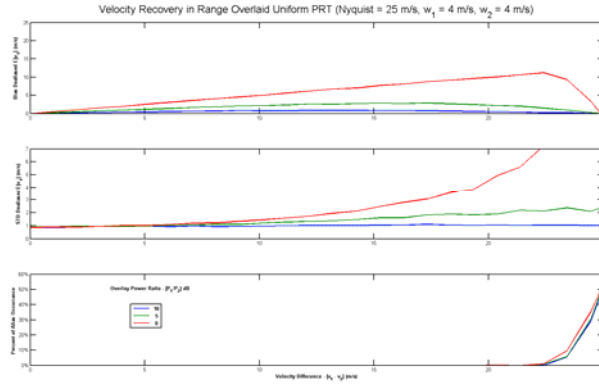


Fig. 3.5. Velocity bias (top), standard deviation of velocity (middle), and percent of aliasing occurrences (bottom) for overlaid echoes as a function of the absolute velocity difference ( $|v_1 - v_2|$ ). A Nyquist velocity of 25 m/s, power ratios (strongest to weakest) of 0, 5.0, and 10.0 dB and equal spectrum widths of 4 m/s are shown.

Because overlaid echoes are uniformly distributed across the SPRT spectrum, there is no velocity bias when recovering Doppler estimates in overlaid regions; however, aliasing does occur. Torres et al. (2004) noted that not all SPRT velocity aliasing was the typical aliasing at twice the SPRT extended Nyquist velocity ( $v_a$ ) as described by the sampling theorem. On occasion, SPRT velocity estimates alias by a factor of  $v_a/2$ . They coined the term "catastrophic errors" for these SPRT aliasing occurrences. Because of "catastrophic errors" in SPRT, Torres et al. (2009) recommended updates to the dealiasing rules in the WSR-88D Radar Product Generation (RPG) subsystem that mitigate these dealiasing errors.

The occurrence of "catastrophic errors" in SPRT is directly related to the variance of the short- and long-PRT velocity estimates and is exacerbated in overlaid echo regions. Fig. 3.6 shows plots of the dealiased velocity bias (top),  $SD[v]$  (middle), and percent of alias velocity occurrence (bottom) for two overlaid signals in SPRT (i.e., overlaid echoes in segment I or segment III). The plots were created using normal distributions for both

signals at different power ratios ( $P_1/P_2$ ). Just as with uniform sampling, the first signal is held stationary at 0 m/s with spectrum width of 4 m/s, while the second signal is made to increase in velocity from 0 m/s to 50 m/s and has a spectrum width of 4 m/s. In this way, the absolute velocity difference increases from 0 m/s to 50 m/s. The top plot in Fig. 3.6 shows the dealiased velocity bias with "catastrophic errors" dealiased at  $v_a/2$ , the middle plot shows the  $SD[v]$ , and the bottom plot shows the percent of velocity aliasing occurrences.

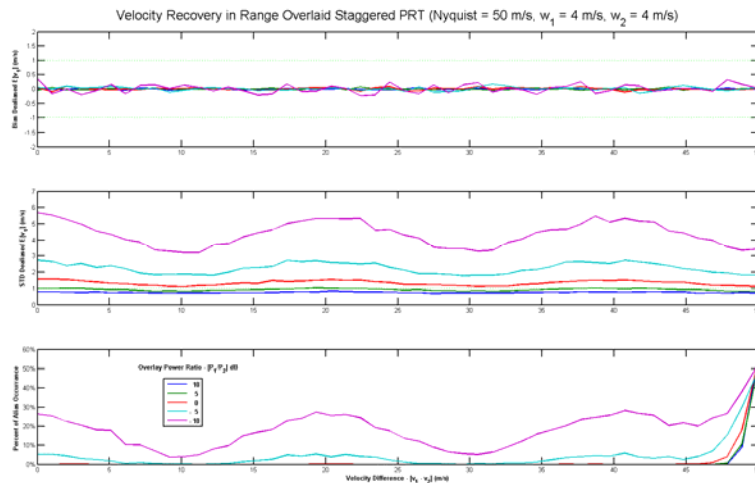


Fig. 3.6. Velocity bias (top), standard deviation (middle), and percent of aliasing occurrences (bottom) for overlaid echoes with SPRT sampling as a function of the velocity difference ( $|\bar{v}_1 - \bar{v}_2|$ ). An extended Nyquist velocity of 50 m/s for power ratios (strongest to weakest) of 0,  $\pm 5.0$ , and  $\pm 10.0$  dB with both signals having equal spectrum widths of 4 m/s are shown.

As expected, no velocity bias occurs in SPRT for any of the power ratios shown. However, observe that the  $SD[v]$  and the percent of alias occurrences increase as the power ratio decreases. Also note the increase in errors at absolute velocity difference of 0, 20, and 40 m/s (with minimums at 10, 30 and 50 m/s); these increased errors occur at absolute velocity differences of 0, 0.4, and 0.8 of the normalized Nyquist co-interval. This cyclic (5 times within the Nyquist co-interval) increase and decrease in errors is

noteworthy since the maxima coincides with the SPRT kernel spectra and the overlaid kernel spectra occurring at the same coefficients; while the minima coincides with the kernel spectra having maximum divergence. The cyclic behavior is attributed to the overlaid kernel equally distributed between the coefficients at  $0.0 + v_2/v_a$ ,  $\pm 0.4 + v_2/v_a$ , and  $\pm 0.8 + v_2/v_a$  of the normalized Nyquist co-interval where  $v_2$  is velocity of the overlaid echo.

Sirmans and Bumgarner (1990) considered the effects of different meteorological overlaid situations such as convective storms overlaid with clutter, clear air, stratiform rain, convective, and severe convective using uniform sampling. For SPRT, Fig. 3.7 through 3.10 show the effects of mixed overlaid situations when the overlaid echo spectrum width is not the same as the signal being measured. Fig. 3.7 shows clutter (spectrum width of 0.5 m/s) overlaid on a convective storm (spectrum width of 4 m/s). Note that at power ratios above 0 dB, overlaid clutter contamination maintains the  $SD[v]$  below 2 m/s. As in the clutter contamination case,  $SD[v]$  can be maintained below 2 m/s for power ratios at 0 dB and above when either clear air (spectrum width of 1 m/s, Fig. 3.8) or stratiform rain (spectrum width of 2 m/s, Fig. 3.9) returns are overlaid onto a convective storm. It is interesting to note (e.g., Fig. 3.6 through 3.9) that as the overlaid signal becomes narrower compared to the non-overlaid signal, the cyclic maxima and minima become more pronounced. Now, observe in Fig. 3.10 that when a severe convective return (spectrum width of 8 m/s) overlays a convective storm, the cyclic effect disappears. The behavior of wide spectrums to flatten the  $SD[v]$  is attributed to the overlap of the five spectra of the overlaid signal with each other.

The WSR-88D system specification requires the  $SD[v]$  to be maintained at or below 1 m/s for a true spectrum width of 4 m/s. For overlaid clutter contamination, clear air, stratiform rain, convective, and severe convective echoes, a power ratio of at least 5 dB (dark green) or greater is needed to meet this requirement for a 50 m/s extended Nyquist velocity. The simulation results shown in Fig. 3.6 through 3.10 indicate that a power ratio of 0 dB (red line) performs very well and is comparable to the overlaid threshold for velocity recovery operationally used on the WSR-88D with uniform sampling. That is, a power ratio of 0 dB allows the  $SD[v]$  with SPRT to be equal to or less than 1 m/s when applying the same Nyquist benchmark of 25 m/s (used in establishing the uniform overlaid threshold).

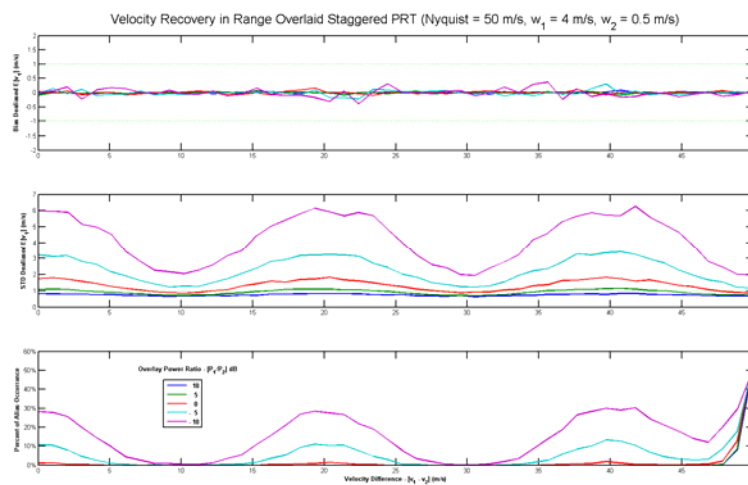


Fig. 3.7. Same as Fig. 3.6 but signal 1 has a spectrum width of 4 m/s and signal 2 (overlaid echo) has a spectrum width of 0.5 m/s (representative of low level range overlaid ground clutter contamination on a convective storm).

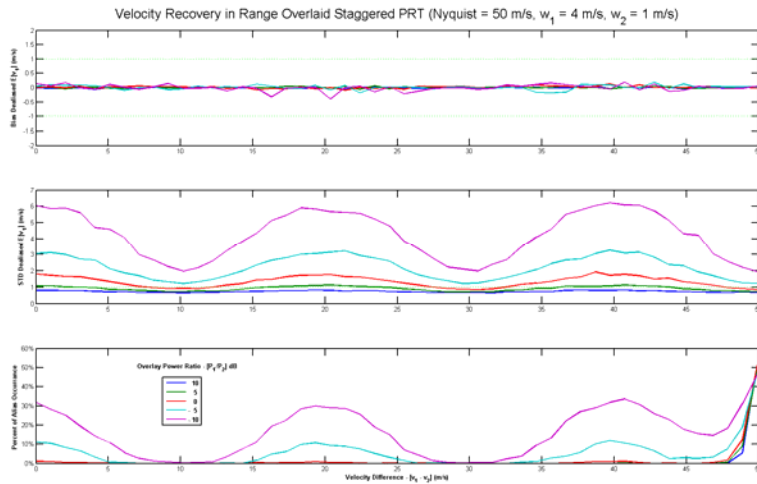


Fig. 3.8. Same as Fig. 3.6 but signal 1 has a spectrum width of 4 m/s and signal 2 (overlaid echo) has a spectrum width of 1.0 m/s (representative of range overlaid clear air return on a convective storm).

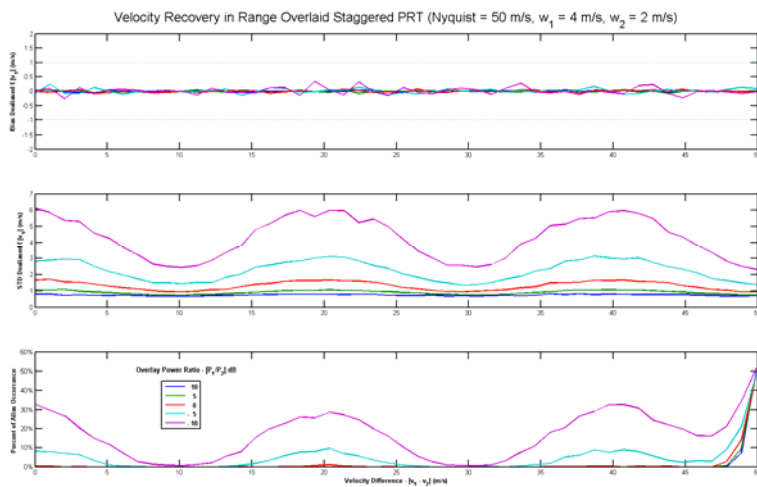


Fig. 3.9. Same as Fig. 3.6 but signal 1 has a spectrum width of 4 m/s and signal 2 (overlaid echo) has a spectrum width of 2.0 m/s (representative of range overlaid stratiform rain return on a convective storm).

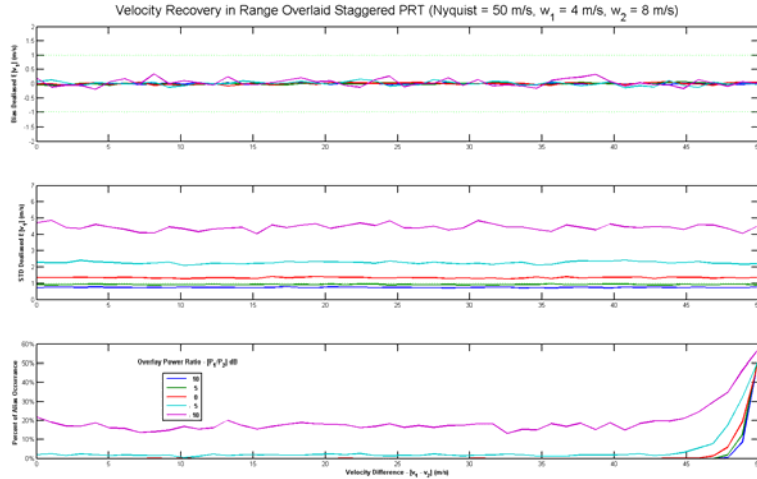


Fig. 3.10. Same as Fig. 3.6 but signal 1 has a spectrum width of 4 m/s and signal 2 (overlaid echo) has a spectrum width of 8.0 m/s (representative of range overlaid severe convective storm return on a convective storm).

### 3.3.2. SPRT Spectrum Width Estimate Threshold

Although the WSR-88D uses the same overlaid threshold (5 dB) for both velocity and spectrum width, Sirmans (1998) found that an overlaid power ratio of 20 dB was needed to maintain the standard deviation of spectrum width ( $SD[w]$ ) at or below 1 m/s. Presented in Fig. 3.11 through 3.15 are the effects of different meteorological overlaid situations for SPRT. As before, when establishing a threshold for overlaid spectrum width estimates, simulations of a convective storm echo are overlaid with clutter (Fig. 3.11), clear air (Fig. 3.12), stratiform rain (Fig. 3.13), convective (Fig. 3.14), and severe convective returns (Fig. 3.15). These figures show the bias (top) and the standard deviation (bottom) of spectrum width estimates as a function of the velocity difference (same as before). These plots show that the spectrum width is not biased for any power ratio, but the  $SD[w]$  increases as the power ratio decreases. Similar oscillations are observed for the  $SD[w]$  as were observed for the  $SD[v]$ . To maintain  $SD[w]$  at or below the 1 m/s requirement established for the WSR-88D and using a 25 m/s benchmark as

before, a power ratio of about 10 dB is needed. However, if operationally acceptable, a power ratio of about 5 dB will maintain  $SD[w]$  at or below 2 m/s.

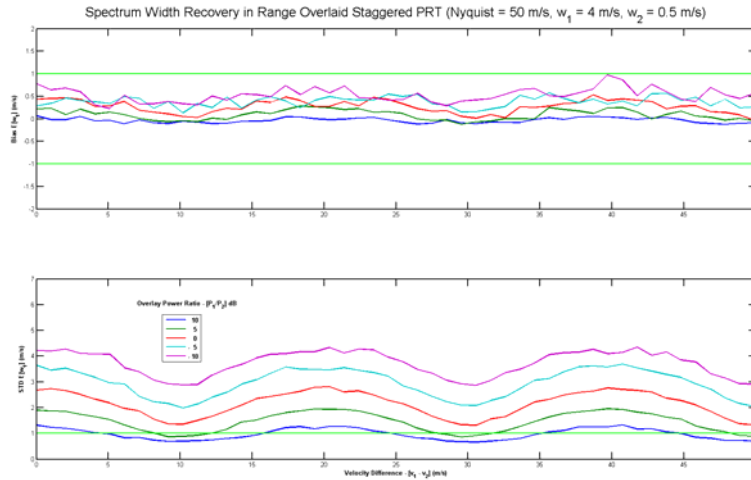


Fig. 3.11. Spectrum width bias (top) and standard deviation (bottom) for overlaid echoes with SPRT as a function of the velocity difference ( $|(\bar{v}_1 - \bar{v}_2)|$ ). An extended Nyquist velocity of 50 m/s for power ratios (strongest to weakest) of 0,  $\pm 5.0$ , and  $\pm 10.0$  dB. Signal 1 has a spectrum width of 4 m/s and signal 2 (overlaid echo) has a spectrum width of 0.5 m/s (representative of low level range overlaid ground clutter contamination on a convective storm).

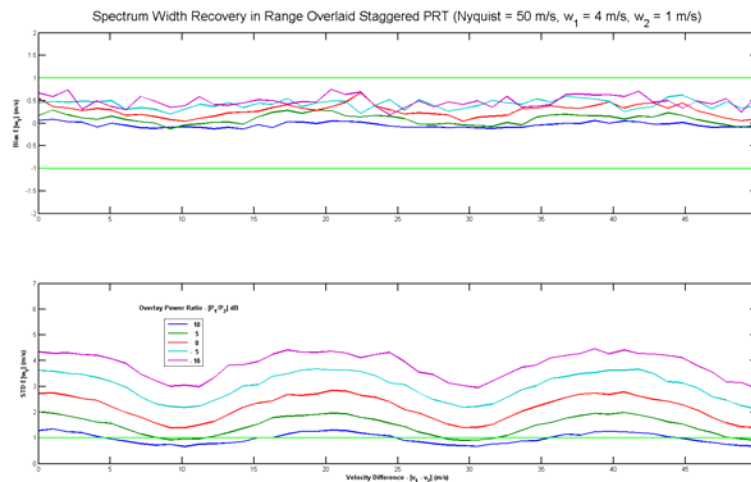


Fig. 3.12. Same as Fig. 3.11 but signal 1 has a spectrum width of 4 m/s and signal 2 (overlaid echo) has a spectrum width of 0.5 m/s (representative of range overlaid clear air return on a convective storm).

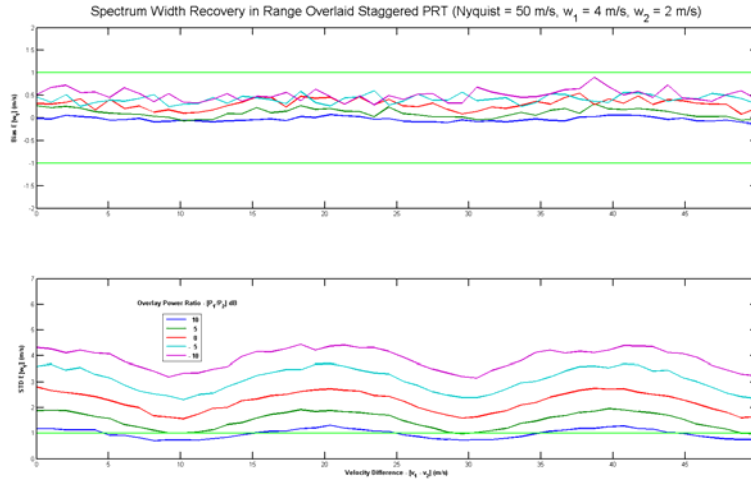


Fig. 3.13. Same as Fig. 3.11 but signal 1 has a spectrum width of 4 m/s and signal 2 (overlaid echo) has a spectrum width of 2 m/s (representative of range overlaid stratiform rain return on a convective storm).

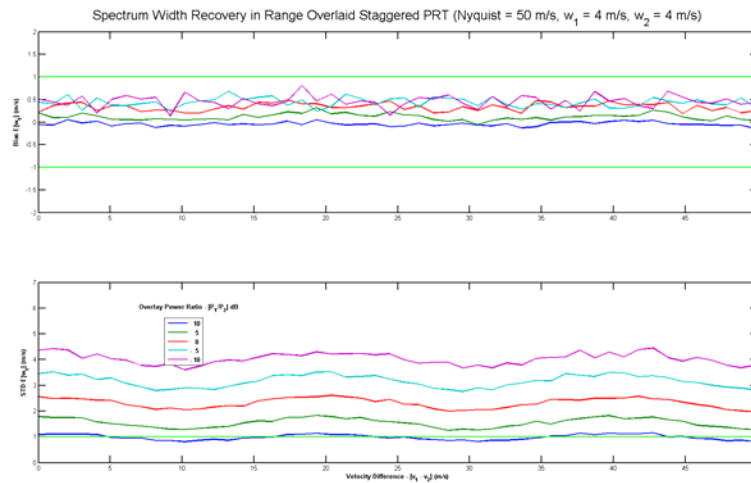


Fig. 3.14. Same as Fig. 3.11 but signal 1 has a spectrum width of 4 m/s and signal 2 (overlaid echo) has a spectrum width of 4.0 m/s (representative of range overlaid convective storm return on a convective storm).

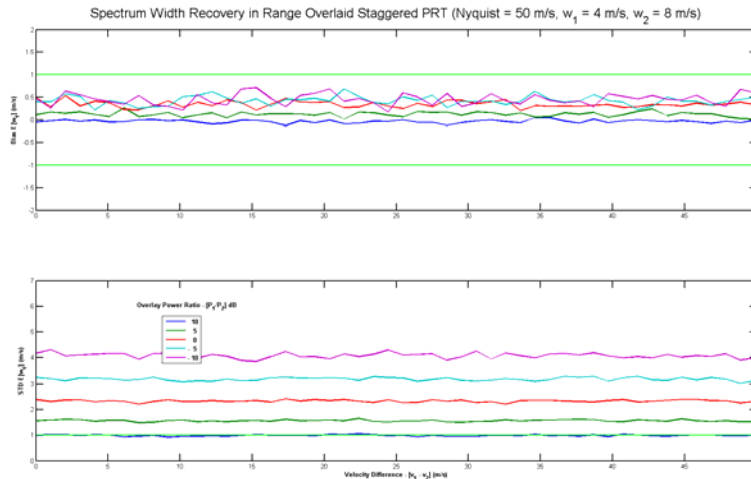


Fig. 3.15. Same as Fig. 3.11 but signal 1 has a spectrum width of 4 m/s and signal 2 (overlaid echo) has a spectrum width of 8.0 m/s (representative of range overlaid severe convective storm return on a convective storm).

### 3.4. Real Data Example of Overlaid Recovery of Doppler Estimates in SPRT

The Staggered PRT algorithm with ground clutter filtering and overlaid echo recovery (Torres and Warde 2009) was implemented in MATLAB to allow reprocessing of time series data. SPRT time series collected from KOUN on June 26, 2003 using experimental volume coverage pattern VCP45b (detailed in NSSL report 7 2003) was replayed through the MATLAB implementation of the new SPRT algorithm. Although not recommended for operational use, SPRT data was collected at an elevation of  $1.45^\circ$  to provide weather estimates beyond  $r_{a1}$ . An example of the reflectivity PPI is shown in Fig. 3.16. Note the ring of no data in the display at the segment II/III boundaries. This ring is due to missing data at the end of  $T_1$  receive time and occurs during the receiver protect time of the WSR-88D when the receiver is desensitized. Special attention may be required in the practical implementation of the SPRT algorithm on the WSR-88D to account for missing data that may occur at the end of  $r_{a1}$  and  $r_{a2}$ .

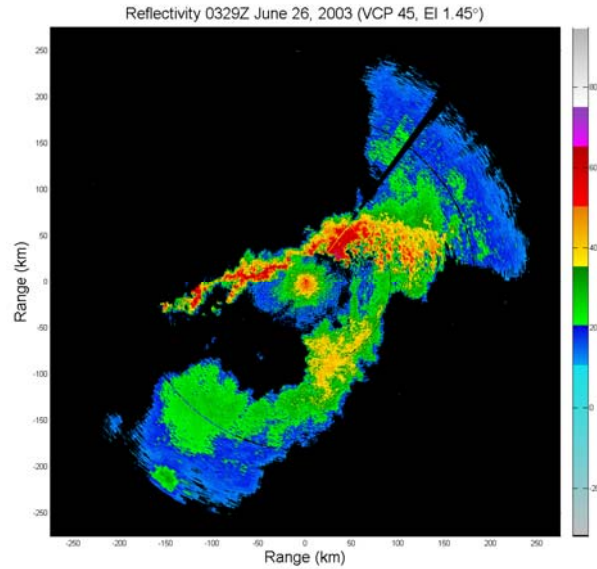


Fig. 3.16. Reflectivity field of SPRT using 2/3 PRT ratio as reprocessed in MATLAB from time series collected with KOUN on 0329Z June, 26 2003 ( $r_{a1}$  is 184 km and  $r_{a2}$  is 276 km).

Since KOUN has a transmit frequency of 2.705 MHz and the short PRT was set at 1230  $\mu$ s, this 2/3 SPRT time series provided a Nyquist velocity of about 45.1 m/s. Fig. 3.17 shows the Doppler velocity estimates recovered out to  $r_{a2}$ . For this velocity display, no overlaid threshold is applied. Fig. 3.17 shows that velocity recovery is possible in segment III using equations (3.3) and (3.4). The observed noisy velocities are caused from severe clutter contamination in segment I and need to be censored from the display. Fig. 3.18 shows the same velocity data with an overlaid threshold of 0 dB applied. Note that there are a few "catastrophic errors" in segment III in the outer edge of the display to the northeast and to the southwest. In Fig. 3.19, the "catastrophic errors" are dealiased.

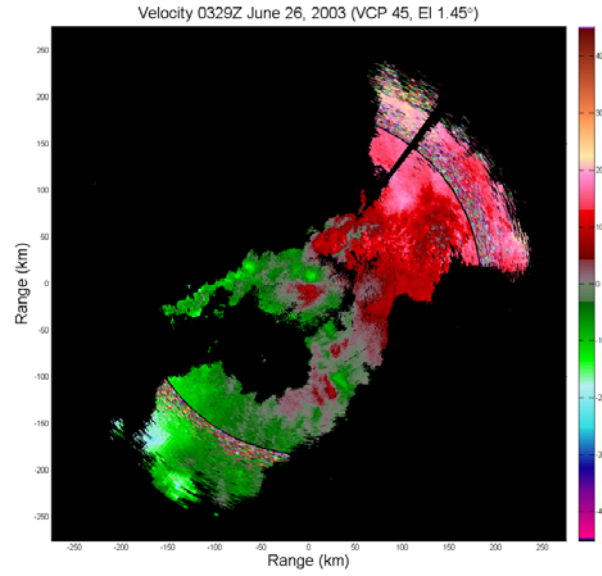


Fig. 3.17. Velocity field of SPRT using 2/3 PRT ratio as reprocessed in MATLAB without overlaid threshold applied from the same time series as in Fig. 3.16.

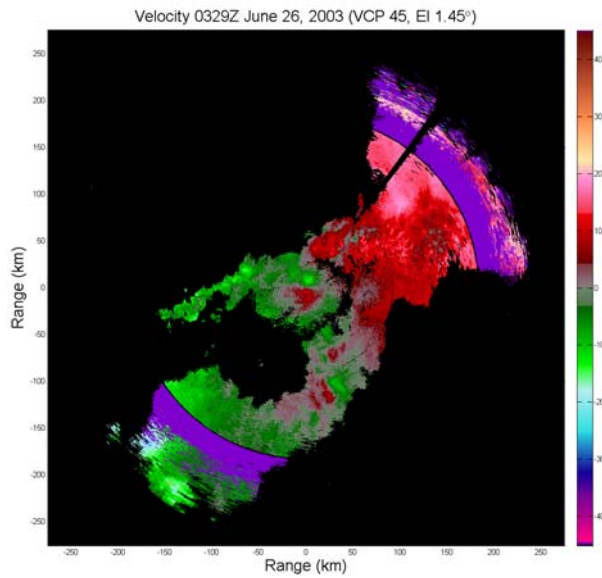


Fig. 3.18. Velocity field of SPRT using 2/3 PRT ratio as reprocessed in MATLAB with overlaid threshold set at 0 dB from the same time series as in Fig. 3.16. No velocity dealiasing was applied.

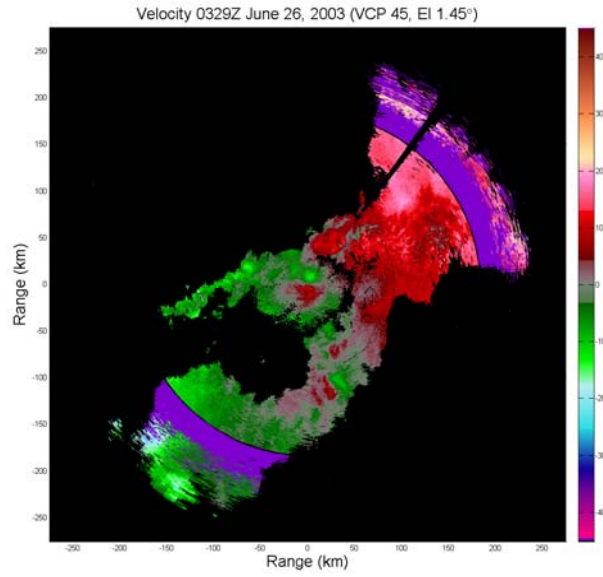


Fig. 3.19. Velocity field of SPRT using 2/3 PRT ratio as reprocessed in MATLAB with overlaid threshold set at 0 dB from the same time series as in Fig. 3.16. Velocity dealiasing was applied to remove "catastrophic errors."

Figures 3.20 and 3.21 display the SPRT recovery of the spectrum width field to  $r_{a2}$ . For Fig. 3.21, an overlaid threshold of 10 dB is applied.

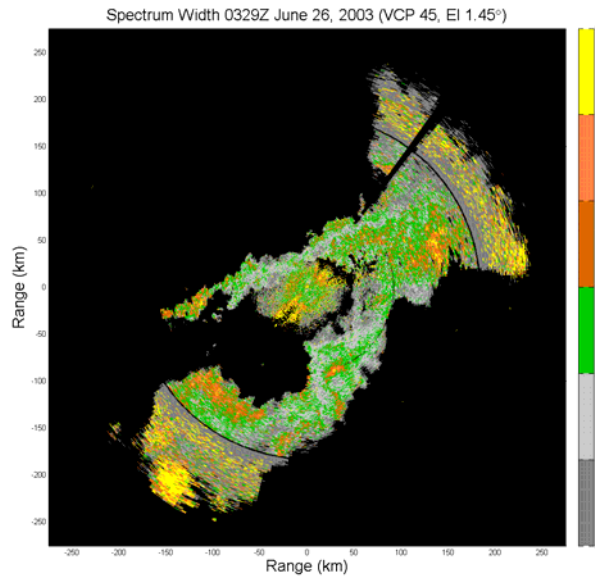


Fig. 3.19. Spectrum width field of SPRT using 2/3 PRT ratio as reprocessed in MATLAB without overlaid threshold applied from the same time series as in Fig. 3.16.

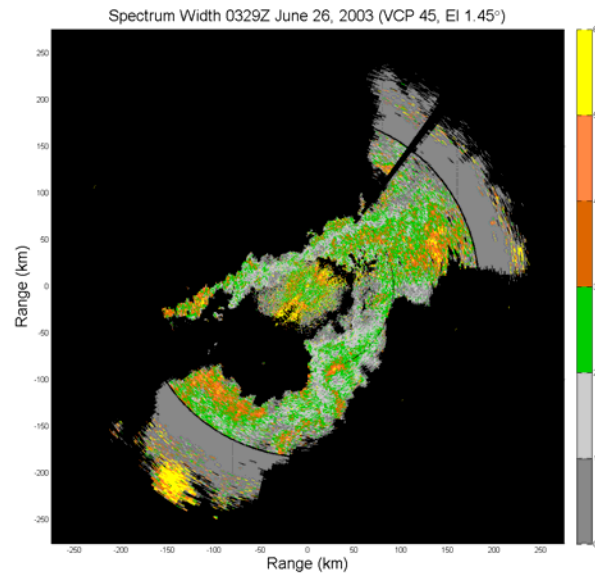


Fig. 3.19. Spectrum width field of SPRT using 2/3 PRT ratio as reprocessed in MATLAB with overlaid threshold set at 0 dB from the same time as in Fig. 3.16.



## 4. Updates to the Staggered PRT Algorithm

This section describes updates to the Staggered PRT algorithm recommended during FY 09. Updates to the May 2008 algorithm (NSSL report 12) were necessary in order to include the SACHI ground clutter filter and also to increase the range coverage of the Doppler moments to the unambiguous range of the long PRT (described in the previous section). The addition of the SACHI ground clutter filter resulted in a few constraints compared to the May 2008 algorithm. Namely, the PRT ratio must be  $2/3$ ,  $T_1$  must be the short PRT, and the number of samples must be even. Nevertheless, the ability to use shorter PRTs to meet ground clutter filtering requirements makes the SPRT algorithm now viable for operational implementation. For reference purposes, Appendix A includes a copy of the updated algorithm description that was delivered to the ROC in July of 2009.

### 4.1. Incorporating the SACHI Ground Clutter Filter

In the May 2008 algorithm, ground clutter mitigation was done using a DC-removal filter. This filter takes a dwell of time-series data and produces a filtered dwell of time-series data. Evidently, substituting this filter with the SACHI filter is not a trivial task since the outputs of the SACHI filter are the filtered weather signal moments (i.e., signal power, Doppler velocity, and spectrum width). Additionally, strong-point cancelling must occur on the filtered data stream *before* moment computations. Hence, in order to fit within the required signal processing pipeline, the output of the SACHI filter had to be modified to produce “manufactured” lag- $T_1$  and lag- $T_2$  autocorrelations (see Fig. 4.1). That is, the magnitudes of the lag- $T_1$  and lag- $T_2$  autocorrelations must be adjusted to

preserve the filtered spectrum width estimate; while, the phase of the lag  $T_1$  and lag  $T_2$  autocorrelations must be aliased to preserve the filtered velocity estimate. In other words, after the conversion and in the absence of strong-point clutter, the algorithm produces the same spectral moments as the outputs of SACHI.

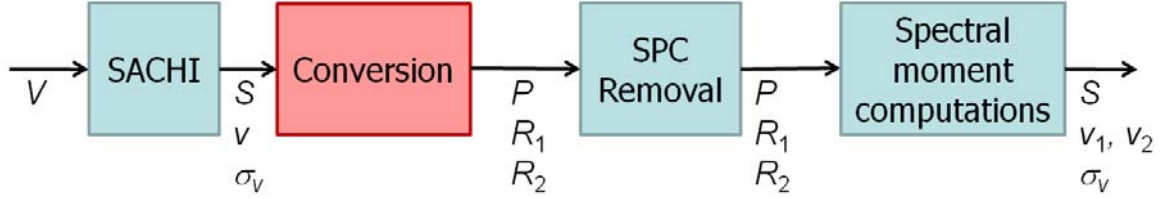


Fig. 4.1. Conversion of SACHI outputs to fit within the existing SPRT algorithm processing pipeline.

In the SPRT algorithm, signal power is estimated using

$$S = P(n) - Noise, \quad (6.1)$$

and the corresponding output from SACHI is denoted by  $S_c$ . Hence, the conversion is simply

$$P(n) = S_c + Noise, \quad (6.2)$$

so when plugging (6.2) into (6.1) we get  $S = S_c$ , as required.

Doppler velocity in the SPRT algorithm is computed from two velocity estimates corresponding to the short and long PRTs, respectively:

$$\begin{aligned} v_1 &= -\frac{\lambda}{4\pi T_1} \arg[R_1(n)], \\ v_2 &= -\frac{\lambda}{4\pi T_2} \arg[R_2(n)]. \end{aligned} \quad (6.3)$$

In the SACHI filter, the velocity estimate is already computed on the extended Nyquist interval using the following formula:

$$v = -\frac{\lambda}{4\pi T_u} \arg[R_{1c}], \quad (6.4)$$

where  $T_1 = 2T_u$  and  $T_2 = 3T_u$ . Hence, the arguments of  $R_1$  and  $R_2$  should be computed as

$$\begin{aligned} \arg[R_1(n)] &= 2 \arg[R_{1c}], \text{ and} \\ \arg[R_2(n)] &= 3 \arg[R_{1c}], \end{aligned} \quad (6.5)$$

so that when plugging (6.5) into (6.3),  $v_1$  and  $v_2$  result in aliased versions of  $v$  on the corresponding Nyquist co-intervals given by  $v_{a1}$  and  $v_{a2}$ , respectively.

The SPRT algorithm spectrum width computation is carried out as follows:

$$w(n) = \frac{\lambda}{2\sqrt{2}\pi T_1} \sqrt{\ln\left(\frac{S}{|R_1(n)|}\right)}. \quad (6.6)$$

In SACHI, the computation is similar but using different powers and correlation estimates. That is,

$$w_m = \frac{\lambda}{2\sqrt{2}\pi T_u} \sqrt{\ln\left(\frac{S_m}{|R_{1m}|}\right)}. \quad (6.7)$$

Therefore, the conversion for the magnitudes of  $R_1$  and  $R_2$  are given by:

$$\begin{aligned} |R_1(n)| &= S P_{adj}^4, \text{ and} \\ |R_2(n)| &= S P_{adj}^9, \end{aligned} \quad (6.8)$$

where

$$P_{adj} = \frac{|R_{1m}|}{P_m - N_m \text{ Noise}} = \frac{|R_{1m}|}{S_m}. \quad (6.9)$$

It is not difficult to see that inserting (6.8) into (6.6) results in (6.7). Although only one of the correlations is used in the computation of the SPRT spectrum width, both correlations are converted, so that continuity along range is preserved for the strong-point clutter filter. Note that this conversion would ensure consistent spectrum widths if (6.6) were to employ  $R_2$  instead of  $R_1$ .

With the output conversion for SACHI described above, the logic of the algorithm was modified so that the combined power and correlation computations only run when the SACHI filter is not needed. This logic is repeated in Fig. 4.3 for convenience. For gates within segments I and II (see Fig. 4.2) with clutter contamination, SACHI runs and produces “manufactured” filtered power and autocorrelation estimates at lags  $T_1$  and  $T_2$ . For gates in segment III with clutter contamination, a DC-removal filter runs and produces a dwell of filtered time-series data from which power and autocorrelations are estimated (note that in these range gates only long-PRT data is available.) If no clutter filtering is needed, power and correlations are estimated from the original dwell of time-series data.

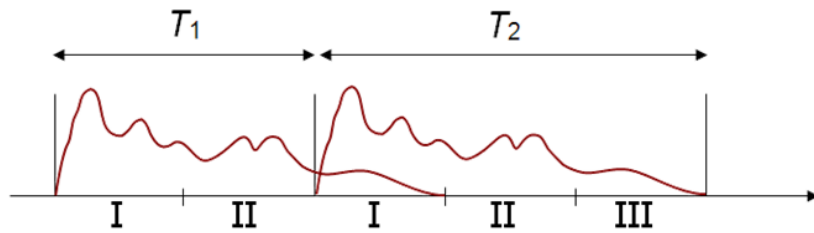


Fig. 4.2. Depiction of SPRT segments for the 2/3 PRT ratio.

```

If  $B(n) = 0$  AND  $n < N_1$ 
    6) SACHI Clutter Filtering (Segment-I/II gate with segment-I/II clutter)
Else
    If  $n \geq N_1$  AND  $B(n - N_1) = 0$ 
        7) DC Removal Clutter Filtering (Segment-III gate with segment-I clutter)
    Else
        8) No Clutter Filtering
    End
    9) Power and correlation computations for each PRT
    10) Combined power computation
End

```

Fig. 4.3. New clutter filtering logic to incorporate SACHI in the SPRT algorithm.

In addition to these changes, the SACHI filter was updated to include noise compensation vectors to properly account for the reduced number of spectral components used in the filtered power estimates. Also, readers familiar with older descriptions of the SACHI algorithm will notice that the notation in the new document has been updated to blend with the new description and to follow usual conventions. Despite these changes, the functionality of the filter as described in NSSL report 11 remains unchanged.

## 4.2. Incorporating Recovery of Range-Overlaid Echoes

As described in section 3, the performance of the SPRT algorithm is significantly better when using shorter PRTs. However, decreasing the PRTs leads to reduced range coverage. This problem is more serious in the case of Doppler moments, which, using the current algorithm, can only be retrieved up to the short-PRT unambiguous range. To extend the recovery of Doppler moments to the unambiguous range of the long PRT, the SPRT algorithm was modified to handle overlaid echoes. These modifications are described next.

### 4.2.1. *Segment-III Data Reconstruction*

In the May 2008 SPRT algorithm description, autocorrelations are computed only for those range gates within segments I and II (i.e., within the maximum unambiguous range corresponding to the short PRT,  $r_{a1}$ ). Extending this procedure to gates in segment III is not possible since only long-PRT gates are involved in the computation of lag- $T_1$  and lag- $T_2$  autocorrelations [see equations (3.3) and (3.4)]. A “trick” can be exploited to use the same functionality developed in previous descriptions to compute the desired autocorrelations for all range gates up to  $r_{a2}$ . That is, long-PRT segment-I data can be copied as the short-PRT segment-III data as depicted in Fig. 4.4. Note that if there are no overlaid echoes (i.e., for a given gate either  $S_1 = 0$  or  $S_3 = 0$ ), the autocorrelations computed in this way are exactly as needed. Otherwise, in the presence of overlaid echoes, a decision will need to be made as to the validity of these estimates both for segments I and III.

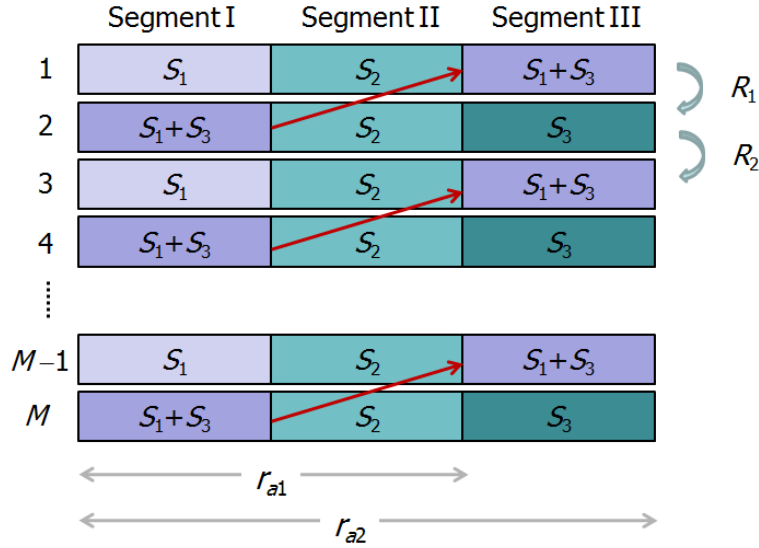


Fig. 4.4. Depiction of segment-III data reconstruction for the computation of  $R_1$  and  $R_2$  in the SPRT algorithm.

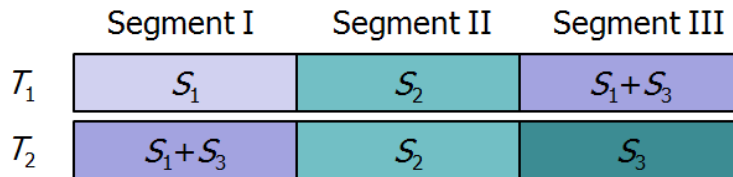


Fig. 4.5. Depiction of possible overlaid echo occurrences in the SPRT algorithm.

As illustrated in Fig. 4.5, only gates in segments I and III may contain overlaid echoes. Even then, overlaid signals appear on every other pulse so correlations are not biased (see discussion in section 3). This would suggest that recovery of correlations for all segments is possible. However, overlaid signals on every other pulse act as noise and they increase the standard deviation of correlation estimates. Therefore, to preserve the quality of base data it is mandatory to detect the presence of overlaid echoes and apply proper censoring, if needed. As mentioned before, power (or reflectivity) estimates are not affected by overlaid echoes because there is always a “clean” segment in one of the PRT sets.

Moment-specific overlaid-power-ratio thresholds are used to identify recoverable data and flag unrecoverable Doppler moments. That is, the ratio of powers from segment-I and segment-III gates that would be overlaid on every other pulse is compared against the moment-specific thresholds to flag velocities and/or spectrum widths as overlaid (purple haze).

The rules for clutter filtering have also been updated to deal with overlaid clutter signals. As shown in Fig. 4.6, gates in segments I or III that have clutter contamination will lead to overlaid clutter signals. Having multiple cases of overlaid clutter signals requires a complicated logic. However, the likelihood of having ground clutter contamination on segment-III gates at the elevation angles where staggered PRT will be used is almost zero! The worst-case scenario occurs at the lowest elevation angle (1.8 deg) and for the shortest PRT (0.88 ms). Fig. 4.7 shows the height of the antenna beam as a function of the slant range for an antenna elevation angle of 1.8 deg. Segments I, II, and III are highlighted assuming a PRT  $T_1$  of 0.88 ms. From this plot, we can see that for all segment-III gates, the antenna beam is at least 5 km from the ground, so illumination of targets on the ground is very unlikely. Moreover, this is not a realistic worst-case scenario since the PRTs recommended for the lower elevations are much longer. Fig. 4.8 shows the same situation as Fig. 4.7 but segments are delineated using a PRT  $T_1$  of 1.74 ms, a value that is recommended for VCP 212 at 1.8 deg. In this case, the antenna mainlobe is at least 12 km above the ground for any segment-III gate. Clearly, it is safe to assume that ground clutter contamination will not extend onto segment-III gates even under anomalous propagation conditions. Hence, in this version of the algorithm, ground clutter is assumed to be within the unambiguous range of the short PRT.

	Segment I	Segment II	Segment III
$T_1$	$S_1+C_1$	$S_2+C_2$	$S_1+C_1+S_3+C_3$
$T_2$	$S_1+C_1+S_3+C_3$	$S_2+C_2$	$S_3+C_3$

Fig. 4.6. Depiction of possible overlaid ground clutter occurrences in the SPRT algorithm.

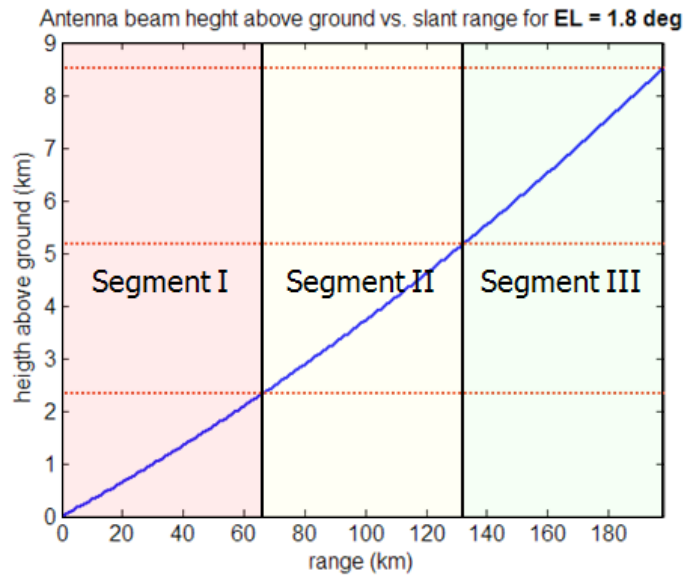


Fig. 4.7. Height above ground of the antenna beam in km as a function of the slant range in km for an antenna elevation angle of 1.8 deg. Staggered PRT segments I, II, and III are indicated for a short PRT  $T_1$  of 0.88 ms.

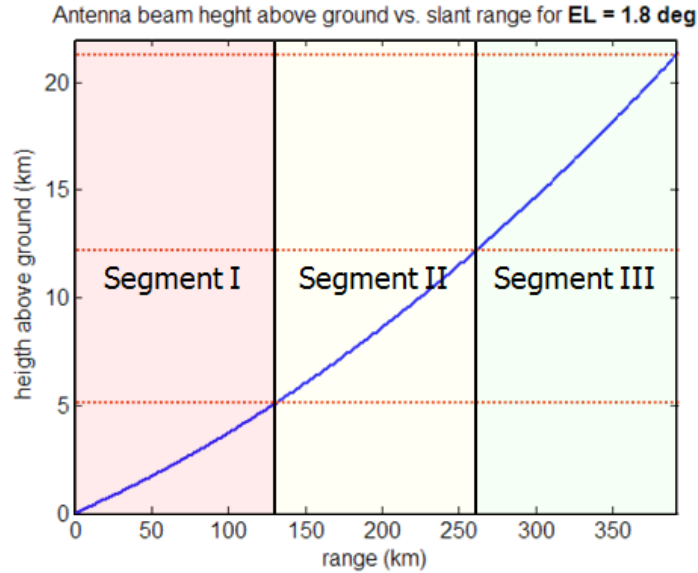


Fig. 4.8. Same as Fig. 4.7 but for a PRT  $T_1$  of 1.74 ms.

With this assumption, the rules for clutter filtering are quite simple. The SACHI filter is applied on segment-I and segment-II gates with clutter contamination. Segment-III gates are clutter-free; however, a DC-removal filter is applied to remove overlaid clutter from segment I, if needed. Note that this DC removal filter operates only on the short-PRT pulse data (see Fig. 4.6).

Because the SACHI filter was not designed to handle overlaid echoes, an overlaid power correction has been added to the algorithm. In a case of segment-III overlaid echoes, the ideal signal power output from the SACHI filter would be  $S_1 + S_3/2$ . Hence, the spurious  $S_3/2$  term must be removed. This is achieved by computing the segment-III signal power using the long-PRT pulse data. The drawback is that the algorithm now requires information about another range gate and this may prove problematic on systems that rely on data partitioning for increased throughput.

#### 4.2.2. *Summary of changes*

Even with the recommended changes to incorporate SACHI and to handle overlaid echoes, the staggered PRT algorithm remains very close to the one recommended last year. An effort was made to reuse much of the functionality implemented in previous descriptions of the algorithm. At the same time, we have taken into account the architectural limitations of the signal processing software on the ORDA.

With these changes, we are confident that staggered PRT will result in significant improvements in echo recovery and velocity dealiasing at the intermediate angles of VCPs that currently employ the Batch Mode.



## **5. Volume Coverage Patterns for Staggered PRT**

In this section, we revisit the very important topic of creating effective volume coverage patterns (VCP) to fully exploit the benefits that the staggered PRT (SPRT) algorithm can provide. We review the basic performance indicators and then establish new design criteria based on the performance of the latest SPRT algorithm. We provide examples of VCPs and recommendations for future work.

### **5.1. Designing VCPs for Staggered PRT**

We maintain that one of the most critical aspects in this project is to provide our users good VCPs that exploit the complementary behaviors of SZ-2 and SPRT. This will determine the success of our “complete solution” for range and velocity ambiguity mitigation. More so than with other improvements, it is crucial that we design VCPs for SPRT that provide the expected benefits while keeping in mind a variety of operational trade-offs. This is the main reason as to why we have devoted a considerable amount of time to this problem, although this is not the first time we attempt to tackle it.

Because the performance of the SPRT algorithm is intimately tied to the radar acquisition parameters (i.e., PRTs and dwell times), the design of VCPs for staggered PRT must follow the algorithm evolution. That is, we must comply with new limitations imposed by it such as fixing the PRT ratio to  $2/3$  as well as exploit better functionality such as the ability to recover overlaid echoes as discussed in the previous chapter. At the same time, we should be aware of operational requirements for data quality which, for example, dictate the required level of clutter suppression. Staggered PRT seems to be caught in the

middle of more trade-offs than any other evolutionary technique up to date. One reason for this maybe that with any new development, users want to retain the past performance and get more! However, we must remind our end users that every benefit usually comes at a price, and the problem consists always in choosing the lesser of the multiple evils.

In order to assess the trade-offs involved in the design of VCPs, we rely on six quantitative performance indicators: acquisition time (or dwell time), maximum unambiguous range, maximum unambiguous velocity, spectrum width saturation, errors of estimates (both statistical and dealiasing errors), and clutter suppression. These were defined in NSSL report 11 (2007). In NSSL report 12 (2008), we indicated that the benefits of using shorter PRTs overwhelm those of using longer PRTs. Namely, shorter PRTs lead to: larger Nyquist velocities, larger maximum spectrum widths, more samples for the same dwell times, lower errors of estimates, lower rates of catastrophic rates, and better clutter suppression. On the other hand, longer PRTs are needed to achieve the required coverage in range. However, with the new functionality of the SPRT algorithm to recover overlaid echoes, we are able to relax the design criteria and allow for shorter PRTs, which will improve the overall performance of the algorithm and make it more in line with current operational needs and requirements.

## **5.2. Choosing the PRTs**

The new SPRT algorithm imposes a PRT ratio of 2/3. This is needed in order to use the SACHI filter, which, unlike the DC-removal filter, achieves the required levels of clutter suppression. With the condition  $T_2 = 3T_1/2$ ,  $T_1$  should be chosen as short as possible; i.e., to produce the maximum number of gates with possible overlaid echoes that the SPRT

algorithm can handle. With the latest improvements, the SPRT algorithm can recover all moments up to  $r_{a2}$ . Therefore,  $r_{a2}$  should be set to match  $r_{max}$ ; i.e., the maximum range of echoes for a given elevation assuming the required maximum height of storm tops of 70 kft. This condition results in a value for  $T_1$  given by

$$T_1 = \frac{4r_{max}}{3c}, \quad (7.1)$$

where  $c$  is the speed of light. Note that as the antenna elevation angle increases, the value of  $r_{max}$  decreases, and shorter PRTs can (and should) be used.

In principle, (7.1) should be the only criterion to use for staggered PRT VCP design. However, there are constraints on the range and number of PRTs that we can use. In order to maintain a 0.5 m/s resolution for the Doppler velocity data transmitted from the RDA, the extended Nyquist velocity must not exceed 63 m/s. The worst-case scenario is obtained for the lowest transmitter frequency of 2700 MHz. Hence, the short PRT  $T_1$  cannot be shorter than 0.88 ms. Because we are limited to a pre-defined set of 8 PRTs, an efficient choice for these PRTs is a uniform distribution from the minimum to the maximum possible values. The maximum PRT is required to match  $r_{max}$  at the lowest elevation angle in which SPRT will be used; i.e., 1.8 deg. The corresponding value of  $r_{max}$  is 392 km, which results in a maximum value of  $T_1$  of 1.74 ms. Therefore, the PRTs that will use in our design are drawn from Table 5.1.

PRI #	Period ( $\mu$ s)	$r_{a,1}$ (km)	$r_{a,2}$ (km)	$v_a$ (m/s)
1	1743	261	392	30.2
2	1620	243	365	32.5
3	1497	224	336	35.1
4	1374	206	309	38.3
5	1251	188	282	42
6	1128	169	254	46.6
7	1005	151	227	52.3
8	881	132	198	59.7

Table 5.1. Set of short PRTs ( $T_1$ ) available for SPRT VCP design.

### 5.3. Choosing the Dwell Times

Once the PRTs are chosen, we must decide on the number of samples that will be collected for every radial. The only restriction imposed by the SPRT algorithm is that the number of samples is even (i.e., a whole number of pairs). However, the number of samples ( $M$ ) and the PRTs ( $T_1$  and  $T_2$ ) will determine the dwell time,  $DT = (T_1 + T_2)M/2$ . Dwell times must be chosen long enough so that error requirements for base-data estimates are met and the desired clutter filtering performance is achieved. However, operational needs for VCP times limit the maximum dwell times that can be used with Staggered PRT.

As was documented in NSSL report 11 (2009), excessively long dwell times seem to be needed to meet “high suppression” clutter filtering velocity requirements. Whereas this is feasible, it will certainly not be operationally acceptable. Thus, we recommend using dwell times long enough to just meet System Specification error requirements and “medium suppression” clutter filtering requirements. We believe that “medium suppression” (i.e., about 30 dB of clutter suppression) should be acceptable because at the

antenna elevation angles in which SPRT will run, returns from the ground will come mostly through the antenna sidelobes, which already provide about 30 dB of attenuation. On top of this, the current DC-removal filter employed at the intermediate elevation angles (Batch mode) in the presence of overlaid echoes exhibits a modest suppression of about 10 dB, and this is used routinely on the NEXRAD network without noticeable functional degradation.

#### **5.4. Examples of VCP Design for Staggered PRT**

Operational VCPs that employ advanced range and velocity ambiguity mitigation schemes include VCP 121 (SZ-2 and MPDA), VCP 211 (like VCP 11 but with SZ-2 on split cuts), VCP 212 (like VCP 12 but with SZ-2 on split cuts), and VCP 221 (like VCP 21 but with SZ-2 on split cuts). Of these VCPs, VCP 121 is the only scanning strategy that includes advanced algorithms for range and velocity ambiguity mitigation on every tilt. In this section, we will develop replacements for VCPs 211, 212, and 221 that use staggered PRT (SPRT) on the Batch (B) and Contiguous Doppler (CDX) tilts (i.e., for intermediate and upper elevation angles).

##### *5.4.1. VCP 211*

Table 5.2 shows the parameters and performance indicators for the current implementation of VCP 211 using the default PRT settings. The proposed staggered PRT VCP 211 (herein referred to as VCP 211S) is shown in Table 5.3, where the upper 12 tilts have been replaced with a staggered PRT waveform. Performance indicators for VCP 211S are also included in Table 5.3. Unlike with VCP 211, the maximum unambiguous ranges for surveillance and Doppler on VCP 211S are matched to the maximum possible

range of echoes ( $r_{max}$ ) to ensure full coverage. At the same time, the maximum unambiguous velocity ( $v_a$ ) is about twice as large! However, note that requirements for staggered PRT errors of velocity estimates and clutter suppression (note the ‘M’ for medium suppression) impose longer dwell times and add about 1.3 min to the total VCP time. If this additional time were not acceptable, there are some trade-offs that can be made. For example, to shorten the VCP time, the upper elevation tilts can remain unchanged (CDX waveform), or increased errors of estimates can be allowed, or clutter suppression can be reduced on the upper tilts. The final solution will depend on what the users want and what they are willing to sacrifice.

#### 5.4.2. VCP 212

Table 5.4 shows the parameters and performance indicators for the current implementation of VCP 212 using the default PRT settings. The proposed staggered PRT VCP 212 (herein referred to as VCP 212S) is shown in Table 5.5, where the upper 11 tilts have been replaced with a staggered PRT waveform. Performance indicators for VCP 212S are also included in Table 5.5. As with VCP 211S, the maximum unambiguous ranges for surveillance and Doppler on VCP 212S are matched to the maximum possible range of echoes ( $r_{max}$ ) to ensure full coverage. Here as well, the maximum unambiguous velocity ( $v_a$ ) is about twice as large. In this case, requirements for staggered PRT errors of velocity estimates and clutter suppression impose much longer dwell times and add about 2.1 min to the total VCP time, which would be clearly unacceptable. However, note that VCP 212 does not meet error requirements on the B and CDX tilts, so a similar relaxation can be allowed for VCP 212S to reduce dwell times and maintain VCP times to acceptable levels.

### 5.4.3. VCP 221

Table 5.5 shows the parameters and performance indicators for the current implementation of VCP 221 using the default PRT settings. The proposed staggered PRT VCP 221 (herein referred to as VCP 221S) is shown in Table 5.6, where the upper 7 tilts have been replaced with a staggered PRT waveform. Performance indicators for VCP 221S are also included in Table 5.6. Once again, the maximum unambiguous ranges for surveillance and Doppler on VCP 221S are matched to the maximum possible range of echoes ( $r_{max}$ ) to ensure full coverage, and the maximum unambiguous velocity ( $v_a$ ) is about twice as large. Because of the inherently longer dwell times of VCP 221, the staggered PRT dwell times needed to meet errors of estimates and clutter suppression requirements could be shorter. However, we decided to match the performance of VCP 221 in terms of data quality and therefore kept the same total VCP times as in the original VCP definition. Note that the update time of VCP 221S is suitable for operations.

Angle (deg)	AZ Rate (deg/s)	Period (s)	WF Type	Surveillance		Doppler		$T_1$ (ms)	$T_2$ (ms)	$DT$ (ms)	$r_{a,S}$ (km)	$r_{a,D}$ (km)	$v_a$ (m/s)	$\sigma_{vmax}$ (m/s)	SD(Z) (dB)*	SD(v) (m/s)	$r_{max}$ (km)
				PRF #	No. of Pulses	PRF #	No. of Pulses										
0.50	18.93	19.01	SZCS	1	17			3.11		52.81	466				0.58		533
0.50	20.03	17.97	SZCD			8	64		0.78	49.92		117	33.7	21.9		0.97	533
1.45	20.12	17.89	SZCS	1	16			3.11		49.71	466				0.60		425
1.45	20.03	17.97	SZCD			8	64		0.78	49.92		117	33.7	21.9		0.97	425
2.40	16.92	21.27	B	1	6	5	41	3.11	0.99	59.09	466	148	26.7	16.3	0.94	1.06	344
3.35	18.55	19.40	B	2	6	5	41	2.24	0.99	53.89	336	148	26.7	16.3	1.07	1.06	284
4.35	18.55	19.40	B	2	6	5	41	2.24	0.99	53.89	336	148	26.7	16.3	1.07	1.06	238
5.25	17.86	20.16	B	3	10	5	41	1.55	0.99	55.99	233	148	26.7	16.3	0.99	1.06	206
6.20	17.86	20.16	B	3	10	5	41	1.55	0.99	55.99	233	148	26.7	16.3	0.99	1.06	180
7.50	25.46	14.14	CDX			6	43		0.91	39.27	137	137	28.8	17.8	0.64	1.08	153
8.70	25.68	14.02	CDX			7	46		0.85	38.95	127	127	31.1	19.3	0.64	1.09	134
10.00	25.68	14.02	CDX			7	46		0.85	38.95	127	127	31.1	19.3	0.64	1.09	118
12.00	25.68	14.02	CDX			7	46		0.85	38.95	127	127	31.1	19.3	0.64	1.09	100
14.00	25.68	14.02	CDX			7	46		0.85	38.95	127	127	31.1	19.3	0.64	1.09	86
16.70	25.68	14.02	CDX			7	46		0.85	38.95	127	127	31.1	19.3	0.64	1.09	73
19.50	25.68	14.02	CDX			7	46		0.85	38.95	127	127	31.1	19.3	0.64	1.09	63
<b>VCP Time 4.53 min</b>																	

Table 5.2. Standard VCP 211.

Angle (deg)	AZ Rate (deg/s)	Period (s)	WF Type	Surveillance		Doppler		$T_1$ (ms)	$T_2$ (ms)	$DT$ (ms)	$r_{a,S}$ (km)	$r_{a,D}$ (km)	$v_a$ (m/s)	$\sigma_{vmax}$ (m/s)	SD(Z) (dB)*	SD(v) (m/s)	Clutter Supp.
				PRF #	No. of Pulses	PRF #	No. of Pulses										
0.50	18.93	19.01	SZCS	1	17			3.11		52.81	466				0.58		
0.50	20.03	17.97	SZCD			8	64		0.78	49.92		117	33.7	21.9		0.97	
1.45	20.12	17.89	SZCS	1	16			3.11		49.71	466				0.60		
1.45	20.03	17.97	SZCD			8	64		0.78	49.92		117	33.7	21.9		0.97	
2.40	14.84	24.25	SPRT			3	36	1.50	2.25	67.37	337	337	35.1	10.6	0.53	0.93	M
3.35	17.76	20.27	SPRT			5	36	1.25	1.88	56.30	281	281	42.0	12.7	0.57	1.03	M
4.35	16.58	21.71	SPRT			7	48	1.01	1.51	60.30	226	226	52.3	16.4	0.54	1.02	M
5.25	15.13	23.79	SPRT			8	60	0.88	1.32	66.08	198	198	59.7	19.2	0.51	1.00	M
6.20	15.13	23.79	SPRT			8	60	0.88	1.32	66.08	198	198	59.7	19.2	0.51	1.00	M
7.50	15.13	23.79	SPRT			8	60	0.88	1.32	66.08	198	198	59.7	19.2	0.51	1.00	M
8.70	15.13	23.79	SPRT			8	60	0.88	1.32	66.08	198	198	59.7	19.2	0.51	1.00	M
10.00	15.13	23.79	SPRT			8	60	0.88	1.32	66.08	198	198	59.7	19.2	0.51	1.00	M
12.00	15.13	23.79	SPRT			8	60	0.88	1.32	66.08	198	198	59.7	19.2	0.51	1.00	M
14.00	15.13	23.79	SPRT			8	60	0.88	1.32	66.08	198	198	59.7	19.2	0.51	1.00	M
16.70	15.13	23.79	SPRT			8	60	0.88	1.32	66.08	198	198	59.7	19.2	0.51	1.00	M
19.50	15.13	23.79	SPRT			8	60	0.88	1.32	66.08	198	198	59.7	19.2	0.51	1.00	M
<b>VCP Time 5.89 min</b>																	

Table 5.3. Staggered PRT VCP 211, VCP 211S.

Angle (deg)	AZ Rate (deg/s)	Period (s)	WF Type	Surveillance		Doppler		$T_1$ (ms)	$T_2$ (ms)	$DT$ (ms)	$r_{a,S}$ (km)	$r_{a,D}$ (km)	$v_a$ (m/s)	$\sigma_{vmax}$ (m/s)	SD(Z) (dB)*	SD(v) (m/s)	$r_{max}$ (km)	
				PRF #	No. of Pulses	PRF #	No. of Pulses											
0.50	21.46	16.78	SZCS	1	15			3.11		46.60	466				0.62		533	
0.50	17.11	21.04	SZCD			6	64		0.91	58.45		137	28.8	18.7		0.89	533	
0.90	21.46	16.78	SZCS	1	15			3.11		46.60	466				0.62		484	
0.90	17.11	21.04	SZCD			6	64		0.91	58.45		137	28.8	18.7		0.89	484	
1.30	21.46	16.78	SZCS	1	15			3.11		46.60	466				0.62		440	
1.30	17.11	21.04	SZCD			6	64		0.91	58.45		137	28.8	18.7		0.89	440	
1.80	26.36	13.66	B	1	3	5	29	3.11	0.99	37.93	466	148	26.7	15.6	1.28	1.26	392	
2.40	27.53	13.08	B	2	3	5	30	2.24	0.99	36.32	336	148	26.7	15.6	1.44	1.24	344	
3.10	27.53	13.08	B	2	3	5	30	2.24	0.99	36.32	336	148	26.7	15.6	1.44	1.24	298	
4.00	27.53	13.08	B	2	3	5	30	2.24	0.99	36.32	336	148	26.7	15.6	1.44	1.24	252	
5.10	29.19	12.33	B	3	3	5	30	1.55	0.99	34.26	233	148	26.7	15.6	1.66	1.24	211	
6.40	29.19	12.33	B	3	3	5	30	1.55	0.99	34.26	233	148	26.7	15.6	1.66	1.24	175	
8.00	28.81	12.49	CDX			6	38		0.91	34.71	137	137	28.8	17.5	0.67	1.15	145	
10.00	29.53	12.19	CDX			7	40		0.85	33.87	127	127	31.1	19.0	0.68	1.17	118	
12.50	29.14	12.36	CDX			8	44		0.78	34.32	117	117	33.7	20.9	0.67	1.17	96	
15.60	29.14	12.36	CDX			8	44		0.78	34.32	117	117	33.7	20.9	0.67	1.17	78	
19.50	29.14	12.36	CDX			8	44		0.78	34.32	117	117	33.7	20.9	0.67	1.17	63	
<b>VCP Time 4.21 min</b>																		

Table 5.4. Standard VCP 212.

Angle (deg)	AZ Rate (deg/s)	Period (s)	WF Type	Surveillance		Doppler		$T_1$ (ms)	$T_2$ (ms)	$DT$ (ms)	$r_{a,S}$ (km)	$r_{a,D}$ (km)	$v_a$ (m/s)	$\sigma_{vmax}$ (m/s)	SD(Z) (dB)*	SD(v) (m/s)	Clutter Supp.	
				PRF #	No. of Pulses	PRF #	No. of Pulses											
0.50	21.46	16.78	SZCS	1	15			3.11		46.60	466				0.62			
0.50	17.11	21.04	SZCD			6	64		0.91	58.45		137	28.8	18.7		0.89		
0.90	21.46	16.78	SZCS	1	15			3.11		46.60	466				0.62			
0.90	17.11	21.04	SZCD			6	64		0.91	58.45		137	28.8	18.7		0.89		
1.30	21.46	16.78	SZCS	1	15			3.11		46.60	466				0.62			
1.30	17.11	21.04	SZCD			6	64		0.91	58.45		137	28.8	18.7		0.89		
1.80	11.47	31.37	SPRT			1	40	1.74	2.61	87.15	392	392	30.2	9.2	0.47	0.83	M	
2.40	14.84	24.25	SPRT			3	36	1.50	2.25	67.37	337	337	35.1	10.6	0.53	0.93	M	
3.10	16.17	22.26	SPRT			4	36	1.37	2.06	61.83	309	309	38.3	11.5	0.55	0.98	M	
4.00	16.12	22.33	SPRT			6	44	1.13	1.69	62.04	254	254	46.6	14.4	0.54	0.99	M	
5.10	15.13	23.79	SPRT			8	60	0.88	1.32	66.08	198	198	59.7	19.2	0.51	1.00	M	
6.40	15.13	23.79	SPRT			8	60	0.88	1.32	66.08	198	198	59.7	19.2	0.51	1.00	M	
8.00	15.13	23.79	SPRT			8	60	0.88	1.32	66.08	198	198	59.7	19.2	0.51	1.00	M	
10.00	15.13	23.79	SPRT			8	60	0.88	1.32	66.08	198	198	59.7	19.2	0.51	1.00	M	
12.50	15.13	23.79	SPRT			8	60	0.88	1.32	66.08	198	198	59.7	19.2	0.51	1.00	M	
15.60	15.13	23.79	SPRT			8	60	0.88	1.32	66.08	198	198	59.7	19.2	0.51	1.00	M	
19.50	15.13	23.79	SPRT			8	60	0.88	1.32	66.08	198	198	59.7	19.2	0.51	1.00	M	
<b>VCP Time 6.34 min</b>																		

Table 5.5. Staggered PRT VCP 212, VCP 212S.

Angle (deg)	AZ Rate (deg/s)	Period (s)	WF Type	Surveillance		Doppler		$T_1$ (ms)	$T_2$ (ms)	$DT$ (ms)	$r_{a,S}$ (km)	$r_{a,D}$ (km)	$v_a$ (m/s)	$\sigma_{vmax}$ (m/s)	SD(Z) (dB)*	SD(v) (m/s)	$r_{max}$ (km)
				PRF #	No. of Pulses	PRF #	No. of Pulses										
0.50	11.50	31.32	SZCS	1	28			3.11		86.99	466				0.46		533
0.50	15.84	22.73	SZCD			5	64		0.99	63.15		148	26.7	17.3		0.85	533
1.45	11.50	31.32	SZCS	1	28			3.11		86.99	466				0.46		425
1.45	15.84	22.73	SZCD			5	64		0.99	63.15		148	26.7	17.3		0.85	425
2.40	11.53	31.23	B	2	8	4	59	2.24	1.17	86.76	336	175	22.5	14.5	0.94	0.81	344
3.35	11.53	31.23	B	2	8	4	59	2.24	1.17	86.76	336	175	22.5	14.5	0.94	0.81	284
4.30	11.53	31.23	B	2	8	4	59	2.24	1.17	86.76	336	175	22.5	14.5	0.94	0.81	240
6.00	11.43	31.49	B	3	12	4	59	1.55	1.17	87.47	233	175	22.5	14.5	0.91	0.81	185
9.90	12.30	29.26	CDX			7	96		0.85	81.28	127	127	31.1	21.1	0.45	0.76	119
14.60	12.30	29.26	CDX			7	96		0.85	81.28	127	127	31.1	21.1	0.45	0.76	83
19.50	12.30	29.26	CDX			7	96		0.85	81.28	127	127	31.1	21.1	0.45	0.76	63
<b>VCP Time</b>				<b>5.35</b>	<b>min</b>												

Table 5.6. Standard VCP 221.

Angle (deg)	AZ Rate (deg/s)	Period (s)	WF Type	Surveillance		Doppler		$T_1$ (ms)	$T_2$ (ms)	$DT$ (ms)	$r_{a,S}$ (km)	$r_{a,D}$ (km)	$v_a$ (m/s)	$\sigma_{vmax}$ (m/s)	SD(Z) (dB)*	SD(v) (m/s)	Clutter Supp.
				PRF #	No. of Pulses	PRF #	No. of Pulses										
0.50	11.50	31.32	SZCS	1	28			3.11		86.99	466				0.46		
0.50	15.84	22.73	SZCD			5	64		0.99	63.15		148	26.7	17.3		0.85	
1.45	11.50	31.32	SZCS	1	28			3.11		86.99	466				0.46		
1.45	15.84	22.73	SZCD			5	64		0.99	63.15		148	26.7	17.3		0.85	
2.40	11.62	30.99	SPRT			3	46	1.50	2.25	86.08	337	337	35.1	10.9	0.47	0.83	M
3.35	11.42	31.53	SPRT			5	56	1.25	1.88	87.57	281	281	42.0	13.4	0.46	0.83	M
4.30	11.44	31.47	SPRT			6	62	1.13	1.69	87.42	254	254	46.6	15.1	0.46	0.84	H
6.00	11.35	31.72	SPRT			8	80	0.88	1.32	88.10	198	198	59.7	19.9	0.45	0.87	H
9.90	12.27	29.34	SPRT			8	74	0.88	1.32	81.49	198	198	59.7	19.7	0.47	0.90	M
14.60	12.27	29.34	SPRT			8	74	0.88	1.32	81.49	198	198	59.7	19.7	0.47	0.90	M
19.50	12.27	29.34	SPRT			8	74	0.88	1.32	81.49	198	198	59.7	19.7	0.47	0.90	M
<b>VCP Time 5.36 min</b>																	

Table 5.7. Staggered PRT VCP 221, VCP 221S.

## **5.5. Summary of Performance and Recommendations**

The exercise in the previous section reveals that, in general, similar or longer dwell times are required when replacing Batch (B) and Contiguous Doppler (CD/CDX) modes with Staggered PRT (SPRT). This is the price to pay in order to get longer range coverage, significantly larger Nyquist velocities, improved clutter suppression, and much lower standard error of reflectivities. Even then, in those instances where SPRT dwell times are about 20% longer than B or CD dwell times, some trade-offs are available that can help bring the VCP times down to operationally acceptable levels.

An additional disadvantage of the current SPRT algorithm is the occurrence of “catastrophic” velocity dealiasing errors. However, there is preliminary evidence that these are “speckly” in nature and can be easily corrected with the ORPG modified velocity dealiasing algorithm (Torres et al. 2009).

We recommend that the proposed VCPs or some variation of them are implemented on the ROC’s testbed for engineering evaluation. It would be important to collect several data cases with the proper settings that would exploit the advantages of the staggered PRT technique to their fullest. Data cases should be processed with the latest version of the recommended SPRT algorithm (included in this report) and base data produced in such manner should be run through the ORPG’s modified velocity dealiasing algorithm. Finally, data quality should be assessed both quantitatively but also qualitatively by direct comparison of SPRT-derived data fields with their corresponding Batch and Contiguous Doppler counterparts.

Success of this program depends critically on the ability to show that the main trade-offs associated with the staggered PRT technique are a relatively cheap price to pay for the expected drastic improvement in performance.



## 6. References

Sachidananda, M., 1999: Signal Design and Processing Techniques for WSR-88D Ambiguity Resolution, NOAA/NSSL Report, Part 3, 81 pp.

Sachidananda, M., 2000: Signal Design and Processing Techniques for WSR-88D Ambiguity Resolution, NOAA/NSSL Report, Part 4, 99 pp.

Sachidananda, M., 2001: Signal Design and Processing Techniques for WSR-88D Ambiguity Resolution, NOAA/NSSL Report, Part 5, 75 pp.

Sachidananda, M., 2002: Signal Design and Processing Techniques for WSR-88D Ambiguity Resolution, NOAA/NSSL Report, Part 6, 57 pp.

Sachidananda, M., D. Zrnić, 2003: Unambiguous range extension by overlay resolution in staggered PRT technique. *J. Atmos. Oceanic Technol.*, 20, 673-684.

Sirmans, D., 1998: Note on spectrum width calculation in the WSR-88D and recommended software changes. Operational Support Facility internal report, February, 1998.

Sirmans, D., and W. Bumgarner, 1990: Velocity estimate bias due to range overlaid echoes. Operational Support Facility internal report, November, 1990.

Sirmans, D., D. Zrnić, and B. Bumgarner, 1976: Extension of maximum unambiguous Doppler velocity by use of two sampling rates. Preprints, 17th Conf. on Radar Meteorology, Seattle, WA, Amer. Meteor. Soc., 23–28.

Torres S., M. Sachidananda, and D. Zrnić, 2005: Signal Design and Processing Techniques for WSR-88D Ambiguity Resolution: Phase coding and staggered PRT. NOAA/NSSL Report, Part 9, 112 pp.

Torres S., M. Sachidananda, and D. Zrnić, 2007: Signal Design and Processing Techniques for WSR-88D Ambiguity Resolution: Staggered PRT and updates to the SZ-2 algorithm. NOAA/NSSL Report, Part 11, 146 pp.

Torres, S., and D. Warde, 2009: Staggered PRT with ground clutter filtering and overlaid echo recovery: Algorithm description. NOAA/NSSL Report, June 18, 2009.

Torres, S., and D. Zrnić, 2006: Signal Design and Processing Techniques for WSR-88D Ambiguity Resolution: Evolution of the SZ-2 Algorithm. NOAA/NSSL Report, Part 10, 71 pp.

Torres, S., and D. Zrnić, 2007: Signal Design and Processing Techniques for WSR-88D Ambiguity Resolution: Evolution of the SZ-2 Algorithm. NOAA/NSSL Report, Part 11, 145 pp.

Torres, S., and D. Zrnić, 2009: Signal Design and Processing Techniques for WSR-88D Ambiguity Resolution: Staggered PRT Updates and Generalized Phase Codes. NOAA/NSSL Report, Part 12, 156 pp.

Torres, S., D. Zittel, and D. Saxion, 2009: Update on Development of Staggered PRT for the NEXRAD Network. Preprints, 25th International Conference on Interactive Information and Processing Systems (IIPS) for Meteorology, Oceanography, and Hydrology, Phoenix, AZ, Amer. Meteor. Soc., Paper 11B.2.

Torres, S., D. Zrnić, and Y. Dubel, 2003: Signal Design and Processing Techniques for WSR-88D Ambiguity Resolution: Phase coding and staggered PRT: Implementation, data collection, and processing. NOAA/NSSL Report, Part 7, 128 pp.

Torres, S., M. Sachidananda, and D. Zrnić, 2004: Signal Design and Processing Techniques for WSR-88D Ambiguity Resolution: Phase coding and staggered PRT: Data collection, implementation, and clutter filtering. NOAA/NSSL Report, Part 8, 113 pp.

Torres, S., M., Sachidananda, and D. Zrnić, 2005: Signal Design and Processing Techniques for WSR-88D Ambiguity Resolution: Phase coding and staggered PRT. NOAA/NSSL Report, Part 9, 112 pp.

Torres, S., Y. Dubel, and D. S. Zrnić, 2004: Design, implementation, and demonstration of a staggered PRT algorithm for the WSR-88D. *J. Atmos. Oceanic Technol.*, **21**, 1389-1399.

Warde, D. A., and S. Torres, 2009: The Range-Overlaid Staggered PRT Algorithm. Preprints, *34th International Conference on Radar Meteorology*, Williamsburg, VA, USA, American Meteorological Society, CD-ROM, P5.11. Doviak, R. J. and Zrnić, D., *Doppler Radar and Weather Observations*, 2nd Edition, 1999. Academic Press, pp 134.

Zrnić, D. S., 1975: Simulation of weather like Doppler spectra and signals, *Journal of Applied Meteorology*, **14**, No. 4, 619-620.

**LIST OF NSSL REPORTS FOCUSED ON POSSIBLE UPGRADES  
TO THE WSR-88D RADARS**

Torres S., M., D. Warde, and D. Zrnić, 2009: Signal Design and Processing Techniques for WSR-88D Ambiguity Resolution: Staggered PRT Updates and Generalized Phase Codes. NOAA/NSSL Report, Part 12, 156 pp.

Torres S., M. and D. Zrnić, 2007: Signal Design and Processing Techniques for WSR-88D Ambiguity Resolution: Evolution of the SZ-2 Algorithm. NOAA/NSSL Report, Part 11, 145 pp.

Zrnić, D.S., Melnikov, V. M., J. K. Carter, and I. Ivić, 2007: Calibrating differential reflectivity on the WSR-88D, (Part 2). NOAA/NSSL Report, 34 pp.

Torres S., M. and D. Zrnić, 2006: Signal Design and Processing Techniques for WSR-88D Ambiguity Resolution: Evolution of the SZ-2 Algorithm. NOAA/NSSL Report, Part 10, 71 pp.

Torres S., M. Sachidananda, and D. Zrnić, 2005: Signal Design and Processing Techniques for WSR-88D Ambiguity Resolution: Phase coding and staggered PRT. NOAA/NSSL Report, Part 9, 112 pp.

Zrnić, D.S., Melnikov, V.M., and J.K. Carter, 2005: Calibrating differential reflectivity on the WSR-88D. NOAA/NSSL Report, 34 pp.

Torres S., M. Sachidananda, and D. Zrnić, 2004: Signal Design and Processing Techniques for WSR-88D Ambiguity Resolution: Phase coding and staggered PRT: Data collection, implementation, and clutter filtering. NOAA/NSSL Report, Part 8, 113 pp.

Zrnić, D., S. Torres, J. Hubbert, M. Dixon, G. Meymaris, and S. Ellis, 2004: NEXRAD range-velocity ambiguity mitigation. SZ-2 algorithm recommendations. NCAR-NSSL Interim Report.

Melnikov, V, and D Zrnić, 2004: Simultaneous transmission mode for the polarimetric WSR-88D – statistical biases and standard deviations of polarimetric variables. NOAA/NSSL Report, 84 pp.

Bachman, S., 2004: Analysis of Doppler spectra obtained with WSR-88D radar from non-stormy environment. NOAA/NSSL Report, 86 pp.

Zrnić, D., S. Torres, Y. Dubel, J. Keeler, J. Hubbert, M. Dixon, G. Meymaris, and S. Ellis, 2003: NEXRAD range-velocity ambiguity mitigation. SZ(8/64) phase coding algorithm recommendations. NCAR-NSSL Interim Report.

Torres S., D. Zrnić, and Y. Dubel, 2003: Signal Design and Processing Techniques for WSR-88D Ambiguity Resolution: Phase coding and staggered PRT: Implementation, data collection, and processing. NOAA/NSSL Report, Part 7, 128 pp.

Schuur, T., P. Heinselman, and K. Scharfenberg, 2003: Overview of the Joint Polarization Experiment (JPOLE), NOAA/NSSL Report, 38 pp.

Ryzhkov, A, 2003: Rainfall Measurements with the Polarimetric WSR-88D Radar, NOAA/NSSL Report, 99 pp.

Schuur, T., A. Ryzhkov, and P. Heinselman, 2003: Observations and Classification of echoes with the Polarimetric WSR-88D radar, NOAA/NSSL Report, 45 pp.

Melnikov, V., D. Zrnić, R. J. Doviak, and J. K. Carter, 2003: Calibration and Performance Analysis of NSSL's Polarimetric WSR-88D, NOAA/NSSL Report, 77 pp.

NCAR-NSSL Interim Report, 2003: NEXRAD Range-Velocity Ambiguity Mitigation SZ(8/64) Phase Coding Algorithm Recommendations.

Sachidananda, M., 2002: Signal Design and Processing Techniques for WSR-88D Ambiguity Resolution, NOAA/NSSL Report, Part 6, 57 pp.

Doviak, R., J. Carter, V. Melnikov, and D. Zrnić, 2002: Modifications to the Research WSR-88D to obtain Polarimetric Data, NOAA/NSSL Report, 49 pp.

Fang, M., and R. Doviak, 2001: Spectrum width statistics of various weather phenomena, NOAA/NSSL Report, 62 pp.

Sachidananda, M., 2001: Signal Design and Processing Techniques for WSR-88D Ambiguity Resolution, NOAA/NSSL Report, Part 5, 75 pp.

Sachidananda, M., 2000: Signal Design and Processing Techniques for WSR-88D Ambiguity Resolution, NOAA/NSSL Report, Part 4, 99 pp.

Sachidananda, M., 1999: Signal Design and Processing Techniques for WSR-88D Ambiguity Resolution, NOAA/NSSL Report, Part 3, 81 pp.

Sachidananda, M., 1998: Signal Design and Processing Techniques for WSR-88D Ambiguity Resolution, NOAA/NSSL Report, Part 2, 105 pp.

Torres, S., 1998: Ground Clutter Canceling with a Regression Filter, NOAA/NSSL Report, 37 pp.

Doviak, R. and D. Zrnić, 1998: WSR-88D Radar for Research and Enhancement of Operations: Polarimetric Upgrades to Improve Rainfall Measurements, NOAA/NSSL Report, 110 pp.

Sachidananda, M., 1997: Signal Design and Processing Techniques for WSR-88D Ambiguity Resolution, NOAA/NSSL Report, Part 1, 100 pp.

Sirmans, D., D. Znić, and M. Sachidananda, 1986: Doppler radar dual polarization considerations for NEXRAD, NOAA/NSSL Report, Part I, 109 pp.

Sirmans, D., D. Znić, and N. Balakrishnan, 1986: Doppler radar dual polarization considerations for NEXRAD, NOAA/NSSL Report, Part II, 70 pp.



## **Appendix A. Staggered PRT Algorithm Description (July 2009)**

### **A.1. Preface**

This document extends the previous Staggered PRT algorithm descriptions from May 2008 and March 2009 by including the SACHI ground clutter filter *and* increasing the range coverage of the Doppler moments to the unambiguous range of the long PRT. This algorithm description includes a high-level description with the overall processing logic followed by a detailed explanation of each pre-computation and processing step.

As in the March 2009 description, in order to fit within the required signal processing pipeline, the output of the SACHI filter has been modified to produce “manufactured” lag- $T_1$  and lag- $T_2$  autocorrelations. That is, the magnitudes of the lag- $T_1$  and lag- $T_2$  autocorrelations have been adjusted to preserve the filtered spectrum width estimate; while, the phase of the lag- $T_1$  and lag- $T_2$  autocorrelations have been aliased to preserve the filtered velocity estimate. Additionally, noise compensation vectors have been added to the algorithm to properly account for the reduced number of spectral components used in the filtered power estimates. Readers familiar with older descriptions of the SACHI algorithm will notice that the notation in this document has been updated to blend with the May 2008 SPRT algorithm description and to follow usual conventions. Further, to ease implementation and reduce ambiguity, many of the steps in the SACHI algorithm are now described in algorithmic form. Despite these changes, the functionality of the filter as described in our Report 11 remains unchanged. The DC removal ground clutter filter has been retained to operate on those range gates where only long-PRT data is available and ground clutter filtering is needed.

To extend the recovery of Doppler moments to the unambiguous range of the long PRT, the algorithm has been modified to handle overlaid echoes. Moment-specific overlaid power thresholds are used to identify recoverable data and flag unrecoverable Doppler moments. Also, the rules for clutter filtering have been updated to deal with overlaid clutter, and an overlaid power correction has been added to the SACHI filter. In this

version of the algorithm, ground clutter is assumed to be within the unambiguous range of the short PRT.

As with the March 2009 description, the addition of the SACHI ground clutter filter resulted in a few constraints compared to the May 2008 description. Specifically, the PRT ratio must be  $2/3$ ,  $T_1$  must be the short PRT, and the number of samples must be even. Nevertheless, the ability to use shorter PRTs to meet ground clutter filtering requirements makes the SPRT algorithm viable for operational implementation.

## A.2. Assumptions

- 1) The transmission sequence alternates two pulse repetition times (PRT) as:  $T_1, T_2, T_1, T_2 \dots$  for a total of  $M$  pulses.
- 2) The PRT ratio  $T_1/T_2 = 2/3$ , where  $\kappa_m = 2$ ,  $\kappa_n = 3$  and  $T_2 - T_1 = T_u$ .
- 3) All range gates are available and there is a perfect alignment of range gates between the two PRTs (i.e., a given range gate represents the same resolution volume in space for every transmitted pulse). Also, the number of range gates for each PRT is:  $N_1 = T_1/\tau_s$  and  $N_2 = T_2/\tau_s$ , where  $\tau_s$  is the sampling period.
- 4) There are no significant echoes beyond the maximum unambiguous range corresponding to  $T_2$  ( $r_{a2}$ ).
- 5) There is no significant ground clutter beyond the maximum unambiguous range corresponding to  $T_1$  ( $r_{a1}$ ).
- 6) The number of staggered PRT samples per range gate ( $M$ ) is even.
- 7) The algorithm operates on a radial worth of data at a time.

## A.3. Inputs

- 1) Complex time-series data:

$V(n, m) = I(n, m) + jQ(n, m)$ , where  $0 \leq n < N_1$  for even  $m$ ,  $0 \leq n < N_2$  for odd  $m$  and  $0 \leq m < M$ . Note that  $n$  indexes the range gates and  $m$  the sweeps (or pulses).

- 2) Associated metadata:

$\lambda$  is the radar wavelength in meters

*Noise* is the noise power in linear units

$dBZ0$  is the system calibration constant in dB

$ATMOS$  is the elevation-dependent atmospheric attenuation in dB/km

$\Delta R$  is the spacing between range gates in km ( $\Delta R = c \tau_s / 2$ )

$T_Z$  is the signal-to-noise ratio threshold for reflectivity in dB

$T_V$  is the signal-to-noise ratio threshold for velocity in dB

$T_W$  is the signal-to-noise ratio threshold for spectrum width in dB

$T_{OV}$  is the velocity overlaid threshold in dB (*Note: recommended value is 0 dB*)

$T_{OW}$  is the spectrum width overlaid threshold in dB (*Note: recommended value is 10 dB*)

3) Data window:

$d'(m)$ , where  $0 \leq m < 5M/2$ . Note that  $d'$  does not need to be normalized or scaled in any way. A tapered data window such as the Blackman window is recommended for best performance of the SACHI ground clutter filter. Otherwise, rectangular window (i.e., no window) should be applied.

4) Ground clutter filter bypass map:

$B(n)$ , where  $n$  indexes the range bins with the same resolution as the time-series data along a radial, and the map corresponds to the elevation and azimuth of the radial being processed.  $B$  is 0 if clutter filtering is required and 1 otherwise. In this algorithm, the clutter map is ignored beyond the unambiguous range corresponding to the short PRT where clutter is assumed not to be present.

#### A.4. Outputs

1) Reflectivity, Doppler velocity, and spectrum width:

$$\begin{array}{ll} Z(n) & \text{for } 0 \leq n < N_2, \\ v(n) \text{ and } w(n) & \text{for } 0 \leq n < N_2. \end{array}$$

2) Signal-to-noise ratio and overlaid censoring flags:

$$\begin{array}{ll} NS_Z(n), NS_V(n) \text{ and } NS_W(n) & \text{for } 0 \leq n < N_2, \\ OV_V(n) \text{ and } OV_W(n) & \text{for } 0 \leq n < N_2. \end{array}$$

#### A.5. Functions and Conventions

- 1)  $|\cdot|$  – Returns the absolute value of a complex number or the absolute value of each element of a matrix of complex numbers.
- 2)  $\arg$  – Returns the principal phase angle of the input complex number in radians. The algorithm is written to accommodate this phase in the interval  $[0, 2\pi)$  or  $[-\pi, \pi)$ .

- 3)  $\arg \min_k$  – Returns the index  $k$  to the element in the input vector that has the minimum value.
- 4)  $\text{diag}$  – Returns a square matrix with the input vector along the principal diagonal (row index = column index) of the matrix and all other elements not on the principal diagonal equal to zero. The number of rows (columns) of the matrix is equal to the number of elements in the vector.
- 5)  $\text{ceiling}$  – Returns the smallest integer value not less than the input number.
- 6)  $\text{floor}$  – Returns the largest integer value not greater than the input number.
- 7)  $\text{round}$  – Returns the nearest integer to the input number.
- 8) Italicized names are used to denote scalars (e.g., *Noise*).
- 9) Bolded names are used to denote vectors or matrices (e.g., **A**). Italicized names with indexing in parentheses are used to denote elements of a vector or matrix [e.g.,  $A(i,j)$ ].
- 10)  $*$  – Denotes complex conjugate.
- 11)  $T$  – Denotes matrix transpose.
- 12)  $j$  – Denotes the imaginary unit  $\sqrt{-1}$ .

## A.6. High-level Algorithm description

If first run of SPRT algorithm

- 1) Pre-computation of velocity dealiasing rules
- 2) Pre-computation of  $M$ -independent SACHI filter parameters

End

If the number of samples ( $M$ ) changed

- 3) Pre-computation of window parameters#
- 4) Pre-computation of  $M$ -dependent SACHI filter parameters

End

For each range bin  $n$ , where  $0 \leq n < N_2$

If  $n \geq N_1$

- 5) Short-PRT Segment-III Data Reconstruction

End

If  $B(n) = 0$  AND  $n < N_1$

- 6) SACHI Clutter Filtering (Segment-I/II gate with segment-I/II clutter)

Else

If  $n \geq N_1$  AND  $B(n - N_1) = 0$

- 7) DC Removal Clutter Filtering (Segment-III gate with segment-I clutter)

Else

- 8) No Clutter Filtering

End

- 9) Power and correlation computations for each PRT

- 10) Combined power computation

End

End

11) Strong point clutter canceling

For each range bin  $n$ , where  $0 \leq n < N_2$

12) Signal power computation

13) Reflectivity computation

14) Velocity computation

15) Spectrum width computation

# 16) Determination of significant returns for reflectivity

17) Determination of significant returns for velocity

18) Determination of significant returns for spectrum width

End

For each range bin  $n$ , where  $0 \leq n < N_2$

19) Determination of overlaid returns for velocity and spectrum width

End

## A.7. Step-by-step algorithm description

### 1. Pre-computation of velocity dealiasing rules

---

This method is described in the paper “Design, Implementation, and Demonstration of a Staggered PRT Algorithm for the WSR-88D” by Torres et al. (2004). Herein,  $VDA_c$  are the normalized velocity difference transfer function (VDTF) constant values and  $VDA_p$  are the normalized number of Nyquist co-intervals for dealiasing.

A set of velocity dealiasing rules is pre-computed at the initiation of the SPRT algorithm as follows:

*(Compute type-I and II positive VDTF discontinuity points.  $\kappa_m$  and  $\kappa_n$  are the integers in the PRT ratio)*

$p = 0$

While  $2p + 1 < \kappa_m$

$$D_1(p) = (2p + 1)/\kappa_m$$

$$TYPE_1(p) = 1$$

$$p = p + 1$$

End

$q = 0$

While  $2q + 1 < \kappa_n$

$$D_2(q) = (2q + 1)/\kappa_n$$

$$TYPE_2(q) = 2$$

$$q = q + 1$$

End

*(Create TYPE by combining and sorting both sets of discontinuity points)*

Concatenate  $D_1$  and  $D_2$  to create  $D$  with  $p + q$  elements.

Concatenate  $TYPE_1$  and  $TYPE_2$  to create  $TYPE$  with  $p + q$  elements.

Sort  $TYPE$  in a “slave” mode using  $D$  as the “master”.

*(Compute VDTF constants and dealiasing factors for non-negative discontinuity points)*

$$VDA_c(p + q) = 0$$

$$VDA_p(p + q) = 0$$

For  $0 \leq k < p + q$

If  $TYPE(k) = 1$

$$VDA_c(p + q + k + 1) = VDA_c(p + q + k) - 2/\kappa_m$$

$$VDA_p(p + q + k + 1) = VDA_p(p + q + k) + 1/\kappa_m$$

Else

$$VDA_c(p + q + k + 1) = VDA_c(p + q + k) + 2/\kappa_n$$

$$VDA_p(p + q + k + 1) = VDA_p(p + q + k)$$

End

End

(Compute VDTF constants and dealiasing factors for negative discontinuity points)

For  $-(p+q) \leq k < 0$

$$VDA_c(p+q+k) = -VDA_c(p+q-k)$$

$$VDA_p(p+q+k) = -VDA_p(p+q-k)$$

End

(Note that since the PRT ratio does not change, these vectors can be hard-coded in a real-time implementation of the SPRT algorithm.)

## 2. Pre-computation of M-independent SACHI filter parameters

---

This method is described in NSSL Signal Design and Processing Techniques for WSR-88D Ambiguity Resolution (Report 3, Report 9 and Report 11). The SACHI filter parameters could be pre-computed at the initiation of the SPRT algorithm as follows:

(Create 5-by-5 convolution matrix,  $\mathbf{C}_r$ )

$$\mathbf{C}_r = \begin{bmatrix} C(0) & C(4) & C(3) & C(2) & C(1) \\ C(1) & C(0) & C(4) & C(3) & C(2) \\ C(2) & C(1) & C(0) & C(4) & C(3) \\ C(3) & C(2) & C(1) & C(0) & C(4) \\ C(4) & C(3) & C(2) & C(1) & C(0) \end{bmatrix} = [\mathbf{C}_{r,1} \quad \mathbf{C}_{r,2} \quad \mathbf{C}_{r,3} \quad \mathbf{C}_{r,4} \quad \mathbf{C}_{r,5}],$$

where  $C(k) = \frac{1}{\sqrt{10}} \sum_{n=0}^4 c(n) \exp(-j2\pi nk/5)$ ; for  $0 \leq k < 5$  and  $\mathbf{c} = [1, 0, 1, 0, 0]$ , and  $\mathbf{C}_{r,k}$  is the  $k$ -th column of  $\mathbf{C}_r$ .

(Calculate magnitude deconvolution matrix,  $\mathbf{C}_{md}$ )

(Note: The following formulas are written in matrix algebra notation with the conventions described above)

$$\mathbf{C}_{md} = |\mathbf{C}_r|^{-1} = \begin{bmatrix} \mathbf{C}_{md,1} \\ \mathbf{C}_{md,2} \\ \mathbf{C}_{md,3} \\ \mathbf{C}_{md,4} \\ \mathbf{C}_{md,5} \end{bmatrix} = \begin{bmatrix} -4.6281 & -2.0697 & 4.6281 & 4.6281 & -2.0697 \\ -2.0697 & -4.6281 & -2.0697 & 4.6281 & 4.6281 \\ 4.6281 & -2.0697 & -4.6281 & -2.0697 & 4.6281 \\ 4.6281 & 4.6281 & -2.0697 & -4.6281 & -2.0697 \\ -2.0697 & 4.6281 & 4.6281 & -2.0697 & -4.6281 \end{bmatrix},$$

where  $\mathbf{C}_{md,k}$  is the  $k$ -th row of  $\mathbf{C}_{md}$ .

(Calculate matrices  $\mathbf{C}_{f1}$  and  $\mathbf{C}_{f2}$  using 1<sup>st</sup> and 5<sup>th</sup> columns of  $\mathbf{C}_r$ )

$$\mathbf{C}_{f1} = \mathbf{C}_{r,1} \mathbf{C}_{r,1}^{*T} = \begin{bmatrix} 0.4 & 0.0382 + j0.1176 & 0.2618 - j0.1902 & 0.2618 + j0.1902 & 0.0382 - j0.1176 \\ 0.0382 - j0.1176 & 0.0382 & -0.0309 - j0.0951 & 0.0809 - j0.0588 & -0.0309 - j0.0225 \\ 0.2618 + j0.1902 & -0.0309 + j0.0951 & 0.2681 & 0.0809 + j0.2490 & 0.0809 - j0.0588 \\ 0.2618 - j0.1902 & 0.0809 + j0.0588 & 0.0809 - j0.2490 & 0.2618 & -0.0309 - j0.0951 \\ 0.0382 + j0.1176 & -0.0309 + j0.0225 & 0.0809 + j0.0588 & -0.0309 + j0.0951 & 0.0382 \end{bmatrix}$$

$$\mathbf{C}_{f2} = \mathbf{C}_{r,5} \mathbf{C}_{r,5}^{*T} = \begin{bmatrix} 0.0382 & -0.0309 - j0.0951 & 0.0809 - j0.0588 & -0.0309 - j0.0225 & 0.0382 - j0.1176 \\ -0.0309 + j0.0951 & 0.2618 & 0.0809 + j0.249 & 0.0809 - j0.0588 & 0.2618 + j0.1902 \\ 0.0809 + j0.0588 & 0.0809 - j0.249 & 0.2618 & -0.0309 - j0.0951 & 0.2618 - j0.1902 \\ -0.0309 + j0.0225 & 0.0809 + j0.0588 & -0.0309 + j0.0951 & 0.0382 & 0.0382 + j0.1176 \\ 0.0382 + j0.1176 & 0.2618 - j0.1902 & 0.2618 + j0.1902 & 0.0382 - j0.1176 & 0.4 \end{bmatrix}$$

where  $*T$  stands for the matrix conjugate transpose (a.k.a. Hermitian) operation.

(Calculate the correction coefficients  $\xi_2$  and  $\xi_3$  for correction vector  $\mathbf{X}$ )

$$\xi_k = \frac{1}{\mathbf{C}_{md,1} \left| \mathbf{C}_{r,k} - (\mathbf{C}_{r,1}^{*T} \mathbf{C}_{r,k}) \mathbf{C}_{r,1} \right|}; k = 2, 3.$$

$$\xi_2 = 1.1056 \text{ and } \xi_3 = 1.7889.$$

(Note: since the PRT ratio does not change, these matrices and coefficients can be hard-coded in a real-time implementation of the SPRT algorithm. The numbers provided here are for reference purposes only; the highest precision available is recommended for hard-coding these numbers.)

### 3. Pre-computation of window parameters

---

(Calculate the extended number of coefficients)

$$M_x = 5M / 2$$

(Calculate the number of pulse pairs)

$$M_p = M / 2$$

(Calculate normalized window  $d$  for un-normalized window function  $d'$  with  $M_x$  points)

$$d(m) = d'(m) \left( \sqrt{\frac{1}{M_x} \sum_{m=0}^{M_x-1} [d'(m)]^2} \right)^{-1}; 0 \leq m < M_x.$$

(Calculate window correction factor for lag-1)

$$d_c = \frac{1}{M_x} \sum_{m=0}^{M_x-2} d(m)d(m+1)$$

#### 4. Pre-computation of $M$ -dependent SACHI filter parameters

---

(Compute correction vector,  $\mathbf{X}$ )

For  $0 \leq k < \text{ceiling}(M_p/2)$

$$X(k) = 1$$

End

For  $\text{ceiling}(M_p/2) \leq k < \text{ceiling}(M_p/2) + M_p$

$$X(k) = \zeta_2$$

End

For  $\text{ceiling}(M_p/2) + M_p \leq k < \text{ceiling}(M_p/2) + 3M_p$

$$X(k) = \zeta_3$$

End

For  $\text{ceiling}(M_p/2) + 3M_p \leq k < \text{ceiling}(M_p/2) + 4M_p$

$$X(k) = \zeta_2$$

End

For  $\text{ceiling}(M_p/2) + 4M_p \leq k < M_x$

$$X(k) = 1$$

End

#### 5. Short-PRT Segment-III Data Reconstruction

---

Long-PRT Segment-I data is used as a proxy for short-PRT segment-III data

For  $0 \leq m < M_p$

$$V(n, 2m) = V(n - N_1, 2m + 1)$$

End

#### 6. SACHI Clutter Filtering

---

The SACHI filter algorithm is used when clutter filtering is required inside the maximum unambiguous range corresponding to  $T_1(r_{a1})$ .

(Form derived time series,  $V_d$ , from input time series  $V$ )

For  $0 \leq m < M_p$

$$V_d(5m) = V(n, 2m)$$

$$V_d(5m + 1) = 0$$

$$V_d(5m + 2) = V(n, 2m + 1)$$

$$V_d(5m + 3) = 0$$

$$V_d(5m + 4) = 0$$

End

(Compute DFT of windowed extended time series power compensated for added zeroes)

$$F(k) = \left( \sqrt{\frac{5}{2}} \right) \left( \frac{1}{M_x} \sum_{m=0}^{M_x-1} V_d(m) d(m) \exp(-j2\pi km / M_x) \right); k = 0, 1, \dots, M_x - 1.$$

(Determine clutter filter width parameter,  $q$ )  
 (Use GMAP to return the number of coefficients identified as clutter,  $GMAP_{coef}$ . Pass to GMAP the 5<sup>th</sup> of the Doppler spectrum containing the main clutter replica; i.e.,  $\{|F(0)|^2, \dots, |F[\text{ceiling}(M_p/2) - 1]|^2, |F[M_x - \text{floor}(M_p/2)]|^2, \dots, |F(M_x - 1)|^2\}$ ; initialize GMAP for spectra with  $v_d/5$ , and get the number of coefficients identified as clutter to estimate  $q$ )  
 $q = \text{floor} [(GMAP_{coef} + 1)/2]$

(Create clutter filter vectors,  $\mathbf{I}_{f1}$ ,  $\mathbf{I}_{f2}$ ,  $\mathbf{I}_1$ , and  $\mathbf{I}_2$ )

For  $0 \leq k < M_p$

  If  $k < q$

$$I_{f1}(k) = 1$$

$$I_{f2}(k) = 0$$

$$I_1(k) = 0$$

$$I_1(k + M_p) = 0$$

$$I_1(k + 2M_p) = 0$$

$$I_1(k + 3M_p) = 0$$

$$I_1(k + 4M_p) = 0$$

$$I_2(k) = 1$$

$$I_2(k + M_p) = 1$$

$$I_2(k + 2M_p) = 1$$

$$I_2(k + 3M_p) = 1$$

$$I_2(k + 4M_p) = 1$$

  ElseIf  $k \leq M_p - q$

$$I_{f1}(k) = 0$$

$$I_{f2}(k) = 0$$

$$I_1(k) = 1$$

$$I_1(k + M_p) = 1$$

$$I_1(k + 2M_p) = 1$$

$$I_1(k + 3M_p) = 1$$

$$I_1(k + 4M_p) = 1$$

$$I_2(k) = 0$$

$$I_2(k + M_p) = 0$$

$$I_2(k + 2M_p) = 0$$

$$I_2(k + 3M_p) = 0$$

$$I_2(k + 4M_p) = 0$$

  Else

$$I_{f1}(k) = 0$$

$$I_{f2}(k) = 1$$

$$I_1(k) = 0$$

$$I_1(k + M_p) = 0$$

$$I_1(k + 2M_p) = 0$$

$$I_1(k + 3M_p) = 0$$

$$I_1(k + 4M_p) = 0$$

$$I_2(k) = 1$$

$$I_2(k + M_p) = 1$$

$$I_2(k + 2M_p) = 1$$

$$I_2(k + 3M_p) = 1$$

$$I_2(k + 4M_p) = 1$$

End

End

(Row-wise re-arrange  $F$  into a 5-by- $M_p$  matrix,  $\mathbf{F}_r$ )

For  $0 \leq k < M_p$

$$F_r(0, k) = F(k)$$

$$F_r(1, k) = F(k + M_p)$$

$$F_r(2, k) = F(k + 2M_p)$$

$$F_r(3, k) = F(k + 3M_p)$$

$$F_r(4, k) = F(k + 4M_p)$$

End

(Compute the clutter filtered spectrum matrix,  $\mathbf{F}_f$ )

(Note: The following formulas are written in matrix algebra notation. Complex-matrix multiplications can be implemented using four real-matrix multiplications as:

$$\mathbf{A}\mathbf{B} = (\mathbf{A}_r + j\mathbf{A}_i)(\mathbf{B}_r + j\mathbf{B}_i) = (\mathbf{A}_r\mathbf{B}_r - \mathbf{A}_i\mathbf{B}_i) + j(\mathbf{A}_r\mathbf{B}_i + \mathbf{A}_i\mathbf{B}_r)$$

$$\mathbf{F}_f = \mathbf{F}_r - \mathbf{C}_{n1}\mathbf{F}_r \text{diag}(\mathbf{I}_{n1}) - \mathbf{C}_{n2}\mathbf{F}_r \text{diag}(\mathbf{I}_{n2})$$

(Magnitude deconvolved matrix,  $\mathbf{F}_d$ )

$$\mathbf{F}_d = \mathbf{C}_{md} |\mathbf{F}_f|$$

(Row-wise unfold  $\mathbf{F}_d$  into  $F_{df}$ )

For  $0 \leq k < M_p$

$$F_{df}(k) = F_d(0, k)$$

$$F_{df}(k + M_p) = F_d(1, k)$$

$$F_{df}(k + 2M_p) = F_d(2, k)$$

$$F_{df}(k + 3M_p) = F_d(3, k)$$

$$F_{df}(k + 4M_p) = F_d(4, k)$$

End

(Compute the lag-1 autocorrelation,  $R_{1df}$ )

$$R_{1df} = \frac{1}{d_c} \sum_{k=0}^{M_x-1} |F_{df}(k)|^2 \exp(j2\pi k / M_x)$$

(Compute vector  $\mathbf{I}_v$  with  $M/2$  ones centered on  $\arg(R_{1df})$ )

(Round to the nearest spectral coefficient. Choose symmetric window of coefficients around it)

$$k_{0df} = \text{round} \left[ \frac{M_x \arg(R_{1df})}{2\pi} \right]$$

If  $k_{0df} < 0$

$$k_{0df} = k_{0df} + M_x$$

```

End
If  $k_{0df} \geq M_x$ 
     $k_{0df} = k_{0df} - M_x$ 
End
 $k_{1df} = k_{0df} - \text{floor}(M / 4)$ 
If  $k_{1df} < 0$ 
     $k_{1df} = k_{1df} + M_x$ 
End
 $k_{2df} = k_{0df} + \text{ceiling}(M / 4) - 1$ 
If  $k_{2df} \geq M_x$ 
     $k_{2df} = k_{2df} - M_x$ 
End

```

*( $k_{0df}$  is the coefficient corresponding to  $\arg(R_{1df})$ ,  $k_{1df}$  and  $k_{2df}$  specify the extent of  $M_p$  spectral coefficients centered on the mean velocity. If  $k_{1df} < k_{2df}$ , the ones span from  $k_{1df}$  to  $k_{2df}$ ; otherwise, the ones will span from  $k_{1df}$  to  $M_x - 1$ , and 0 to  $k_{2df}$ )*

```

If  $k_{1df} < k_{2df}$ 
    For  $0 \leq k < M_x$ 
        If  $k < k_{1df}$  OR  $k > k_{2df}$ 
             $I_v(k) = 0$ 
        Else
             $I_v(k) = 1$ 
        End
    End
Else
    For  $0 \leq k < M_x$ 
        If  $k < k_{1df}$  AND  $k > k_{2df}$ 
             $I_v(k) = 0$ 
        Else
             $I_v(k) = 1$ 
        End
    End
End

```

*(Interpolate the elements for the region around zero velocity in  $F_{df}$  with linearly interpolated values from  $S_1$  and  $S_2$ )*

```

If  $q > 0$ 
     $S_1 = |F_{df}(q)|^2$ 
     $S_2 = |F_{df}(M_x - q)|^2$ 
    For  $0 \leq k < M_x$ 
        If  $k < q$ 
             $F_i(k) = [S_2 + (S_1 - S_2) (q + k) / 2q]^{1/2}$ 
        ElseIf  $k > M_x - q$ 

```

$$F_i(k) = \left[ S_2 + (S_1 - S_2) (q + k - M_x) / 2q \right]^{1/2}$$

Else

$$F_i(k) = F_{df}(k)$$

End

End

Else

*(Don't interpolate if not needed)*

For  $0 \leq k < M_x$

$$F_i(k) = F_{df}(k)$$

End

End

*(Compute the corrected spectrum,  $F_c$ )*

For  $0 \leq k < M_x$

$$F_c(k) = F_i(k) I_1(k) + F_i(k) I_2(k) I_v(k) X(k)$$

End

*(Compute vector  $\mathbf{I}_c$  with ones where there's a non-zero spectral component in vector  $\mathbf{F}_c$ )*

For  $0 \leq k < M_x$

$$I_c(k) = I_1(k) + I_2(k) I_v(k)$$

End

*(Compute the mean power,  $P_c$ , and autocorrelation at lag  $T_w$ ,  $R_{1c}$ , using  $F_c$ )*

$$P_c = \sum_{k=0}^{M_x-1} |F_c(k)|^2$$

$$R_{1c} = \frac{1}{d_c} \sum_{k=0}^{M_x-1} |F_c(k)|^2 \exp(j2\pi k / M_x)$$

*(Retain only  $M$  coefficients centered on velocity based on  $R_{1c}$  and delete the rest from  $F_c$  and  $I_c$ )*

$$k_{0c} = \text{round} \left[ \frac{M_x \arg(R_{1c})}{2\pi} \right]$$

If  $k_{0c} < 0$

$$k_{0c} = k_{0c} + M_x$$

End

If  $k_{0c} \geq M_x$

$$k_{0c} = k_{0c} - M_x$$

End

$$k_{1c} = k_{0c} - M_p$$

If  $k_{1c} < 0$

$$k_{1c} = k_{1c} + M_x$$

End

$$k_{2c} = k_{0c} + M_p - 1$$

```

If  $k_{2c} \geq M_x$ 
     $k_{2c} = k_{2c} - M_x$ 
End
If  $k_{1c} < k_{2c}$ 
    For  $0 \leq k < M_x$ 
        If  $k < k_{1c}$  OR  $k > k_{2c}$ 
             $F_m(k) = 0$ 
             $I_m(k) = 0$ 
        Else
             $F_m(k) = F_c(k)$ 
             $I_m(k) = I_c(k)$ 
        End
    End
End
Else
    For  $0 \leq k < M_x$ 
        If  $k < k_{1c}$  AND  $k > k_{2c}$ 
             $F_m(k) = 0$ 
             $I_m(k) = 0$ 
        Else
             $F_m(k) = F_c(k)$ 
             $I_m(k) = I_c(k)$ 
        End
    End
End
End

```

(Compute the modified mean power,  $P_m$ , and autocorrelation at lag  $T_w$ ,  $R_{1m}$ , using  $F_m$ )

$$P_m = \sum_{k=0}^{M_x-1} |F_m(k)|^2$$

$$R_{1m} = \frac{1}{d_c} \sum_{k=0}^{M_x-1} |F_m(k)|^2 \exp(j2\pi k/M_x)$$

(Compute noise correction factors)

$$N_c = \frac{1}{M_x} \sum_{k=0}^{M_x-1} I_c(k)$$

$$N_m = \frac{1}{M_x} \sum_{k=0}^{M_x-1} I_m(k)$$

(Compute overlaid power correction if in segment I)

```

If  $n < N_2 - N_1$ 
    
$$S_{ov} = \frac{1}{2} \left[ \frac{1}{M_p} \sum_{m=0}^{M_p-1} |V(n + N_1, 2m + 1)|^2 - Noise \right]$$

    If  $S_{ov} < 0$ 
         $S_{ov} = 0$ 
    End
End

```

End  
Else  
 $S_{ov} = 0$   
End

*(Correct powers to remove overlaid contamination adjusted for each spectrum)*

$$P_m = P_m - N_m S_{ov}$$

If  $P_m < 0$

$$P_m = 0$$

End

$$P_c = P_c - N_c S_{ov}$$

If  $P_c < 0$

$$P_c = 0$$

End

*(Compute spectrum width power ratio adjustment)*

$$S_m = P_m - N_m \text{Noise}$$

If  $S_m < 0$

$$S_m = 0$$

End

If  $S_m > 0$

$$P_{adj} = \frac{|R_{1m}|}{S_m}$$

Else

$$P_{adj} = 0$$

End

*(Compute signal power)*

$$S_c = P_c - N_c \text{Noise}$$

If  $S_c < 0$

$$S_c = 0$$

End

*(Compute short PRT autocorrelation at lag  $T_1$ )*

$$R_1(n) = S \cdot P_{adj}^4 \exp[j2\arg(R_{1c})]$$

*(Compute long PRT autocorrelation at lag  $T_2$ )*

$$R_2(n) = S \cdot P_{adj}^9 \exp[j3\arg(R_{1c})]$$

*(Adjust signal power to include noise)*

$$P(n) = S_c + \text{Noise}$$

*(Note that the outputs of SACHI are  $P(n)$ ,  $R_1(n)$  and  $R_2(n)$ )*

### 7. DC Removal Clutter Filtering (Segment-III gate with segment-I clutter)

---

This DC Removal clutter filtering algorithm removes the mean (DC) component of the short-PRT segment-III gates in those locations where the site-dependent clutter filter bypass map  $B$  indicates the need for clutter within segment I.

(Calculate the mean of the even pulses.)

$$V_m = \frac{1}{M_p} \sum_{m=0}^{M_p-1} V(n, 2m)$$

(Subtract mean from even pulses.)

For  $0 \leq m < M_p$

$$V_F(2m) = V(n, 2m) - V_m$$

$$V_F(2m+1) = V(n, 2m+1)$$

End

### 8. No Clutter Filtering

---

For  $0 \leq m < M$

$$V_F(m) = V(n, m)$$

End

### 9. Power and correlation computations for each PRT

---

If  $n < N_1$

(Compute power from even pulses, if available)

$$P_1 = \frac{1}{M_p} \sum_{m=0}^{M_p-1} |V_F(2m)|^2$$

End

(Compute power from odd pulses, if available)

$$P_2 = \frac{1}{M_p} \sum_{m=0}^{M_p-1} |V_F(2m+1)|^2$$

(Compute lag-1 correlations from all pulses)

$$R_1(n) = \frac{1}{M_p} \sum_{m=0}^{M_p-1} V_F^*(2m)V_F(2m+1)$$

$$R_2(n) = \frac{1}{M_p-1} \sum_{m=0}^{M_p-2} V_F^*(2m+1)V_F(2m+2)$$

## 10. Combined power computation

---

To use as much information as possible, data are extracted from the two power arrays with different rules for each of the three segments depicted in Fig. A.1. For segment I, data are extracted only from  $P_1$ , since  $P_2$  may be contaminated on those range bins with overlaid powers. An average of  $P_1$  and  $P_2$  is extracted for segment II, given that both power vectors are “clean” there. Finally, segment III data are obtained from  $P_2$ . In algorithmic form:

```
If  $n < N_2 - N_1$ 
  (Segment I)
   $P(n) = P_1$ 
ElseIf  $n < N_1$ 
  (Segment II)
   $P(n) = \frac{1}{2}(P_1 + P_2)$ 
Else
  (Segment III)
   $P(n) = P_2$ 
End
```

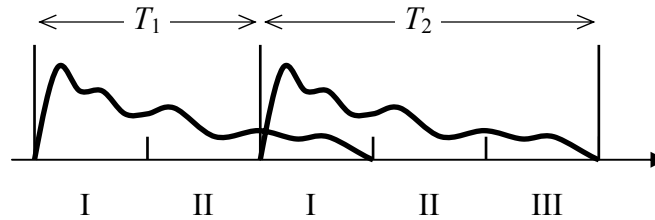


Fig. A.1. Signal powers in the staggered PRT algorithm. Roman numerals indicate segment numbers.

## 11. Strong point clutter canceling

---

Processing is as in the current system. Strong-point clutter canceling is applied to  $P$ ,  $R_1$  and  $R_2$  based on radial power continuity in  $P$ . For the remainder of the algorithm it is assumed that the outputs of this step are  $P$ ,  $R_1$  and  $R_2$ .

## 12. Signal power computation

---

If  $P(n) < \text{Noise}$   
     $S = 0$   
Else  
     $S = P(n) - \text{Noise}$   
End

## 13. Reflectivity computation

---

*(Range in km)*

$$R = n\Delta R + \Delta R/2$$

*(Reflectivity in dBZ.  $\log_{10}$  is the base-10 logarithm)*

If  $S > 0$   
     $Z(n) = 10\log_{10}(S) + \text{dBZ0} + R \text{ ATMOS} + 20\log_{10}(R) - 10\log_{10}(\text{Noise})$ ,  
Else  
     $Z(n)$  should be set to the smallest possible reflectivity value  
End

## 14. Velocity computation

---

*(Compute Doppler velocities for each PRT using the corresponding correlation estimates)*

$$v_1 = -\frac{\lambda}{4\pi T_1} \arg[R_1(n)], \quad v_2 = -\frac{\lambda}{4\pi T_2} \arg[R_2(n)]$$

*(Compute extended Nyquist velocity)*

$$v_a = \frac{\lambda}{2T_1}$$

*(Dealias velocity using pre-computed rules)*

$$l = \arg \min_k |v_1 - v_2 - VDA_c(k)v_a|$$

$$v(n) = v_1 + 2v_a VDA_p(l)$$

*(Prevent dealiased velocities outside of the extended Nyquist co-interval)*

If  $v(n) > v_a$   
     $v(n) = v(n) - 2v_a$

End

If  $v(n) < -v_a$   
     $v(n) = v(n) + 2v_a$

End

### 15. Spectrum width computation

---

The spectrum width estimator corresponds to the algorithm implemented in the legacy WSR-88D signal processor.

If  $S = 0$  OR  $|R_1(n)| = 0$

*(Insert spectrum width of white noise)*

$$w(n) = \frac{\lambda}{4\sqrt{3}T_1}$$

ElseIf  $S < |R_1(n)|$

*(Insert spectrum width of a constant)*

$$w(n) = 0$$

Else

*(Spectrum width computation. ln is the natural logarithm)*

$$w(n) = \frac{\lambda}{2\sqrt{2}\pi T_1} \sqrt{\ln\left(\frac{S}{|R_1(n)|}\right)}$$

If  $w(n) = \frac{\lambda}{4\sqrt{3}T_1}$

*(Saturation of the spectrum width)*

$$w(n) = \frac{\lambda}{4\sqrt{3}T_1}$$

End

End

### 16. Determination of significant returns for reflectivity

---

The non-significant return indicator array ( $NS_Z$ ) is a binary array where 0 indicates “significant” and 1 indicates “non-significant”

If  $S < Noise \cdot 10^{0.1T_z}$

$$NS_Z(n) = 1$$

Else

$$NS_Z(n) = 0$$

End

### 17. Determination of significant returns for velocity

---

The non-significant return indicator array ( $NS_V$ ) is a binary array where 0 indicates “significant” and 1 indicates “non-significant”

If  $S < Noise \cdot 10^{0.1T_V}$

$$NS_V(n) = 1$$

Else

$$NS_V(n) = 0$$

End

### 18. Determination of significant returns for spectrum width

---

The non-significant return indicator array ( $NS_W$ ) is a binary array where 0 indicates “significant” and 1 indicates “non-significant”

If  $S < Noise \cdot 10^{0.1T_W}$

$$NS_W(n) = 1$$

Else

$$NS_W(n) = 0$$

End

### 19. Determination of overlaid returns for velocity and spectrum width

---

Censoring of velocity and spectrum width data is only necessary in segments I and III. This is done by analyzing  $P$  in segment I ( $P_1$ ) and  $P$  in segment III ( $P_2$ ) (see Fig. 1). The idea is to determine whether second trip signals mask first trip signals and vice versa. While such overlaid echoes appear in every other pulse and do not bias velocity estimates at those range locations, overlaid powers act as noise. Therefore, when overlaid powers are above a preset fraction of their non-overlaid counterparts, the corresponding velocity and spectrum width estimates exhibit very large errors and must be censored. The overlaid indicator arrays ( $OV_V$  and  $OV_W$ ) are binary arrays where 0 indicates “not overlaid” and 1 indicates “overlaid”.

If  $n < N_2 - N_1$

*(Segment I: Range gates that may or may not have overlaid echoes)*

*(Check power ratio using velocity threshold)*

If  $P(n) > P(n + N_1) 10^{0.1T_{OV}}$

$$OV_V(n) = 0$$

Else

*(Power ratio not met, but consider non-significant returns as non-existent)*

If  $NS_V(n + N_1) = 1$

$$OV_V(n) = 0$$

Else

$$OV_V(n) = 1$$

End

```

End
(Check power ratio using width threshold)
If  $P(n) > P(n + N_1) 10^{0.1T_{ow}}$ 
     $OV_W(n) = 0$ 
Else
    (Power ratio not met, but consider non-significant returns as non-existent)
    If  $NS_W(n + N_1) = 1$ 
         $OV_W(n) = 0$ 
    Else
         $OV_W(n) = 1$ 
    End
End
End
ElseIf  $n < N_1$ 
    (Segment II: Range gates that, based on the assumptions, never have overlaid echoes)
     $OV_V(n) = 0$ 
     $OV_W(n) = 0$ 
Else
    (Segment III: Range gates that may or may not have overlaid echoes)
    (Check power ratio using velocity threshold)
    If  $P(n) > P(n - N_1) 10^{0.1T_{ov}}$ 
         $OV_V(n) = 0$ 
    Else
        (Power ratio not met, but consider non-significant returns as non-existent)
        If  $NS_V(n - N_1) = 1$ 
             $OV_V(n) = 0$ 
        Else
             $OV_V(n) = 1$ 
        End
    End
End
End
(Check power ratio using width threshold)
If  $P(n) > P(n - N_1) 10^{0.1T_{ow}}$ 
     $OV_W(n) = 0$ 
Else
    (Power ratio not met, but consider non-significant returns as non-existent)
    If  $NS_W(n - N_1) = 1$ 
         $OV_W(n) = 0$ 
    Else
         $OV_W(n) = 1$ 
    End
End
End
End

```

*(Note that when processing the overlaid and significant return flags, the overlaid flags take a lower priority. That is, if a range bin is tagged as non significant and also as overlaid, the overlaid indication is ignored and the gate is treated as a non-significant return only; e.g., painted black as opposed to purple)*



## **Appendix B. Bias in differential reflectivity due to cross-coupling through the radiation patterns in the simultaneous horizontal/vertical polarization mode<sup>1</sup>**

### **B.1. Abstract**

Examined is bias in differential reflectivity and its effect on estimates of rain rate due to coupling of the vertically and horizontally polarized fields through the radiation patterns. To that end a brief review of the effects of the bias on classification of hydrometeors and on quantitative rainfall measurements is given. Suggestions for tolerable values of this bias are made. Of utmost interest is the bias produced by radar simultaneously transmitting horizontally and vertically polarized fields, as this configuration has been chosen for the USA national network of radars (WSR-88D). The bias strongly depends on the type of cross-polar radiation pattern. Two patterns, documented in the literature, are considered.

### **B.2. Introduction**

The preferred embodiment of dual linear polarization technology on weather radars is the mode whereby horizontal (H) and vertical (V) polarizations are transmitted and received simultaneously (Doviak et al. 2000). This mode is sometimes referred to as “hybrid” (Wang et al. 2006); to shorten notation we label it SHV (Simultaneous Horizontal and

---

<sup>1</sup> This Appendix was written by Dusan Zrnica, Richard Doviak, Guifu Zhang, and Alexander Ryzhkov

Vertical). The USA National Weather Service is slated to begin retrofitting its WSR-88Ds with this mode in about 2010. By far, the overriding reason for choosing the SHV mode is its total transparency to all the current automated algorithms used in the radar network. That is, algorithms to detect mesocyclones and tornadoes, track storms, etc., will continue to accept data from the horizontal channel, process these, and produce products as is presently done (Doviak and Zrnic 1998). The only minor difference is a 3 dB loss in Signal to Noise (SNR) ratio, but the effect of this loss on algorithm performance will be mitigated by using thresholds that depend on signal coherency (Ivić et al. 2009).

Advantages of the SHV mode are: 1) direct measurement of the cross correlation between the copolar signals, 2) 360° unambiguous span for differential phase measurement, 3) decoupling of the differential phase and Doppler velocity measurements, 4) smaller error of estimates, 5) no degradation of the performance of the ground clutter filters, and 6) avoidance of a high power microwave ferrite switch and its associated problems. Nonetheless there are also disadvantages. For example, Sachidananda and Zrnic (1985) show that bias errors in differential reflectivity can be an order of magnitude larger if estimates are made using the SHV mode rather than alternately transmitting, but simultaneously receiving H, V waves (i.e., the AHV mode). Furthermore, the SHV mode is more affected by coupling between the copolar and cross-polar fields, and it does not offer any protection against even multiple trip overlays as does the AHV mode. Finally, the SHV mode is not fully polarimetric because it precludes cross-polar measurements. On the other hand, cross-polar SNR (measured using the AHV mode) is typically weak, and thus its measurement is limited to high reflectivity regions.

The effects of cross-coupling within the radar, of feed horn misalignment, and of hydrometeor canting on the polarimetric variables have been quantified by Doviak and Zrníc (1998) and Doviak et al. (2000). These authors also presented the copolar and cross-polar radiation patterns made on NSSL's R&D WSR-88D (i.e., KOUN), but did not quantify polarimetric parameter bias due to the coupling between copolar and cross-polar patterns.

The effects of radiation pattern cross-coupling on the measurement of polarimetric variables were first examined by Chandrasekar and Keeler (1993), specifically for the AHV mode. A detailed investigation and explanation of the effects of cross-coupling on weather echoes is presented in the paper by Moisseev et al. (2002), who argue in favor of incorporating the patterns into a calibration procedure using vertical incident measurements in light rain. Although cross-polar radiation affects the accuracy of polarimetric measurements, neither paper address these accuracies if the SHV mode is used.

Even if there is no coupling between the H and V channels within the radar and its antenna, measurements of polarimetric parameters using the SHV mode are affected by depolarization due to propagation through oriented scatterers (Ryzhkov and Zrníc 2007). The effects for various type of precipitation were thoroughly investigated by Wang et al. (2006), who indicate that biases in all polarimetric variables increase due to increases of the cross-polarized echoes.

Differential reflectivity  $Z_{DR}$  (Seliga and Bringi 1976) and specific differential phase  $K_{DP}$  (Sachidananda and Zrníc 1987) have been proposed for quantitative precipitation

measurements and both are included in an algorithm accepted for implementation on the polarimetric WSR-88D (Ryzhkov et al. 2005b). Although the magnitude of the cross correlation coefficient  $\rho_{hv}$  is related to rain rate (Sachidananda and Zrnica 1985, Fig. 7) its value for quantitative measurement is marred by insufficient sensitivity. Because  $Z_{DR}$  is a principal variable for estimating rain rate, and because it is more prone to bias than  $\rho_{hv}$  and  $K_{DP}$ , we examine herein the effects on the  $Z_{DR}$  measurements caused by coupling between the copolar and cross-polar patterns.

Hubbert et al. (2009) have evaluated  $Z_{DR}$  bias caused by depolarizing media. However, even if media are not depolarizing (e.g., propagation paths filled with oblate drops having a vertical axis of symmetry), differential phase shift caused by precipitation along the propagation path will influence the level of  $Z_{DR}$  bias. They have also computed the bias caused by cross-polar to copolar pattern coupling assumed to be constant over the significant part of the copolar pattern. Under the assumption of uniform coupling, Hubbert et al. (2009) were also able to relate pattern coupling to the lower limit of linear depolarization ratio measurements. These results are backed by experiment indicating  $Z_{DR}$  bias (up to 0.27 dB) observed in the SHV mode is much larger compared to that observed in the AHV mode.

Wang and Chandrasekhar (2006) investigated biases in the polarimetric variables caused by the cross-polar pattern. They have developed pertinent equations building on the formalism in Bringi and Chandrasekhar (2001) and quantified biases for a wide range of general conditions. Moreover they present curves for the upper bounds of the errors as function of precipitation type. In its essence their formalism and ours are equivalent. We examine causes of cross-polar radiation and reduce the theoretical expressions of  $Z_{DR}$  bias

to simple compact form. Then, to quantify the effects we approximate radiation patterns with Gaussian shapes for two types of common cross-polar radiation. Applying the methodology to these patterns we obtain dependence of error bounds on copolar and cross polar radiation and the differential reflectivity itself.

Biases in differential reflectivity caused by cross-polar to copolar radiation coupling are examined with the aim to set reasonable limits on cross-polar radiation. In section 2 we set and justify a bound to the  $Z_{DR}$  bias based on the accuracy of rain rate measurements, and use that bound to derive limits on the cross-polar radiation pattern. Section 3 quantifies the relation between cross-polar coupling and bias for practical patterns and includes examples of measured cross-polar patterns. Section 4 compares the bias in the SHV and AHV modes.

### **B.3. Effects of the bias on Rain Rate Measurements**

Accurate polarimetric measurement has two purposes. One is to allow correct classification of precipitation, and the other is to improve quantitative precipitation estimation. In fuzzy logic classification (Zrnich et al. 2001), performance depends on  $Z_{DR}$  through the membership (weighting) functions  $W_i(Z, Z_{DR}, \text{etc.})$ . The effects of the  $Z_{DR}$  bias on classification can be easily mitigated by appropriately broadening the membership functions. Therefore accurate rainfall measurement imposes a more stringent requirement on the bias of  $Z_{DR}$ .

To compute light rain rates (i.e.,  $< 6 \text{ mm h}^{-1}$ ) the following relation has been proposed for the network of WSR-88Ds (Ryzhkov et al. 2005a),

$$R = \frac{1.70 \times 10^{-2} Z_h^{0.714}}{0.4 + 5.0 |Z_{dr} - 1|^{1.3}} \text{ (mm h}^{-1}\text{)}, \quad (1)$$

where  $Z_h$  is in units of  $\text{mm}^6 \text{ m}^{-3}$ ,  $Z_H(\text{dB}) < 36 \text{ dBZ}$ ,  $Z_{dr} = 10^{0.1Z_{DR}}$ , and  $Z_{DR}$  is in dB. We have focused attention to this rain rate regime because it is affected more by  $Z_{DR}$  bias. Assuming no error in  $Z_h$ , the fractional bias,  $\Delta R/R$ , in rain rate is,

$$\Delta R/R = f(Z_{DR})/f(Z_{DRb}) - 1, \quad (2a)$$

where

$$f(Z_{DR}) = 0.4 + 5.0 |10^{0.1Z_{DR}} - 1|^{1.3}, \quad (2b)$$

and  $Z_{DRb} = Z_{DR} + \delta Z_{DR}$  is the biased differential reflectivity. It follows from (2) that the fractional error is slightly larger if the dB bias in differential reflectivity is negative. Hence the fractional biases in  $R$  are plotted (Fig. B.1) for three negative values of  $Z_{DR}$  bias.

Implications of bias can be assessed by comparing the polarimetric estimates of  $R$  with that obtain using a commonly accepted  $R(Z)$  relation. For such a stand-alone relation (i.e., no adjustment with gage data) the rms errors are about 35 % (Brandes et al. 2002, Balakrishnan et al. 1989, Ryzhkov and Zrnicek 1995). But, with judicious use of polarimetric data,  $R$  errors could be reduced to between 15 and 22 % (Zhang et al. 2001; Ryzhkov et al. 2005b; Matrosov et al. 2002). Thus it is reasonable to strive to keep

$\Delta R / R$  less than about 20 % implying that the absolute bias in differential reflectivity should be less than 0.15 dB.

As  $Z_{DR}$  increases, it takes larger  $\delta Z_{DR}$  to produce the same fractional bias in rain rate. This important fact suggests that at larger  $Z_{DR}$  a larger  $\delta Z_{DR}$  could be tolerated. Generally two independent mechanisms produce  $Z_{DR}$  bias. One is a small but constant offset due to calibration error (this can be kept within  $\pm 0.1$  dB; Zrnic et al. 2006), the other is the presence of cross-polar radiation. Bias,  $\delta Z_{DR}$ , depends (as demonstrated later) on  $Z_{DR}$ , the transmitted differential phase  $\beta$ , the phase difference between copolar and cross-polar patterns, and the total differential phase  $\Phi_{DP}$  along the propagation paths.

#### **B.4. Coupling through the radiation patterns**

##### *a. An expression for the bias*

Consider a circularly symmetric antenna (parabolic dish) and uniform distribution of scatterers. Performance characteristics of such antennas for dual polarization radars are discussed by Bringi and Chandrasekar (2001, section 6.2). These authors provide error budget and integral formulas for biases applicable to the AHV mode. With similar simplification, but extending the analysis to cross-polar patterns that are different than the copolar pattern, we formulate equations for the  $Z_{DR}$  bias incurred with the SHV and AHV modes.

The effects on  $Z_{DR}$  will be quantified under the following conditions. The intrinsic  $Z_{DR}$  is produced by oblate scatterers having zero canting angles so that the off-diagonal terms of the backscattering matrix are zero. The amplitudes of the electric fields in the H and V

channels are assumed to be matched, but there is a differential phase  $\beta$  between the two at the feed horn aperture. Differential attenuation along the path of propagation can, for most observations at 10 cm wavelengths, be neglected, but  $\Phi_{DP}$  cannot be ignored. To simplify notation,  $\Phi_{DP}$  is incorporated into the backscattering matrix  $\mathbf{S}$  observed at the radar (i.e.,  $\Phi_{DP}$  is merged with the scatterer's backscatter differential phase). Furthermore, it is not necessary to include the resolution volume depth; thus the function  $F$  (Doviak and Zrnicek, 2006; section 8.5.2.2), weighting the polarimetric properties of a scatterer, is only proportional to the intensity and phase of the radiation pattern at angles  $\theta, \varphi$ .

With these conditions we write the matrix equation

$$\begin{bmatrix} \delta V_h \\ \delta V_v \end{bmatrix} \equiv \vec{V} = \mathbf{F}' \mathbf{S} \mathbf{F} \vec{E}_i = \begin{bmatrix} F_{hh} & F_{vh} \\ F_{hv} & F_{vv} \end{bmatrix} \begin{bmatrix} s_{hh} & 0 \\ 0 & s_{vv} \end{bmatrix} \begin{bmatrix} F_{hh} & F_{hv} \\ F_{vh} & F_{vv} \end{bmatrix} \begin{bmatrix} 1 \\ e^{j\beta} \end{bmatrix} \quad (3)$$

for the received H and V channel incremental voltages generated by the scatterer. (In case of the AHV we would write  $\delta V_h = \delta V_{hi}$ , and  $\delta V_v = \delta V_{vi}$  where 'i' is either h or v, the first index identifying the H or V channel receiving the signal, and the second index identifying the transmitting channel, and the  $\vec{E}_i$  vector's polarization would alternate between H and V every PRT). The superscript "t" denotes the transpose matrix,  $\vec{E}_i$  is the transmitted electric field in the feed horn aperture.  $F_{hv}$  is proportional to the H radiated electric field if the V channel is excited, and vice versa for  $F_{vh}$ . Constants of proportionality, that would make this equation dimensionally correct, and the arguments of  $F_{ij}$  and  $s_{ij}$ , are omitted to shorten the notation; these omissions have no effect

whatsoever on our results. The copolar pattern functions  $F_{ii}$  are not normalized but contain the peak power gain  $g_{ii}$  so that

$$F_{ij}(\theta, \phi) = \sqrt{g_{ij}} f_{ij}(\theta, \phi). \quad (4)$$

The spherical angles  $(\theta, \phi)$  are relative to the copolar beam axis.

It is further stipulated that  $F_{hh} = F_{vv}$  is a real function (i.e., has zero reference phase), but  $F_{hv}$ ,  $F_{vh}$  are complex. Wang and Chandrasekar (2006) also consider the phase differences  $\gamma_{vh}$  and  $\gamma_{hv}$  between copolar and cross-polar patterns. The effect of the phase difference due to the receiver is neglected as it has no bearing on the results reported herein.

Executing the matrix multiplication in (3) the following equation ensues

$$\begin{vmatrix} \delta V_h \\ \delta V_v \end{vmatrix} = \begin{vmatrix} s_{hh} F_{hh} (F_{hh} + F_{hv} e^{j\beta}) + s_{vv} F_{vh} (F_{vh} + F_{hh} e^{j\beta}) \\ s_{hh} F_{hv} (F_{hh} + F_{hv} e^{j\beta}) + s_{vv} F_{hh} (F_{vh} + F_{hh} e^{j\beta}) \end{vmatrix}. \quad (5)$$

Of interest are the powers from the ensemble of scatterers weighted by pattern functions. Thus we will take the ensemble average and integrate it over the pattern functions to obtain the power received in the H channel

$$P_h \sim \iint_{\theta, \phi} \langle |\delta V_h|^2 \rangle \sin \theta d\theta d\phi = \int_{\Omega} \langle |s_{hh} F_{hh} (F_{hh} + F_{hv} e^{j\beta}) + s_{vv} F_{vh} (F_{vh} + F_{hh} e^{j\beta})|^2 \rangle d\Omega, \quad (6)$$

where  $\langle \rangle$  indicates ensemble average over the distribution of the scatterers' properties (Doviak and Zrnic 2006; Eq.8.45). To shorten notation, the integral over  $\theta$  and  $\phi$  is replaced with the integral over the solid angle  $\Omega$ . A very similar expression for  $P_v$  follows from the second row of (5).

The integral in (6) can be expressed as the sum of three terms of which the first (containing  $s_{hh}$ ) is

$$\int_{\Omega} \langle |s_{hh} F_{hh} (F_{hh} + F_{hv} e^{j\beta})|^2 \rangle d\Omega = \langle |s_{hh}|^2 \rangle \int_{\Omega} F_{hh}^2 [F_{hh}^2 + 2F_{hh} \operatorname{Re}(F_{hv} e^{j\beta}) + |F_{hv}|^2] d\Omega, \quad (7a)$$

wherein it is assumed that the ensemble averages of the backscattering second moments (e.g.,  $\langle |s_{hh}|^2 \rangle$ ) are constant in regions where the pattern functions are significant.

The second term is the cross product involving  $s_{hh}$  and  $s_{vv}$  (i.e., it is twice the real part of the first term in (6) multiplied with the conjugate of the second term),

$$2 \int_{\Omega} \operatorname{Re} \left[ \langle s_{hh} s_{vv}^* \rangle (F_{hh}^2 F_{vh}^{*2} + F_{hh} F_{hv} F_{vh}^{*2} e^{j\beta} + F_{hh}^3 F_{vh}^* e^{-j\beta} + F_{hh}^2 F_{hv} F_{vh}^*) \right] d\Omega, \quad (7b)$$

and the third term, the magnitude squared of the second term in (6), is

$$\int_{\Omega} \langle |s_{vv} F_{vh} (F_{vh} + F_{hh} e^{j\beta})|^2 \rangle d\Omega = \langle |s_{vv}|^2 \rangle \int_{\Omega} |F_{vh}|^2 [ |F_{vh}|^2 + 2F_{hh} \operatorname{Re}(F_{vh} e^{-j\beta}) + F_{hh}^2 ] d\Omega. \quad (7c)$$

Next are listed the corresponding three terms comprising the power of vertically polarized return:

$$\langle |s_{hh}|^2 \rangle \int_{\Omega} |F_{hv}|^2 [F_{hh}^2 + 2F_{hh} \operatorname{Re}(F_{hv} e^{j\beta}) + |F_{hv}|^2] d\Omega, \quad (8a)$$

$$2 \int_{\Omega} \operatorname{Re} \left[ \langle s_{hh} s_{vv}^* \rangle (F_{hv}^2 F_{hh}^2 + F_{hh} F_{vh}^* F_{hv}^2 e^{j\beta} + F_{hv} F_{hh}^3 e^{-j\beta} + F_{hh}^2 F_{hv} F_{vh}^*) \right] d\Omega, \quad (8b)$$

and

$$\langle |s_{vv}|^2 \rangle = \int_{\Omega} F_{hh}^2 \left[ |F_{vh}|^2 + 2F_{hh} \operatorname{Re}(F_{vh} e^{-j\beta}) + F_{hh}^2 \right] d\Omega. \quad (8c)$$

The bias  $\delta Z_{DR}$  expressed in dB is computed from

$$\delta Z_{DR} = 10 \log(P_h / P_v) - Z_{DR}, \quad (9)$$

for specific values of the system parameters and polarimetric variables. In the sequel differential reflectivity in linear units will also be used; that is

$$Z_{dr} = \frac{\langle |s_{hh}|^2 \rangle}{\langle |s_{vv}|^2 \rangle}, \quad (10a)$$

as well as the copolar correlation coefficient

$$\rho_{hv} e^{j\Phi_{DP}} = \frac{\langle s_{hh}^* s_{vv} \rangle}{\sqrt{\langle |s_{hh}|^2 \rangle \langle |s_{vv}|^2 \rangle}}. \quad (10b)$$

The expressions for computing bias are applicable to arbitrary copolar and cross-polar patterns. To illustrate and gain some insight on the importance of various terms in (7) and (8), herein we consider parabolic antennas. These antennas are designed to have very low cross-polar radiation. Therefore within the main beam  $F_{hh} \gg |F_{hv}|$  and  $F_{hh} \gg |F_{vh}|$ . With this in mind one can drop the third and fourth order terms in (7) and (8), sum the remaining terms, and divide the powers  $P_h$  and  $P_v$  with  $\langle |s_{vv}|^2 \rangle$  to obtain

$$\frac{P_h}{\langle |s_{vv}|^2 \rangle} = Z_{dr} \int_{\Omega} \left\{ F_{hh}^2 \left[ F_{hh}^2 + 2F_{hh} \operatorname{Re}(F_{hv} e^{j\beta}) + |F_{hv}|^2 \right] + \right. \\ \left. 2\rho_{hv} Z_{dr}^{-1/2} F_{hh}^2 \operatorname{Re} \left[ e^{-j\Phi_{DP}} (F_{vh}^{*2} + F_{hh} F_{vh}^* e^{-j\beta} + F_{hv} F_{vh}^*) \right] + Z_{dr}^{-1} F_{hh}^2 |F_{vh}|^2 \right\} d\Omega, \quad (11a)$$

and

$$\frac{P_v}{\langle |s_{vv}|^2 \rangle} = \int_{\Omega} \left\{ \frac{2\rho_{hv} Z_{dr}^{1/2} F_{hh}^2 \operatorname{Re} \left[ e^{-j\Phi_{DP}} (F_{hv}^2 + F_{hh} F_{hv} e^{-j\beta} + F_{hv} F_{vh}^*) \right] +}{Z_{dr} F_{hh}^2 |F_{hv}|^2 + F_{hh}^2 \left[ |F_{vh}|^2 + 2F_{hh} \operatorname{Re}(F_{vh} e^{-j\beta}) + F_{hh}^2 \right]} \right\} d\Omega. \quad (11b)$$

The biased differential reflectivity (dB) is the difference in the logarithms of (11a) and (11b). Note  $\int_{\Omega} F_{hh}^4 d\Omega$  is much larger than any of the other terms in (11a and b). Dividing these two equations with this term and taking the difference of logarithmic functions produces the bias. Because the arguments of the logarithmic functions are close to 1, we use the first order Taylor expansion and express the bias as

$$\delta Z_{DR} = 10(A_1 + A_2) \log e \quad (12a)$$

where the term  $A_1$  contains integrals of  $F_{hv}$  to first order and  $A_2$  contains the integrals of  $F_{hv}$  to second order. Explicitly

$$A_1 = \frac{2 \int F_{hh}^3 \operatorname{Re} \{ F_{hv} e^{j\beta} - F_{vh} e^{-j\beta} + \rho_{hv} [e^{-j\Phi_{DP}} (Z_{dr}^{-1/2} F_{vh}^* e^{-j\beta} - Z_{dr}^{1/2} F_{hv} e^{-j\beta})] \} d\Omega}{\int F_{hh}^4 d\Omega}, \quad (12b)$$

$$A_2 = \frac{\int F_{hh}^2 \left\{ |F_{hv}|^2 - |F_{vh}|^2 + Z_{dr}^{-1} |F_{vh}|^2 - Z_{dr} |F_{hv}|^2 + 2\rho_{hv} \operatorname{Re} \{ e^{-j\Phi_{DP}} [Z_{dr}^{-1/2} (F_{vh}^{*2} + F_{hv} F_{vh}^*) - Z_{dr}^{1/2} (F_{hv}^2 + F_{hv} F_{vh}^*)] \} \right\} d\Omega}{\int_{\Omega} F_{hh}^4 d\Omega}. \quad (12c)$$

*b. Types of cross-polar radiation patterns*

In the literature one finds cross-polar pattern types to which the expressions developed herein are applicable. One type has a prominent cross-polar peak collocated with the peak of the copolar pattern. This pattern is discussed in the next section. A second type has a quad of cross-polar peaks located diagonally to the H and E principal planes; this is typical of a center feed parabolic reflector (Fradin 1961). For parabolic reflectors with offset feeds, the number of cross-polar peaks is reduced to two (Durić et al. 2008). Finally there are cross-polar patterns that appear to be a combination of the first two types. Contours of the main lobes for these pattern types are sketched in Fig. B.2. The large circles represent cross sections of the copolar main lobes well below the peak (say 30 dB), whereas the small circles are the cross sections of the cross-polar lobes at the same relative level with respect to the main lobe peak.

Prior to quantifying the bias, a brief discussion of radiation patterns follows starting with the one measured for the KOUN radar. This pattern type (i.e., Fig. B.2a) is examined for obvious practical reasons, which are to quantify its effects on the KOUN polarimetric radar and to anticipate the performance of the forthcoming dual-polarization WSR-88D radars. Measurements of the H cross-polar radiation field indicate a cross-polar pattern with a peak about 30 dB below the V copolar peak, centered on the copolar beam axis. The principal contributor to this peak is thought to be the cross-polar pattern of the feed horn illuminating the reflector (Doviak and Zrnic 1998).

We have also examined cross-polar patterns measured by Andrew Canada (Paramax 1992) on another WSR-88D reflector illuminated with a feed that generates a single

linear polarized field (i.e., horizontal). The measurement shows a cross-polar main lobe coaxial with the copolar lobe, and the ratio of the cross-polar peak to copolar peak is about the same as that measured for the KOUN.

The cause of cross-polar peaks along the beam axis of the feed has not been established, but it is known that concentricity and circularity of the horn components on the order of a few thousandths of a wavelength are necessary to substantially reduce spurious emissions (Potter 1963). On the other hand, cross-polar patterns for the WSR-88D reflector at a wavelength of 5 cm have a pronounced minimum along the copolar beam axis (section 3.d.1). Measurements of the weak cross-polar radiation on ad-hoc outdoor antenna ranges are more likely to have problems, and it is possible that the cross-polar radiation along the copolar beam axis is an artifact of the antenna range.

Although there can be many causes of cross-polar peak radiation, we shall focus our formulation on three specific ones, and for each of these we shall specify the amplitude and phase of  $F_{hv}$  and  $F_{vh}$ . Cross-polar radiation (i.e., H radiation fields if the V antenna port is excited and vice versa) can be generated by: 1) a rotation of the horn about its axis (Doviak and Zrnic 1998), 2) a lack of geometric orthogonality of the H and V ports, and 3) the parabolic reflector (Fradin 1961). There might be other causes, and for comparisons we also examine the worst possible case. Next we develop expressions for  $Z_{DR}$  bias in case of coincident copolar and cross-polar pattern peaks.

*c.  $Z_{DR}$  bias due to coincident copolar and cross-polar pattern peaks*

The first order terms in  $A_1$  (12b) are much larger than the second order terms in  $A_2$  (12c) hence  $A_2$  can be ignored so that the bias (12a) can be written as

$$\delta Z_{\text{DR}} = 20 \log(e) \left\{ \begin{aligned} &W_{\text{hv}} \left[ \cos(\beta + \gamma_{\text{hv}}) - \rho_{\text{hv}} Z_{\text{dr}}^{1/2} \cos(\Phi_{\text{DP}} + \beta - \gamma_{\text{hv}}) \right] \\ &- W_{\text{vh}} \left[ \cos(\beta - \gamma_{\text{vh}}) - \rho_{\text{hv}} Z_{\text{dr}}^{-1/2} \cos(\Phi_{\text{DP}} + \beta + \gamma_{\text{vh}}) \right] \end{aligned} \right\} \quad (13)$$

where  $\gamma_{\text{hv}}$  and  $\gamma_{\text{vh}}$  are the phases of the cross-polar radiation relative to the copolar phase,

$$W_{\text{hv}} = \int F_{\text{hh}}^3 |F_{\text{hv}}| d\Omega / \int F_{\text{hh}}^4 d\Omega \quad (14a)$$

and

$$W_{\text{vh}} = \int F_{\text{hh}}^3 |F_{\text{vh}}| d\Omega / \int F_{\text{hh}}^4 d\Omega \quad (14b)$$

are the antenna's bias weighting factors that measure the effectiveness of the cross-polar field in generating  $Z_{\text{DR}}$  biases. For antenna designs these weighting factors can be conservatively specified so that the bias is always smaller than a prescribed value. This conservative specification can be relaxed, as demonstrated next, if the various phases are appropriately adjusted.

Let's first consider the case  $F_{\text{hv}}=F_{\text{vh}}$ . Thus, defining  $W_{\text{hv}}=W_{\text{vh}}=W$  and  $\gamma_{\text{hv}} = \gamma_{\text{vh}} = \gamma$  and substituting these into (13) produces

$$\delta Z_{\text{DR}} \approx 20 \log(e) W \left\{ \begin{aligned} &-2 \sin(\beta) \sin(\gamma) + \\ &\rho_{\text{hv}} \left[ Z_{\text{dr}}^{-1/2} \cos(\Phi_{\text{DP}} + \beta + \gamma) - Z_{\text{dr}}^{1/2} \cos(\Phi_{\text{DP}} + \beta - \gamma) \right] \end{aligned} \right\} \text{ (dB)}. \quad (15)$$

This equation indicates that the maximum bounds on  $\delta Z_{\text{DR}}$  are

$$\delta Z_{\text{DR}} \approx \pm 20 \log(e) W \left\{ 2 + \rho_{\text{hv}} \left[ Z_{\text{dr}}^{-1/2} + Z_{\text{dr}}^{1/2} \right] \right\}. \quad (16a)$$

These bounds occur if  $\beta = \pm 90^\circ$  and  $\gamma = \mp 90^\circ$  (i.e., bias is always positive but variable depending on  $\Phi_{DP}$ ) or  $\gamma = \pm 90^\circ$  (i.e., bias is always negative). Thus depending on the particular values of the phases ( $\beta$ ,  $\gamma$ , and  $\Phi_{DP}$ ) the bias can take any value between the boundaries given by (16a). Because for rain  $\left[ Z_{dr}^{-1/2} + Z_{dr}^{1/2} \right] \approx 2$ , and  $\rho_{hv} \approx 1$ , the largest positive or negative bias is

$$\delta Z_{DR} \approx \pm 80W \log(e) = \pm 35W \text{ (dB)}. \quad (16b)$$

These large biases can be incurred if the transmitted wave is circularly polarized, and the cross-polar and copolar pattern peaks are in phase quadrature.

From (15) it can be deduced that the narrowest span of bias occurs if  $\beta = 0^\circ$  or  $180^\circ$ , and  $\gamma = 180^\circ$  or  $0^\circ$ . Then the bias is contained within the bounds

$$\delta Z_{DR} \approx \pm 20W \log(e) \rho_{hv} (Z_{dr}^{1/2} - Z_{dr}^{-1/2}) \quad (16c)$$

To achieve this narrow span of bias, the transmitted field should be slanted linear at either  $\pm 45^\circ$  while the cross-polar voltage pattern (within the main lobe) should be in or out of phase with respect to the phase of the copolar pattern. Control of the transmitted phase  $\beta$  is practical, but imposition of a phase difference between cross-polar and copolar main lobes might be difficult to achieve.

Suppose that the phase difference  $\beta$  is set to  $0^\circ$  or  $180^\circ$  (by design), but the cross-polar field is in phase quadrature with the copolar field (i.e.,  $\gamma = \pm 90^\circ$ ). Under these conditions,  $\delta Z_{DR}$  is now contained within the intermediate bounds

$$\delta Z_{DR} \approx \pm 20W \log(e) \rho_{hv} (Z_{dr}^{-1/2} + Z_{dr}^{1/2}) \approx \pm 17.4W . \quad (16d)$$

These three bias boundaries (i.e., 16a, 16c, and 16d), with  $\delta Z_{DR}$  bias normalized by  $W$  versus  $Z_{DR}$ , are plotted in Fig. B.3.

In summary, Fig. B.3 indicates that the largest span of bias (top curve) is incurred if  $\beta = \pm 90^\circ$  (i.e., circularly polarized transmitted field) and  $\gamma = 90^\circ$ . Change in any one of these would therefore reduce the bias below the curve. With  $\beta$  adjusted to minimize the bias (e.g.,  $\beta = 0^\circ$ ) the worst case of positive bias is the middle curve (16d). This curve and the highest curve are essentially independent of  $Z_{DR}$ . For the case  $\beta = 0^\circ$  and  $\gamma = 180^\circ$  the maximum positive bias is the lowest curve (its mirror image about the abscissa represents the maximum negative bias). In the region of  $Z_{DR}$  typical for rain these curves are linear.

We shall use Fig. B.3 to determine the bias for some possible values of the antenna gains. Assume axially symmetric Gaussian radiation patterns (4) so that  $|f_{ij}(\theta)|^2 = \exp[-\theta^2 / (4\sigma_{ij}^2)]$  describes the one-way power pattern (Doviak and Zrnich 2006; section 5.3). Then

$$W_{hv} = \frac{4\theta_{1x}^2}{\theta_1^2 + 3\theta_{1x}^2} \cdot \frac{g_{hv}^{1/2}}{g_{hh}^{1/2}} \quad \text{and} \quad W_{vh} = \frac{4\theta_{1x}^2}{\theta_1^2 + 3\theta_{1x}^2} \cdot \frac{g_{vh}^{1/2}}{g_{hh}^{1/2}}, \quad (17a,b)$$

where the one-way 3 dB beamwidths of the copolar and cross-polar power patterns are  $\theta_1$  and  $\theta_{1x}$ . For equal beamwidths and if the peak of the cross polar pattern is 40 dB below the copolar peak,  $W = 0.01$ . From Fig. B.3 we find that the worst bias is about 0.35 dB. This bias would drop to about 0.18 dB if the transmitted H and V field at the antenna aperture are in phase; this would produce a rain rate error of less than 25% (Fig. B.1).

Further reduction is possible only if the copolar and cross-polar patterns are in phase (or 180° out of phase).

#### 1) $Z_{DR}$ BIAS DUE TO A ROTATED HORN

It will be assumed that rotation of the horn in the polarization plane is the only mechanism causing cross-coupling. That is, the cross-polar radiation with a properly oriented horn is negligible (i.e., the intrinsic  $F_{hv} = F_{vh} = 0$ ). Computing the bias in this case can be done by introducing the rotation matrix in equation (3). Multiplying the rotation matrix with the F matrix we obtain the effective matrix  $\mathbf{F}^{(e)}$

$$\mathbf{F}^{(e)} = \begin{vmatrix} F_{hh} \cos \alpha & -F_{hh} \sin \alpha \\ F_{hh} \sin \alpha & F_{hh} \cos \alpha \end{vmatrix}, \quad (18)$$

where  $\alpha$  is the rotation angle with a positive sign counter-clockwise. In this case

$F_{hv}^{(e)} = -F_{hh} \sin \alpha$ ,  $F_{vh}^{(e)} = F_{hh} \sin \alpha$ , etc. Then introducing the terms from (18) into (13) and carrying forward the computations, the following approximate formula for the bias is obtained:

$$\delta Z_{DR} \approx 20W \log(e) \left[ -2 \cos(\beta) + \rho_{hv} (Z_{dr}^{-1/2} + Z_{dr}^{1/2}) \cos(\Phi_{DP} + \beta) \right], \quad (19)$$

where now the bias weighting factor  $W = \tan(\alpha)$ . For small angular rotations, this result agrees with that obtained by Doviak et al. (2000).

Feed horn rotation can be set to tolerances of the order of 0.1° (Doviak and Zrnic 1998, section II.6.7) at which  $\tan(0.1^\circ) = 0.0017$ , and the maximum bias (top graph in Fig. B.3)

is about 0.06 dB. Hence we conclude that on well designed antennas, horn rotation should not be a factor.

## 2) BIAS DUE TO NONORTHOGONALITY OF THE H AND V PORTS

Let's assume that the H, V ports are separated by an angle  $\chi < \pi / 2$  and the horn is rotated about its axis to null one of the cross-polar fields. For example, if the cross-polar V field produced by excitation of the H port had an on-axis null (i.e.,  $F_{vh} = 0$ ), the copolar V field would be  $F_{hh}$ . But if the V port is then excited, the cross-polar H would be  $-F_{hh} \sin \alpha$ , where  $\alpha = (\pi / 2) - \chi$  ( $\alpha$  positive counter-clockwise), and the copolar V would be  $F_{hh} \cos \alpha$ . Thus the matrix  $\mathbf{F}^{(e)}$  becomes

$$\mathbf{F}^{(e)} = \begin{vmatrix} F_{hh} & -F_{hh} \sin \alpha \\ 0 & F_{hh} \cos \alpha \end{vmatrix}, \quad (20)$$

and by substituting the terms from (20) into (13) and simplifying, the following bias equation is obtained,

$$\delta Z_{DR} \approx 20W_1 \log(e) \left[ -\cos(\beta) + \rho_{hv} Z_{dr}^{1/2} \cos(\Phi_{DP} + \beta) \right]. \quad (21)$$

In (21)  $W_1 = \sin \alpha$  and, as with (19), the bias peaks at  $\beta = -90^\circ$  and  $\Phi_{DP} = 90^\circ$ . At the same  $\alpha$  tolerance as that for the rotated horn, bias is insignificant.

### *d. $Z_{DR}$ bias due to a four-lobed cross-polar radiation pattern*

Cross-polar radiation patterns with nulls along the principal planes and a distinct equal amplitude principal peak near the copolar peak in each of the quadrants (Fig. B.3b) is the

subject of this section. This type pattern is inherent to a center-fed parabolic reflector illuminated with linearly polarized radiation (Fradin 1961, section VII.2). For an example the reader is referred to Chandrasekar and Keeler (1993, Fig. 11). Offset parabolic reflectors (e.g., the SPIRA polarimetric imaging radiometer, Durić et al. 2008) produce cross-polar patterns with two principal peaks near the copolar peak. These cross-polarized peaks, inherent to the parabolic reflector, can be substantially reduced if a circular horn is used to illuminate the reflector (Fradin 1961, VII.3). The general procedure used in section 3a to compute  $Z_{DR}$  biases also applies to this case. Nonetheless, to obtain analytical solutions, further simplification and assumptions are required.

The magnitude of the electric field pattern  $f_{hv}(\theta, \phi)$  is roughly axially symmetric about its peak, but the electric field at each peak alternates in sign as one passes from one peak to the next around the beam axis of the copolar pattern. Furthermore, it can be shown (Appendix) that the copolar and cross-polar fields are in phase (or anti-phase), and that  $|F_{hv}| = |F_{vh}|$ . Therefore (in case of perfect axial symmetry), the terms  $F_{hh}^k F_{hv}^n$  in (7) integrate to zero for any  $k$  if the exponent  $n$  is odd and if there is an even number of peaks; that is, the first order and third order terms in  $F_{hv}$  vanish, hence  $A_1=0$ . This will be assumed herein so that  $A_2$  (12c) produces the bias

$$\delta Z_{DR} = 10 \log(e) \left[ Z_{dr}^{-1} - Z_{dr} + 4 \rho_{hv} (Z_{dr}^{-1/2} - Z_{dr}^{1/2}) \cos(\Phi_{DP}) \right] \frac{\int F_{hh}^2 |F_{hv}|^2 d\Omega}{\int F_{hh}^4 d\Omega}. \quad (22)$$

Let's apply (22) to a cross-polar pattern having 4 peaks. Assume a Gaussian shape for the copolar lobe and the following offset Gaussian shape:

$$|F_{hv}(\theta, \phi)|^2 = g_{hv} |f_{hv}(\theta, \phi)|^2 = g_{hv} \exp \left[ -\frac{(\theta - \theta_p)^2 + (\phi - \phi_p)^2}{4\sigma_{hv}^2} \right],$$

for each of the cross-polar lobes. Here  $\theta_p$  and  $\phi_p$  are angular displacements of the cross-polar radiation peaks from the copolar beam axis. Then define

$$W_4 = \frac{\int F_{hh}^2 |F_{hv}|^2 d\Omega}{\int F_{hh}^4 d\Omega} = 4 \frac{2g_{hv}\theta_{1x}^2}{g_{hh}(\theta_{1x}^2 + \theta_1^2)} e^{-\frac{4\theta_p^2 \ln(2)}{(\theta_1^2 + \theta_{1x}^2)}}, \quad (23)$$

as the antenna's bias weighting factor for a 4-lobed cross-polar radiation pattern. The cross-polar lobes are displaced from the main beam axis by  $\theta_p$ , and the 3 dB width of the one-way copolar power pattern is  $\theta_1$ , whereas the 3 dB one-way width of each cross-polar lobe is  $\theta_{1x}$ . Fradin's equations (Appendix) are used to compute the location of the cross-polar peaks for a center-fed parabolic reflector. In the case of a WSR-88D reflector the cross-polar pattern peaks should be about  $1^\circ$  away from the copolar beam axis. Because of the strong on-axis cross-polar lobe, it was difficult to discern the cross-polar peaks due to the KOUN reflector. But for a reflector having the same specifications (section 3.d.1), measurements (i.e., about  $0.5^\circ$ ; Fig. B.5) at a wavelength of 5 cm indicate good agreement with  $\theta_p$  calculated (i.e.,  $0.47^\circ$ ).

For rain  $Z_{dr} > 1$ , and from (22) it is deduced the largest bias is negative if  $\Phi_{DP} = 0^\circ$ . Under this condition (i.e.,  $\Phi_{DP} = 0^\circ$ ) and for  $\rho_{hv} = 1$ ,  $\delta Z_{DR}$  normalized with  $W_4$  is plotted in Fig. B.4. Note that the maximum bias grows almost linearly with differential reflectivity (i.e.,  $\delta Z_{DR} / W_4 \approx -6.15 Z_{DR}$ ) in the range of 0 to 3 dB. Let's now examine a specific polarimetric weather radar example.

Measurements of the cross-polar beam width (section 3.d.1) indicate it is about the same as the copolar beam width (i.e.,  $0.5^\circ$  on the University of Oklahoma polarimetric radar called OU PRIME and  $1^\circ$  on the KOUN), and  $\theta_p \approx \theta_1$ . Assume the ratio of gains ( $g_{hv}/g_{hh}$ ) = 0.001 (-30 dB which is an upper value). Then  $W_4$  in (23) equals  $g_{hv}/g_{hh}$  and the worst negative bias is about  $-0.0062 Z_{DR}$  (dB).

The primary reason for the significantly better performance of this type of cross-polar radiation pattern is that the four symmetrically located pattern peaks alternate sign so that there is cancellation of some cross-polar contribution. Another reason is the bias weighting factor is proportional to the integral of the square of the normalized cross-polar radiation, whereas it is proportional to the normalized radiation if the cross-polar pattern is coaxial with the copolar pattern. Furthermore, the displacement of these peaks from the copolar beam axis causes the cross product of copolar pattern with the cross-polar pattern to be smaller than in case where the peaks are coincident.

#### 1) AN EXAMPLE

In Fig. B.5 are two cross-polar patterns measured OU PRIME radar. This antenna reflector is a replica of the WSR-88D reflector, but has four feed-support struts as opposed to three, and is illuminated with 5 cm wavelength radiation. Thus the beam width is  $0.5^\circ$ , i.e., half the beamwidth of the WSR-88D radar.

This type of cross polar radiation pattern can be represented as sum of a centered pattern (Fig. B.2a) with the quad pattern (Fig. B.2b). The exact computation of the bias is

straight-forward, although tedious. Significant simplification is possible by noting that the dominant terms are the cross products  $\int F_{hh}^3 |F_{hv}| d\Omega$  and  $\int F_{hh}^2 |F_{vh}|^2 d\Omega$ .

The two-way copolar power pattern and the two normalized cross products (i.e.,  $F_{hh}^3 |F_{hv}|$  and  $F_{hh}^2 |F_{vh}|^2$ ) in the three principal planes are in Fig. B.6a, B.6b, B.6c. It is clear from Fig. B.6 that the cross-polar pattern peak collocated with copolar beam axis contributes most to the bias. Because the normalized term  $F_{hh}^3 |F_{vh}| / F_{hh}^4(0)$  has almost the same angular width as  $F_{hh}^4$ , the antenna's bias weighting factor,  $W_{vh}$  (14b) can be approximated with  $\sqrt{g_{vh} / g_{hh}}$  (0.01 in this case). Furthermore if  $|F_{hv}| = |F_{vh}|$ ,  $W_{hv} = W_{vh} = W = 0.01$ . With this value the worst possible bias (if the phase of cross polar pattern is  $90^\circ$  and differential phase on transmission is  $-90^\circ$ ) can be read from the top curve in Fig. B.3. It is about 0.35 dB. This is significant but unlikely to happen as it requires a juxtaposition of  $\gamma = 90^\circ$ ,  $\beta = -90$ , and  $\Phi_{DP} = 0^\circ$ .

The worst possible bias contributed by the four symmetric peaks is computed following equations (22) and (23). The ratio ( $g_{hv}/g_{hh}$ )  $\approx 3.16 \cdot 10^{-4}$  (i.e., about -35 dB from Fig. B.5), and assuming  $\theta_p = \theta_1$ , this bias is approximately  $0.002 Z_{DR}$ , which is insignificant.

### **B.5. Alternate Transmit and Simultaneous Receive (AHV) mode**

Consider next the AHV mode and apply the same formalism starting with (3). For computing  $P_h$  set the second element in the right most matrix to zero, and for  $P_v$  set the first element to zero. Then, after performing the multiplications and ignoring terms higher than first order in the cross-polar radiation, the powers can be expressed as

$$\frac{P_h}{\langle |s_{vv}|^2 \rangle} \sim Z_{dr} \int F_{hh}^4 d\Omega + 2\rho_{hv} \sqrt{Z_{dr}} \cos(\Phi_{DP} + 2\gamma_{vh}) \int F_{hh}^2 |F_{vh}^2| d\Omega ; (25a)$$

$$\frac{P_v}{\langle |s_{vv}|^2 \rangle} \sim \int F_{hh}^4 d\Omega + 2\rho_{hv} \sqrt{Z_{dr}} \cos(\Phi_{DP} - 2\gamma_{hv}) \int F_{hh}^2 |F_{hv}^2| d\Omega . (25b)$$

Thus the bias is

$$\delta Z_{DR} \approx 20 \log(e) \rho_{hv} \{W_{vh} Z_{dr}^{-1/2} \cos(\Phi_{DP} + 2\gamma_{vh}) - W_{hv} Z_{dr}^{1/2} \cos(\Phi_{DP} - 2\gamma_{hv})\} \text{ (dB)}, (26)$$

where now

$$W_{vh} = \frac{\int F_{hh}^2 |F_{vh}|^2 d\Omega}{\int F_{hh}^4 d\Omega}, \quad W_{hv} = \frac{\int F_{hh}^2 |F_{hv}|^2 d\Omega}{\int F_{hh}^4 d\Omega}. (27a, b)$$

Comparing (27a, b) with (14a, b) it is evident that, for cross-polar radiation patterns having a prominent peak on-axis with the copolar peak, the antenna's bias factors for AHV mode are significantly smaller than for SHV mode, and thus  $Z_{DR}$  bias for AHV is substantially reduced.

For a well-designed and fabricated polarimetric antenna, the cross-polar radiation should vanish along the principal planes; thus there should be a null on-axis. For example, Deguchi et al. (2008) have designed a feed horn that has a deep and broad minimum of cross-polar radiation about the axis of the copolar beam, and thus illumination of the parabolic reflector with this radiation field should produce a broad minimum of cross-polar radiation about the copolar beam axis. In this case the only prominent peaks of cross-polar radiation should be that associated with the reflector (Appendix).

Cross-polar pattern measurements on large antennas are more difficult to make and interpret than copolar patterns because cross-polar radiation is weak and the copolar radiation incident on the terrain surrounding the radar site can be converted to cross-polar radiation upon scatter (Doviak and Zrníc 1998, section II.6.3). This is worse at low elevation angles where parts of the copolar beam could illuminate the foreground. Thus the lack of a well defined on-axis null could be an artifact of the site where patterns are measured. The radiation patterns seen in Fig. B.5 suggest that the on-axis cross-polar radiation is well below the copolar peak. It is likely that the smaller beamwidth of the 5 cm OU PRIME mitigates reflection from the terrain. Note that these measurements were made at the site where the patterns of the 10 cm WSR-88D antenna were measured. Thus, let's assume that we have a center-fed antenna in which the on-axis radiation lobe is negligible. Under this condition let's compare the  $Z_{DR}$  biases using the SHV and AHV modes. Thus, assuming four equal cross-polar lobes offset from the beam axis, we use (22) and (26) for this comparison. In this case the antenna's bias factor  $W_4$  is the same for both modes, and  $\gamma_{hv} = \gamma_{vh} = 0^\circ$ . For rain it is safe to set  $\rho_{hv} \approx 1$ , and note  $Z_{dr} \geq 1$ , and thus we can write  $Z_{dr} = 1 + \Delta$ , and assume that  $\Delta < 1$ . Under these conditions it can be shown that (22) reduces to

$$\frac{\delta Z_{DR}(\text{AHV})}{W_4} = -20(Z_{dr} - 1)\log(e)[1 + 2\cos\Phi_{DP}] \quad (28a)$$

which is the normalized bias for the SHV mode, whereas for the AHV mode, (26) becomes

$$\frac{\delta Z_{DR}(\text{SHV})}{W_4} = -20(Z_{dr} - 1)\log(e)\cos\Phi_{DP}, \quad (28b)$$

an almost identical expression. Comparing these two, the SHV  $Z_{DR}$  bias is just about 3 times larger than the bias for the AHV mode. Nevertheless, assuming that  $W_4 \leq 3.16 \cdot 10^{-4}$  (i.e.,  $F_{hv}$  at least -35 dB below the copolar peak; Fig. B.5), SHV bias is approximately  $0.002 Z_{DR}$ , which is still insignificant.

## B.6. Summary

Herein we investigate the bias in the differential reflectivity measurement. The cross-polar radiation introduces a bias that depends on several parameters including differential reflectivity itself. For accurate rainfall measurement this bias should be smaller than about 10% of  $Z_{DR}$  (in dB, Fig. B.1).

With this in mind we set out to quantify the bias caused by cross-polar radiation. We examine two types of cross-polar patterns commonly observed. One has a cross-polar main lobe centered on the copolar main lobe, the other has four lobes of equal magnitude and displaced symmetrically about the beam axis. Use of customary approximations (i.e., radiation lobes having Gaussian shape) and uniform distribution of horizontally oriented scatterers leads to simple analytic equations expressing the antenna's bias weighting factors (i.e., normalized products of copolar and cross-polar radiation patterns,  $W_{hv}$  and  $W_{vh}$ ).

Antennas having cross-polar nulls along the principal planes, but multiple lobes associated with the reflector, cause significantly less bias than those having a single cross-polar lobe centered on the copolar beam axis. This latter situation appears to be an artifact that causes unacceptable bias if the transmitted wave is circularly polarized and

the copolar and cross-polar voltage patterns are  $90^\circ$  out of phase; this bias can be reduced by about a factor of two (on a dB scale) if the transmitted wave is slant linear at  $\pm 45^\circ$ . If these coaxial lobes have the same widths, the level of cross polar radiation must be at least 45 dB below the copolar lobe maximum to keep the bias under 0.1 dB. This stringent condition can be relaxed to 32 dB provided that the transmitted wave is slant linear, the copolar and cross-polar voltage patterns are in or out of phase with each other, and  $Z_{DR} \leq 2$  dB (Fig. B.3). Data (Fig. B.6) and measurements on the polarimetric prototype WSR-88D antenna indicate on-axis cross-polar gain can be 40 dB below the copolar gain.

It is suggested that the on-axis cross-polar radiation observed for large antennas is likely due to reflection from surrounding terrain, and not an inherent characteristic of the antenna. If the cross-polar radiation has an on-axis null, the only significant cross-polar radiation peaks are the four equal-gain lobes due to the reflector (section 3d); the gain of these lobes needs to be below -21 dB to insure that  $Z_{DR}$  bias is less than 0.1 dB (at  $Z_{DR} \leq 2$  dB). In practice this liberal condition would need a 5 to 10 dB downward adjustment to account for depolarization due to imperfections of the antenna. Measurements (Fig. B.5) suggest these gains are well below -30 dB.

In agreement with previous investigations, it turns out that  $Z_{DR}$  bias is not an issue for polarimetric radars utilizing the alternate (AHV) mode. For the simultaneous (SHV) mode, bias in  $Z_{DR}$  is larger, but it can be controlled with appropriate antenna design (i.e., minimizing the on-axis cross-polar radiation) so that its effect on rain rate errors is negligible (section B.5).

## *Acknowledgments*

Pattern measurements of the OU PRIME antenna were provided by Enterprise Electronics Corporation and Dr. Boon Leng Cheong of the Atmospheric Radar Research Center at the University of Oklahoma. Funding for CIMMS authors came from NOAA/Office of Oceanic and Atmospheric Research under NOAA-University of Oklahoma Cooperative Agreement NA17RJ1227, U.S. Department of Commerce.

### **B.7. Appendix: Cross-polar radiation induced by the parabolic reflector**

Fradin (1961, Section 7.2) shows that the copolar and cross-polar fields in an aperture of a center-fed parabolic reflector illuminated with the field of a vertical (i.e.,  $y$  directed) dipole are given by

$$E_y = -A \frac{4f^2 + \rho^2 \cos 2\varphi}{(4f^2 + \rho^2)^2}, \quad (\text{B.7.1})$$

and

$$E_x = -A \frac{\rho^2 \sin 2\varphi}{(4f^2 + \rho^2)^2}, \quad (\text{B.7.2})$$

where the horizontal  $x$  direction is also in the aperture,  $f$  is the focal length of the parabolic reflector (for the WSR-88D,  $f = 0.375 D$ ;  $D$  is the antenna diameter),  $A$  is a complex constant (dependent on  $f$ ,  $D$ , the dipole moment, and wavelength),  $\rho$  is the radial distance from the  $z$  axis to any point in the aperture plane, and  $\varphi$  is the angle measured from the  $x$  axis.

Using these equations, it is easily seen that the cross-polar field has nulls along the principal axes (i.e., x and y), and each quarter sector of the aperture is a source of cross-polar radiation having alternating phases. Thus the far field pattern has nulls along the principal planes. Furthermore, for the WSR-88D antenna, (B.7.2) shows the peak of the aperture's cross-polar field is on the periphery of the aperture and along diagonals at  $\pm 45^\circ$ . We shall treat each sector as a source of radiation emanating from a phase center located at the center of gravity of the cross-polar aperture function (i.e., B.7.2) in each sector. Because the aperture distribution in each sector is symmetrical about the  $\varphi = 45^\circ$  diagonals, the four phase centers lie along these diagonals. Using (B.7.2) we compute the phase centers to be at the radial distance  $\rho_c = 0.356 D$ . The cross-polar radiation has a peak at an angle  $\theta_p$ , measured from the copolar beam axis (i.e., z axis), where radiation from each of the four sectors constructively add. The sectors either side of the diagonals always add in phase, but the sectors along the diagonal add in phase at

$$\theta_p = \sin^{-1} \left( \frac{\lambda}{2\rho_c} \right). \quad (\text{B.7.3})$$

For the KOUN parameters,  $\lambda = 0.11$  m and  $D = 8.53$  m, and thus  $\theta_p$  computes to be  $1.04^\circ$ . We conclude there are four principal lobes of cross-polar radiation, one each along the azimuthal directions  $\varphi = \pm 45^\circ$ , and  $\varphi = \pm 135^\circ$ , and at an angular displacement given by (B.7.3).

## B.8. References

- Balakrishnan, N., D. S. Zrníc, J. Goldhirsh, and J. Rowland, 1989: Comparison of simulated rain rates from disdrometer data employing polarimetric radar algorithms. *J. Atmos. Oceanic Technol.*, **6**, 476-486.
- Brandes, E., G. Zhang, and J. Vivekanandan, 2002: Experiments in rainfall estimation with a polarimetric radar in a subtropical environment, *J. Atmos. Meteor.*, **41**, pp. 674-685.
- Bringi, V. N., and V. Chandrasekar, 2001: Polarimetric Doppler Weather Radar. Cambridge University Press, Cambridge UK, 636 pp.
- Chandrasekar, V., and R. J. Keeler, 1993: Antenna pattern analysis and measurements for multiparameter radars. *J. Atmos. Oceanic Technol.*, **10**, 674-683.
- Deguchi, H., M. Tsuji, and H. Watanabe, 2008: Low-sidelobe multimode horn design for circular coverage based on quadratic programming approach. *IEICE Trans. Electron.*, **E91-C**, No 1, 3-8.
- Doviak, R.J., and D. S. Zrníc, 2006: Doppler radar and weather observations. Second edition, reprinted by Dover, Mineola, NY 562 pp.
- Doviak, R. J., V. Bringi, A. Ryzhkov, A. Zahrai, and D. Zrníc, 2000: Considerations for polarimetric upgrades to operational WSR-88D radars. *J. Atmos. Oceanic Technol.*, **17**, 257-278.
- Doviak, R. J., and D. Zrníc, 1998: Polarimetric upgrades to improve rainfall measurements. NOAA/NSSL technical report (WEB site: [http://publications.nssl.noaa.gov/wsr88d\\_reports/2pol\\_upgrades.pdf](http://publications.nssl.noaa.gov/wsr88d_reports/2pol_upgrades.pdf)) 110 pp.
- Durić, A., A. Magun, A. Murk, C. Mätzler, and N. Kämpfer, 2008: The Fully Polarimetric Imaging Radiometer SPIRA at 91 GHz. *IEEE Trans. Geosci. Remote Sens.*, **46**, 2323-2336.
- Fradin, A. Z., 1961: Microwave antennas. Pergamon Press, London, UK, pp. 668.
- Hubbert, J. C., M. Dixon, S. Ellis, and G. Meymaris, 2009: Simultaneous vertical and horizontal transmit radar data and polarization errors. 25th Conference on Interactive Information and Processing Systems (IIPS) for Meteorology, Oceanography, and Hydrology. Paper 15.4. AMS, Phoenix AZ.
- Ivić, I. R., D. S. Zrníc, and T. Y. Yu, 2009: Use of coherency to improve signal detection in dual-polarization weather radars. Accepted by *J. Atmos. Oceanic Technol.*
- Matrosov, S. Y., K. A. Clark, B. E. Martner, and A. Tokay, 2002: X-Band Polarimetric Radar Measurements of Rainfall. *J. Appl. Meteor.*, **41**, 941-952

Moisseev, D. N., C. M. N. Unal, H. W. J. Russchenberg, and L. P. Ligthart, 2002: Improved polarimetric calibration for atmospheric radars. *J. Atmos. Oceanic Technol.*, **19**, 1968-1977.

Paramax Systems Corp., 1992: Test report CDRL 246; Antenna pedestal, Part 1 of 4, Document #TR1218305, 1 July. Prepared by Paramax Systems Corp. for the U. S. Department of Commerce, Office of Procurement, Washington, DC 20230.

Potter, P. D., 1963: A new horn antenna with suppressed sidelobes and equal beamwidths. *Microwave Journal*, 71-78.

Ryzhkov, A. V., and D. S. Zrnice, 2007: Depolarization in ice crystals and its effect on polarization measurements. *J. Atmos. Oceanic Technol.*, **24**, 1256-1267.

Ryzhkov, A. V., S. E. Giangrande, V. M. Melnikov, and T. J. Schuur, 2005a: Calibration issues of dual-polarization radar measurements. *J. Atmos. Oceanic Technol.*, **22**, 1138-1155.

Ryzhkov, A. V., T. J. Schuur, D. W. Burgess, P. L. Heinselman, S. E. Giangrande, and D. S. Zrnice, 2005b: The Joint Polarization Experiment: Polarimetric rainfall measurements and hydrometeor classification. *Bull. American Met. Soc.*, **86**, 809-824.

Ryzhkov, A. V., and D. S. Zrnice, 1995: Comparison of dual-polarization radar estimators of rain. *J. Appl. Meteor.*, **12**, 249-256.

Sachidananda, M., and D. S. Zrnice, 1985:  $Z_{DR}$  measurement considerations for a fast scan capability radar. *Radio Sci.*, **20**, 907-922.

Sachidananda, M., and D.S. Zrnice, 1987: Rain Rate Estimates from Differential Polarization Measurements. *J. Atmos. & Oceanic Technol.*, **4**, 588-598.

Seliga, T. A., and V. N. Bringi, 1976: Potential use of radar differential reflectivity measurements at orthogonal polarizations for measuring precipitation. *J. Appl. Meteor.*, **15**, 69-76.

Wang, Y., V. Chandrasekar, and V. N. Bringi, 2006: Characterization and evaluation of hybrid polarization observation of precipitation. *J. Atmos. Oceanic Technol.*, **23**, 552-572.

Wang, Y., and V. Chandrasekar, 2006: Polarization isolation requirements for linear dual-polarization weather radar in simultaneous transmission mode of operation. *IEEE Trans. Geosci. Remote Sens.*, **44**, 2019-2028.

Zhang, G., J. Vivekanandan, and E. Brandes, 2001: A method for estimating rain rate and drop size distribution from polarimetric radar measurements. *IEEE Trans. Geosci. Remote Sens.*, **39**, 830-841.

Zrníc, D. S., A. Ryzhkov, J. Straka, Y. Liu, and J. Vivekanandan, 2001: Testing a procedure for automatic classification of hydrometeor types. *J. Atmos. Oceanic Technol.*, **18**, 892-913.

Zrníc, D. S., V. M. Melnikov, and J. K. Carter, 2006: Calibrating differential reflectivity on the WSR-88D. *J. Atmos. Oceanic Technol.*, **23**, 944-951.

## B.9. List of Figures

Fig. B.1. Fractional bias,  $\Delta R / R$ , of rain rate  $R$  vs differential reflectivity  $Z_{DR}$ , with bias  $\delta Z_{DR}$  as a parameter.

Fig. B.2. Cross sections through the copolar main lobe (largest circles) and cross-polar main lobes (shaded circles) for two types of cross-polar patterns: (a) A single cross-polar lobe centered on the beam axis of the copolar main lobe, (b) Four equal cross-polar lobes superposed on the copolar main lobe.

Fig. B.3. Envelopes of the maximum positive  $Z_{DR}$  bias normalized by  $W$  (linear scale), for  $\rho_{hv}=1$ , and the indicated values of the phases. Envelopes of the maximum negative bias are mirror images of these curves with respect to the abscissa.

Fig. B.4. The normalized bias versus  $Z_{DR}$  for an antenna having a cross-polar radiation pattern dominated by four cross-polar lobes which are equally spaced on a circle  $\theta_p$  from the copolar axis.

Fig. B.5. Cross-polar pattern functions  $|F_{hv}(\theta)|^2 / F_{hh}^4(0)$  (thick curve), and  $|F_{vh}(\theta)|^2 / F_{hh}^4(0)$  (thin curve) along the  $45^\circ$  diagonal of the OU PRIME antenna (frequency is 5.625 GHz).

Fig. B.6. a) The two-way pattern  $f_{hh}^4(\theta)$  (i.e., the solid thin curve), the normalized product  $F_{hh}^3 |F_{vh}| / F_{hh}^4(0)$  (i.e., the solid thick curve), and the normalized product  $F_{hh}^2 |F_{vh}|^2 / F_{hh}^4(0)$  (i.e., the dotted curve) in the E plane. b) Same as in a) except measurements are made in the H plane. c) Same as in a) but in the  $45^\circ$  plane.

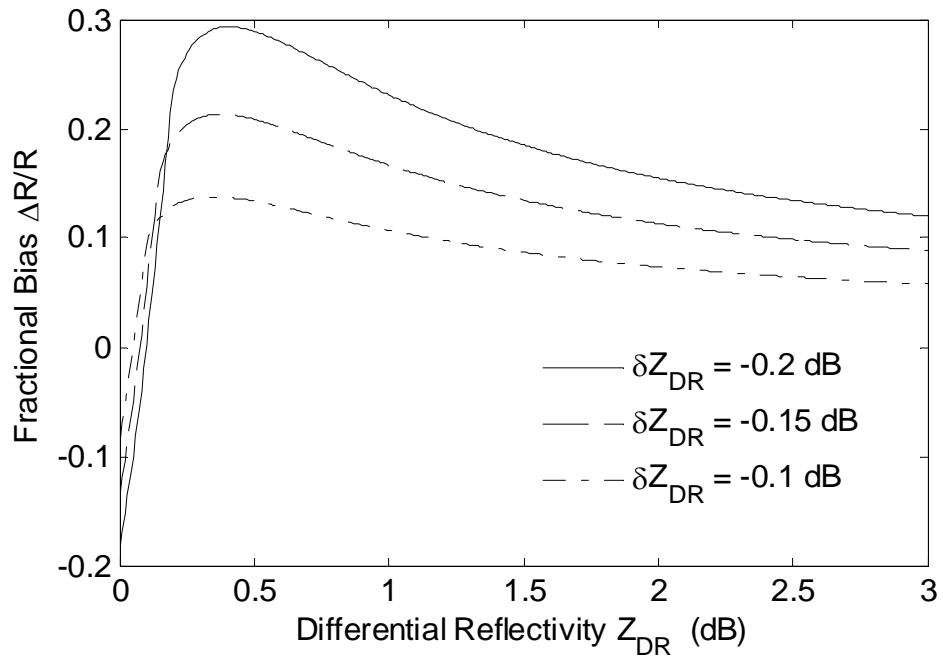


Fig. B.1. Fractional bias,  $\Delta R / R$ , of rain rate  $R$  vs differential reflectivity  $Z_{DR}$ , with bias  $\delta Z_{DR}$  as a parameter.

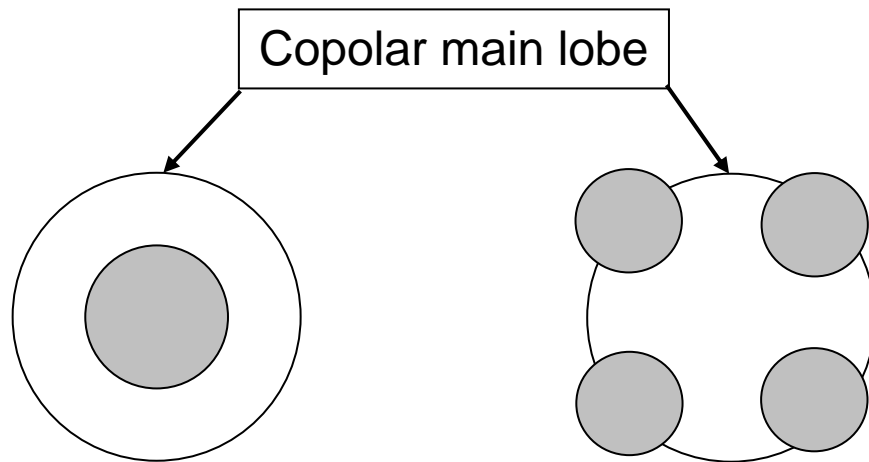


Fig. B.2. Cross sections through the copolar main lobe (largest circles) and cross-polar main lobes (shaded circles) for two types of cross-polar patterns: (a) A single cross-polar lobe centered on the beam axis of the copolar main lobe, (b) Four equal cross-polar lobes superposed on the copolar main lobe.

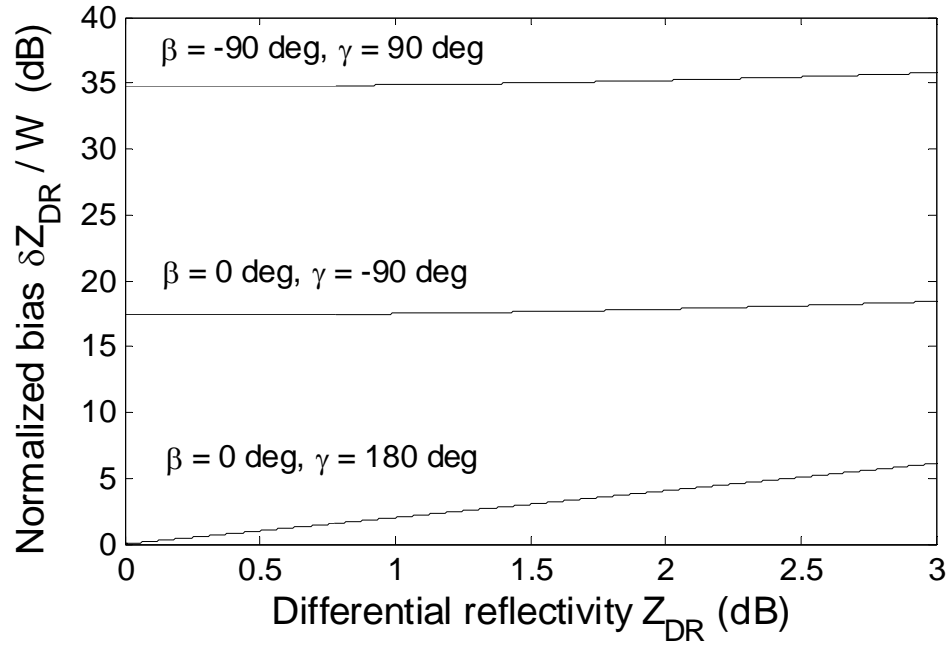


Fig. B.3. Envelopes of the maximum positive  $Z_{DR}$  bias normalized by  $W$  (linear scale), for  $\rho_{hv}=1$ , and the indicated values of the phases. Envelopes of the maximum negative bias are mirror images of these curves with respect to the abscissa.

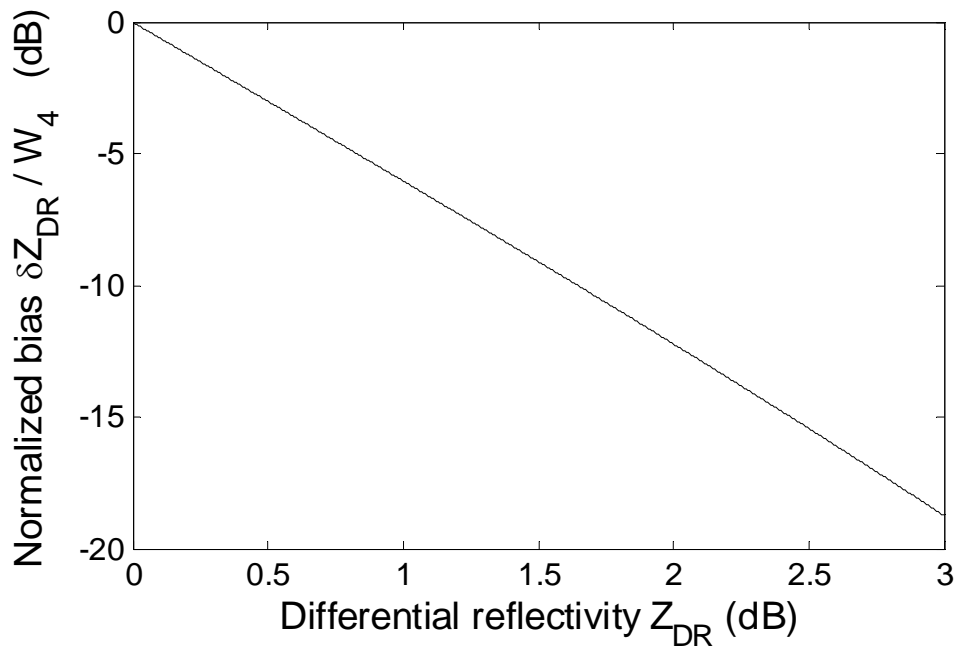


Fig. B.4. The normalized bias versus  $Z_{DR}$  for an antenna having a cross-polar radiation pattern dominated by four cross-polar lobes which are equally spaced on a circle  $\theta_p$  from the copolar axis.

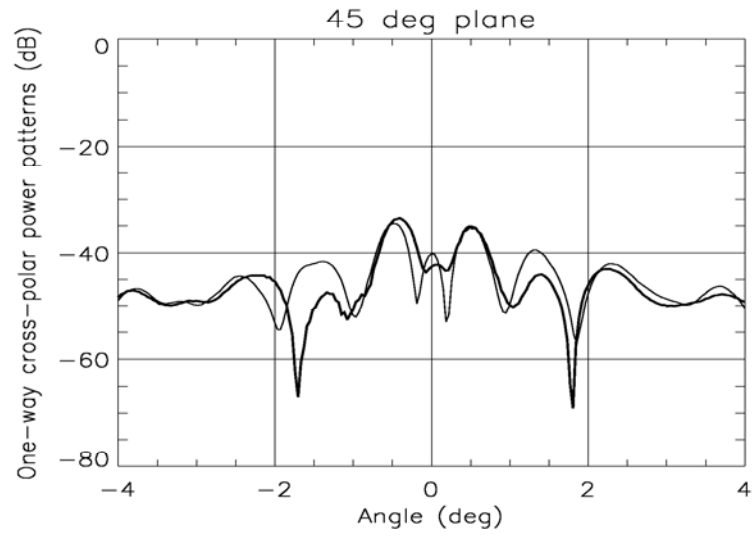


Fig. B.5. Cross-polar pattern functions  $|F_{hv}(\theta)|^2 / F_{hh}^4(0)$  (thick curve), and  $|F_{vh}(\theta)|^2 / F_{hh}^4(0)$  (thin curve) along the  $45^\circ$  diagonal of the OU PRIME antenna (frequency is 5.625 GHz).

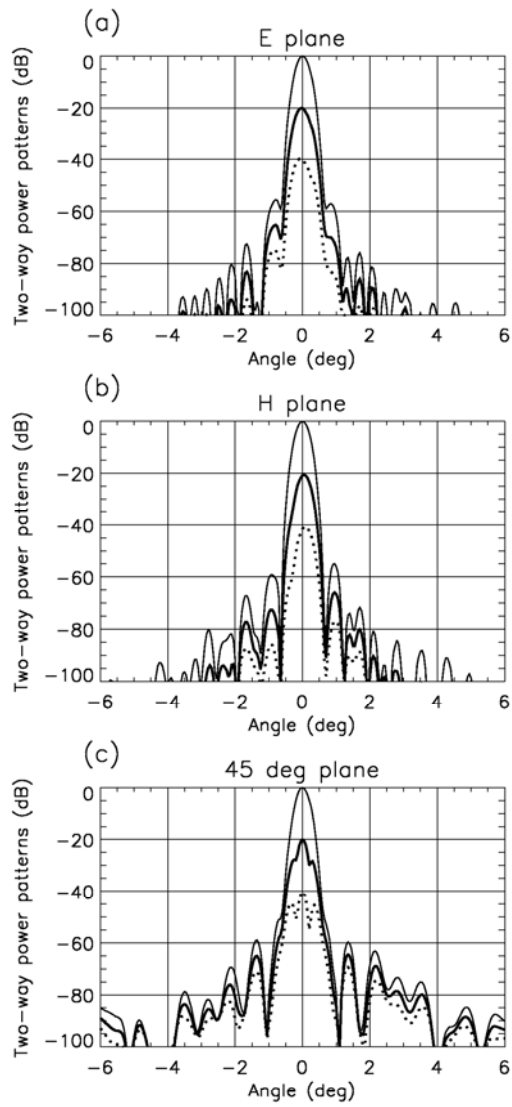


Fig. B.6. a) The two-way pattern  $f_{hh}^4(\theta)$  (i.e., the solid thin curve), the normalized product  $F_{hh}^3 |F_{vh}| / F_{hh}^4(0)$  (i.e., the solid thick curve), and the normalized product  $F_{hh}^2 |F_{vh}|^2 / F_{hh}^4(0)$  (i.e., the dotted curve) in the E plane. b) Same as in a) except measurements are made in the H plane. c) Same as in a) but in the  $45^\circ$  plane.

## Appendix C. Publications

The following conference papers were presented during FY09 and follow in their original form.

Torres, S., D. Zittel, and D. Saxion, 2009: Update on Development of Staggered PRT for the NEXRAD Network. Preprints, *25th International Conference on Interactive Information and Processing Systems (IIPS) for Meteorology, Oceanography, and Hydrology*, Phoenix, AZ, Amer. Meteor. Soc., Paper 11B.2.

Warde, D., and S. Torres, 2009: Range Overlaid Staggered PRT. Preprints, *25th International Conference on Interactive Information and Processing Systems (IIPS) for Meteorology, Oceanography, and Hydrology*, Phoenix, AZ, Amer. Meteor. Soc., Paper P2.2.

Torres, S., and D. Zrníć, 2009: Generalized SZ phase codes to mitigate range and velocity ambiguities. *34th International Conference on Radar Meteorology*, Williamsburg, VA. Amer. Meteor. Soc., Paper P5.10.

Sebastián Torres<sup>1</sup>, David Zittel<sup>2</sup>, and Darcy Saxion<sup>2</sup>

<sup>1</sup>Cooperative Institute for Mesoscale Meteorological Studies, The University of Oklahoma  
and NOAA/OAR National Severe Storms Laboratory, Norman, OK

<sup>2</sup>NOAA/NEXRAD Radar Operations Center, Norman, OK

## 1. INTRODUCTION

In the NEXRAD network, the range and Doppler velocity ambiguity problems are coupled such that trying to alleviate one worsens the other. Operationally, this is evidenced by the obscuration of overlaid weather echoes and/or the aliasing of measured Doppler velocities, both of which impair the effective observation of weather phenomena. Identified as one of the highest technical needs for the NEXRAD program, the Radar Operations Center (ROC) of the National Weather Service has sponsored the National Severe Storms Laboratory (NSSL) to develop signal processing methods for mitigating the effects of velocity and range ambiguities on the US weather radar network (Zrnić and Cook 2002). The first stage of this development was completed during 2007 with the operational deployment of a technique based on systematic phase coding termed as SZ-2 (Torres 2005). However, SZ-2 was designed to run only at the lower antenna elevation angles. Recently, NSSL recommended a staggered pulse repetition time (SPRT) algorithm for the second stage of deployment. This algorithm is based on a transmission sequence with two alternating pulse repetition times (PRT) and is suggested for intermediate to higher elevation angles of the antenna beam.

Comparisons with existing “legacy” algorithms have demonstrated the ability of SPRT to effectively mitigate range and velocity ambiguities (Torres 2006). However, the performance of this algorithm is limited by the accuracy of Doppler velocity estimates obtained for each PRT set. Large errors of estimates lead to dealiasing errors that cannot be effectively mitigated by the baseline NEXRAD velocity dealiasing algorithm (VDA). This paper presents a review of the SPRT algorithm, describes the performance of the algorithm in terms of velocity dealiasing errors, and illustrates the performance of a modified VDA to mitigate this particular class of errors. Finally, the status and plans for the operational deployment of the SPRT algorithm are outlined.

## 2. THE STAGGERED PRT ALGORITHM

The staggered PRT technique was first proposed in the context of weather surveillance radars by Sirmans et

---

*Corresponding author address:* Sebastián Torres, NSSL, 120 David L. Boren Blvd., Norman, OK 73072; email: Sebastian.Torres@noaa.gov

al. (1976). With this technique, transmitter pulses are spaced at alternating PRTs,  $T_1$  and  $T_2$ , and pulse-pair autocorrelation estimates are made independently for each PRT. These estimates are suitably combined so that the effective maximum unambiguous velocity can be extended to  $v_a = m\lambda/4T_1 = n\lambda/4T_2$ , where the stagger PRT ratio is given by  $T_1/T_2 = m/n$  ( $m$  and  $n$  are integers) and  $\lambda$  is the transmitter wavelength. In addition, the maximum unambiguous range is  $r_a = cT_1/2$ , corresponding to the shorter PRT ( $c$  is the speed of light). At the core of this technique is the generalized velocity dealiasing algorithm (Torres et al. 2004); to determine the Nyquist interval of the true velocity, it uses the fact that Doppler velocities obtained from the short and long PRTs alias in different ways.

The implementation of the staggered PRT technique on weather radars had been precluded from use mainly due to the difficulties in designing efficient ground clutter filters. However, a few years ago, Sachidananda and Zrnić (2002) proposed an efficient spectral clutter filter for staggered pairs that achieves clutter suppressions on par with those obtained for uniformly spaced samples. The recommended algorithm incorporates both the generalized velocity dealiasing algorithm and the spectral ground clutter filter.

## 3. VELOCITY DEALIASING ERRORS

The generalized velocity dealiasing algorithm at the core of SPRT fails if the variances of the short- and long-PRT velocity estimates are large. In such cases, the algorithm employs the wrong dealiasing rule and the resulting “dealiasing” velocity is significantly different from its true value. These types of dealiasing errors are termed “catastrophic” errors (Torres et al. 2004) because they may result in completely incorrect velocity estimates. “Catastrophic” errors are usually evident as speckle noise in the Doppler velocity image and can be easily removed by velocity dealiasing algorithms based on field continuity as will be demonstrated later. Still, the rate of catastrophic errors should be kept to a minimum to ensure that the speckling nature of these errors is preserved and that continuity-based velocity dealiasing algorithms can detect and correct these problems effectively.

Figure 1 shows the rate of catastrophic velocity errors expected for a volume coverage pattern (VCP) similar to VCP 11, but using staggered PRT. To get the required coverage in range, longer PRTs are needed at lower elevation angles resulting in larger velocity

variances. Hence, the rate of “catastrophic” errors is larger for the lower elevation angles. Also, wider spectrum widths lead to larger variance of Doppler velocity estimates and, as a result, to higher rates of “catastrophic” errors. However, “catastrophic” errors are almost negligible for all elevation angles if the spectrum widths are less than about 4 m/s.

As shown next, these sporadic dealiasing errors (i.e., the “catastrophic” errors) occurring in the WSR-88D Radar Data Acquisition (RDA) subsystem can be easily mitigated by velocity dealiasing techniques based on field continuity which are implemented in the Radar Product Generation (RPG) subsystem.

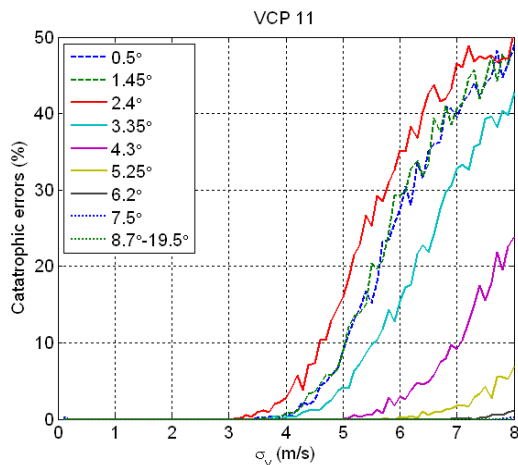


**Fig. 1.** Rate of catastrophic errors as a function of the spectrum width for all the tilts in the staggered PRT-based VCP 11 “clone”.

#### 4. THE VELOCITY DEALIASING ALGORITHM

In addition to the “catastrophic” errors described above, the SPRT algorithm may not fully resolve (dealias) velocities under strong wind conditions (i.e., the actual Doppler velocities exceed the extended unambiguous velocity). Therefore, further velocity dealiasing may be required. The WSR-88D RPG velocity dealiasing algorithm and its modifications to handle the “catastrophic” errors from SPRT are described next.

##### 4.1. General description

The Velocity Dealiasing Algorithm (VDA) for the NEXRAD system is an efficient dealiasing technique that processes one radial at a time but uses dealiased velocity from the preceding radial when available (Eilts and Smith 1990). The VDA runs in the WSR-88D system’s RPG.

Initially, each test velocity bin is compared to a nearby bin closer in range to the radar. If the test bin is within a threshold velocity difference it is assumed to have a good value. If not, the test bin is adjusted (dealias) by integral multiples of the Nyquist co-interval and the difference in values is again checked. If

the velocity cannot be adjusted to within a threshold velocity difference, an average of the 4 preceding bins in the current radial and the 5 bins farther in range in the previous radial is computed against which the test bin (or its dealiased value) is checked. If an average of the nearby velocities cannot be computed, the VDA looks farther back along the current radial or farther in range in the preceding radial for a good comparison velocity. If a comparison velocity still cannot be found, the VDA uses environmental wind data against which to test the velocity in the current bin. For each comparison velocity, if the test bin’s velocity cannot be dealiased to within a threshold velocity difference of the comparison velocity, it is set to a below signal-to-noise flag and the velocity saved for reinsertion into the radial later. The VDA allows a threshold number of consecutive velocities (nominally 4) to be removed before it reinserts them using relaxed thresholds. The original velocity value may be reinserted if, after dealiasing, its value cannot be adjusted to lie within a threshold velocity difference. Error-checking logic tries to correct unrealistically long runs of high azimuthal shear. Other error-checking logic looks for large gate-to-gate jumps in velocity but with opposite sign along the current radial. When found, the velocities between the large jumps are adjusted by an appropriate Nyquist co-interval. If a single large velocity jump in the current radial still exists, that radial is flagged as unusable for dealiasing velocity bins in the next radial and the previous radial’s data is retained for comparison. Otherwise, the current radial’s dealiased velocity data are saved for use by the next radial. An adaptable number of “bad” radials may be skipped before the VDA decides there is no valid previous radial.

At this point VDA has essentially completed dealiasing of the current radial but some bins may still be set to the below signal-to-noise flag. The velocities for these bins are reinserted into the radial with their original values if they cannot be adjusted by a multiple of the Nyquist co-interval using a relaxed velocity difference threshold. The velocities reinserted in this last step have no influence on future dealiasing.

##### 4.2. VDA changes to support SPRT

The baseline VDA cannot dealias the velocities resulting from “catastrophic” errors introduced by the SPRT but instead, places them back in a radial with their original values. Because many of the velocity difference thresholds used by the VDA are derived from the Nyquist velocity, notably for the final reinsertion step, a simple solution is to allow the VDA to use the Nyquist velocity corresponding to  $v_a = \lambda/4T_1$  which is half the extended Nyquist velocity. It is appropriate to use  $v_a$  for  $T_1$  because dealiased velocity estimates provided by the SPRT algorithm are computed from  $T_1$ .

In regions of weak signal, more than 4 consecutive bins may have “catastrophic” errors. These bins would have been filled in by the VDA with their original values during the first reinsertion process and so would not be dealiased using  $v_a$  for  $T_1$ . However, the number of consecutive bins that may be flagged as missing may be increased thus allowing for more recovery of

“catastrophic” errors. The following figures will illustrate the improvements from these simple changes. Figure 2 shows a small region of velocity data dealiased using the baseline VDA. While the overall field has been dealiased correctly, there are numerous bins that do not fit the strong outbound flow. Figure 3 shows that the noisy velocities can be greatly mitigated by allowing the VDA thresholds to be rescaled using half the extended Nyquist velocity. Some remaining regions of noisy velocity may be further “cleaned up” by increasing the number of consecutive bins that may be removed from 4 to 9 as shown in Figure 4. However, care must be taken to not remove too many bins. Figure 5 shows the reflectivity field corresponding to the velocity images. A strong storm core is seen at 70 nautical mile (nmi) range, 75 deg azimuth and also just beyond 50 nmi, about 130 deg azimuth. These cores may act as a barrier to the outbound velocities. The near-zero velocities just upstream of them may, therefore, be entirely realistic.

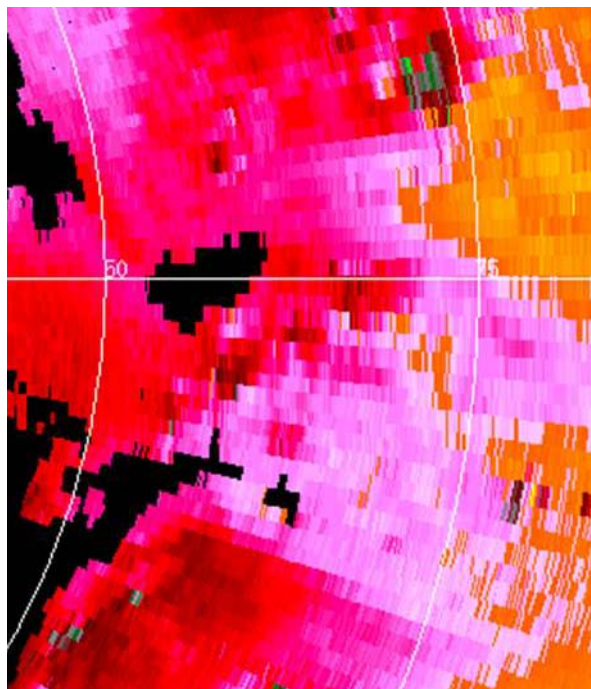


**Fig. 3.** Same as Fig. 2 but the final bin reinsertion for VDA uses the Nyquist velocity corresponding to the shorter PRT.

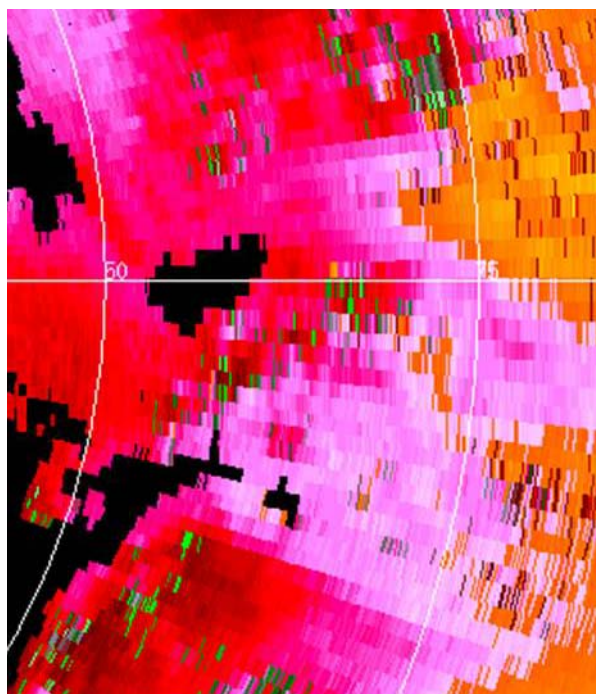


**Fig. 2.** SPRT velocity field from March 31, 2008, 1951Z at 3.1 deg elev. dealiased using baseline VDA. Range rings are every 25 nmi. Note numerous bins with velocities that do not fit the general flow. Warm colors show flow away from the radar; cool colors show flow towards the radar. See legend in Fig. 8 for corresponding velocities.

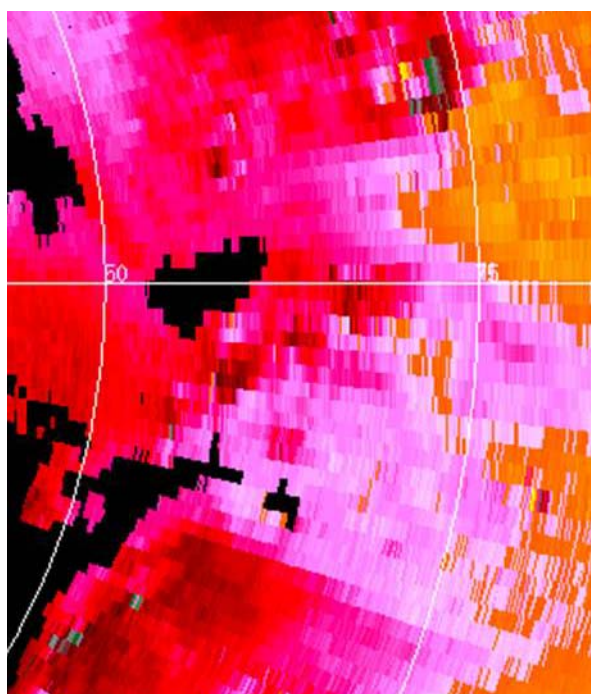


**Fig. 4.** Same as Fig. 3 but the number of bins VDA may initially remove is changed from 4 to 9. Note further reduction in bins with velocities that do not fit the overall flow.

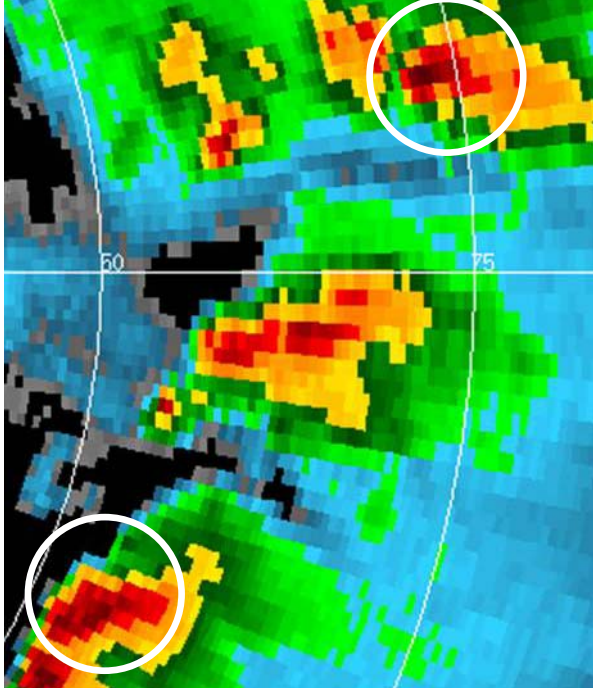


**Fig. 5.** Reflectivity corresponding to the velocity fields in Figs. 2-4. Note the juxtaposition of near zero velocities with strong cores upper right and lower left (circles). See legend in Fig. 7 for dBZ values.

## 5. OPERATIONAL STATUS AND PLANS

The ROC is responsible for implementing and integrating new science into the NEXRAD network. A good example of this process is given by ongoing effort to implement signal processing techniques for the mitigation of range and velocity ambiguities. Both the SPRT algorithm for the RDA subsystem and the modified VDA for the RPG subsystem are in the process of being incorporated into the WSR-88D. As mentioned in the introduction, staggered PRT is only one part of an overarching effort to improve the mitigation of range and velocity ambiguities on the NEXRAD network.

The ROC is developing SPRT in three phases. The first phase was an investigation and decision phase. It was completed in August of 2007. During that time, the ROC compared the NSSL SPRT algorithm with the Vaisala/SIGMET Dual PRT (DPT2) algorithm. While the DPT2 is a very good algorithm, the NSSL approach provided additional flexibility for any form of PRT ratio and an approach to manage overlaid signals. During phase I, the Vaisala/SIGMET DPT2 major mode was enabled so that we could transmit staggered PRT pulse sequences as part of engineering tests. ROC engineers recorded time series data from those tests which were used later for analysis and testing.

The ROC implemented the NSSL SPRT algorithm during the second phase of development. SPRT was implemented in a user major mode on the RDA signal processor, the Vaisala/SIGMET RVP8. The initial

implementation of SPRT uses a DC removal clutter filter. The performance of this filter does not meet WSR-88D clutter suppression requirements; therefore, the new user major mode is non-operational at this time. However, the second phase established the architecture and basic algorithm on which improved clutter filtering can be added. The second phase of SPRT is nearly complete.

Phase II algorithm implementation also allowed for some preliminary comparisons between the current ORDA batch mode and SPRT. On May 07, 2008, a widespread rain event with embedded convective cells passed through central Oklahoma. KTLX, the Oklahoma City radar, was running VCP 12 which runs batch mode signal processing at the mid-level tilts. KCRI, the ROC test radar, was running engineering test VCP 15, which is a "clone" of VCP 12 except that it runs SPRT at the mid-level tilts. Figures 6 and 7 show the reflectivity and Doppler velocity fields from KTLX at an elevation of 1.8 deg obtained with batch processing. The reflectivity is estimated from pulses transmitted at a PRT of 3140  $\mu\text{sec}$ ; which provide a maximum unambiguous range of 252 nmi. The velocity is estimated from pulses transmitted at a PRT of 1000  $\mu\text{sec}$ , which gives a maximum unambiguous range of 80 nmi and a maximum unambiguous velocity of  $24 \text{ m s}^{-1}$ . Note the areas of overlaid echoes (purple haze) that are typical when using shorter PRTs. Figure 8 shows KCRI's Doppler velocities obtained with SPRT processing at nearly the same time and at the same elevation angle. SPRT used a 2/3 PRT ratio of 1740  $\mu\text{sec}/2160 \mu\text{sec}$ . This combination of PRTs provides a maximum unambiguous velocity of  $28 \text{ m s}^{-1}$  and a maximum unambiguous range of 141 nmi. Note the increased coverage in range with similar maximum unambiguous velocities. Both the KTLX and KCRI velocity products have been processed by the improved VDA algorithm on the RPG described in the previous section.

The ROC is beginning the third phase of SPRT. During this phase the ROC will add NSSL's Spectral Algorithm for Clutter Harmonics Identification and removal (SACHI) clutter filter. In addition, the ROC will analyze SPRT-derived base moments to verify that they meet WSR-88D requirements. Another task of phase three is to define optimal PRTs so that both SPRT and the clutter filter have the best performance while maintaining the fastest possible scan rate for minimal Volume Coverage Pattern (VCP) update times. The ROC envisions a VCP that mitigates both range folding and velocity dealiasing by enabling SZ-2 on the lower split-cuts and SPRT on all the remaining upper cuts. The target build for SPRT is Build 13.

The changes to the VDA have been made in a parallel effort with the development of the SPRT Major Mode. The completed upgrades to the VDA will be available in Build 12 whenever SPRT Major Mode is enabled. During the implementation and testing of the SACHI clutter filter, the ROC will perform more testing, data collection, and analysis including changes to the VDA.

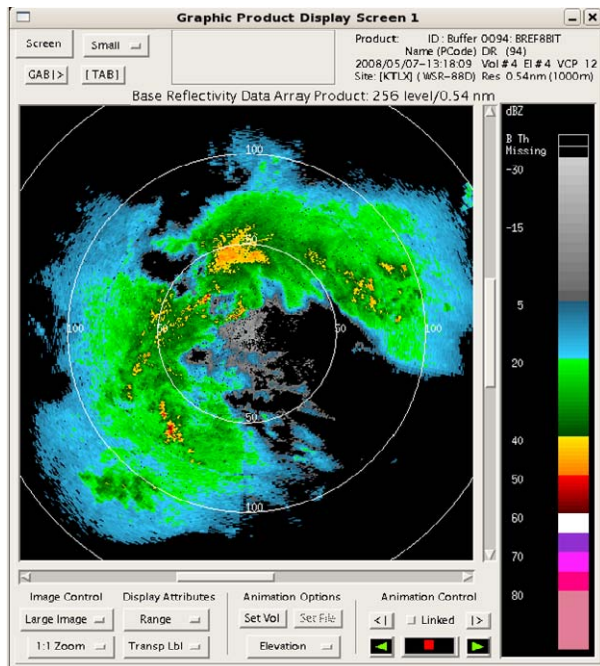


**Fig. 6.** KTLX reflectivity, elevation 1.8°, batch mode processing, Surveillance PRT 3140  $\mu\text{sec}$ , unambiguous range 252 nmi.

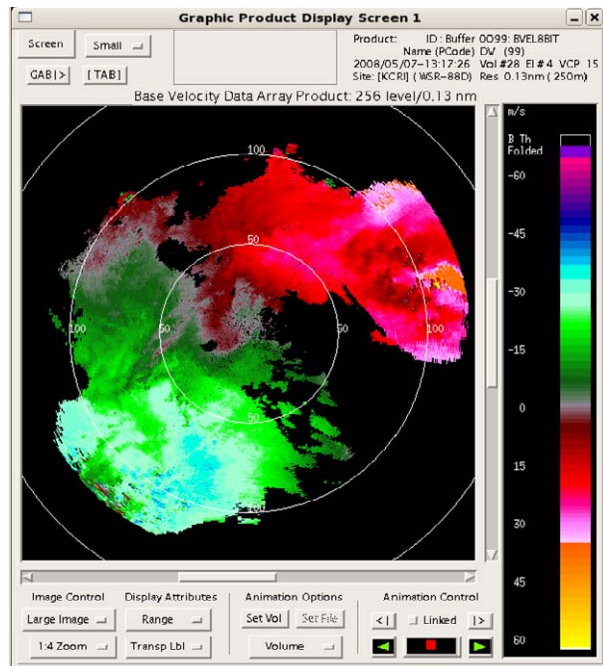


**Fig. 8.** KCRI Doppler velocity, elevation 1.8°, SPRT mode processing, PRT Ratio 2/3, PRT 1740  $\mu\text{sec}$ /2160  $\mu\text{sec}$ , unambiguous range of 141 nmi, unambiguous dealiased velocity of 28  $\text{m s}^{-1}$ .

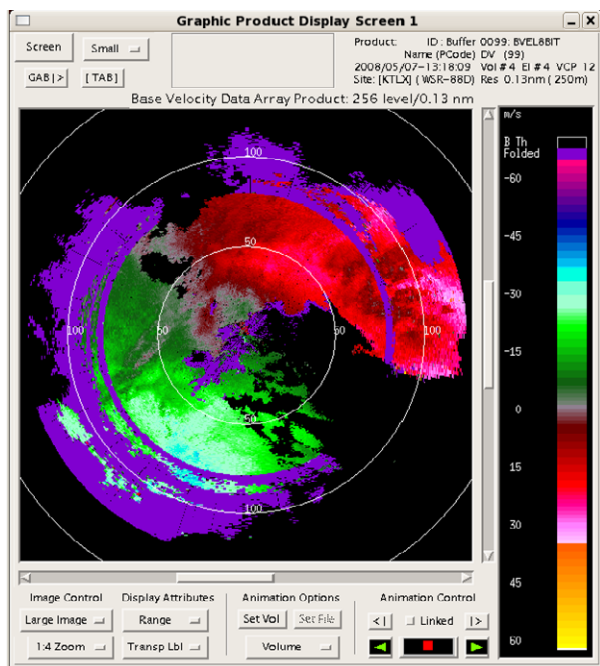


**Fig. 7.** KTLX Doppler velocity, elevation 1.8°, batch mode processing, Doppler PRT 1000  $\mu\text{sec}$ , unambiguous range of 80 nmi, unambiguous velocity of 24  $\text{m s}^{-1}$ .

## 6. CONCLUSIONS

In an effort to improve the effective observation of weather phenomena, the ROC and the NSSL are working together to develop and implement SPRT with clutter filtering as a velocity aliasing mitigation technique. That, in conjunction with VDA upgrades that will correct for the occasional “catastrophic” SPRT dealiasing error, will greatly mitigate velocity aliasing on the WSR-88D. The ROC is working towards having SPRT with clutter filtering and VDA upgrades operational by Build 13.

## ACKNOWLEDGMENT

This conference paper was prepared (in part) by Sebastián Torres with funding provided by NOAA/Office of Oceanic and Atmospheric Research under NOAA-University of Oklahoma Cooperative Agreement #NA17RJ1227, U.S. Department of Commerce. The statements, findings, conclusions, and recommendations are those of the author(s) and do not necessarily reflect the views of NOAA or the U.S. Department of Commerce.

## REFERENCES

- Eilts M. D. and S. D. Smith, 1990: Efficient Dealiasing of Doppler Velocities Using Local Environment Constraints. *J. Atmos. Oceanic Technol.*, **7**, 118-128.
- Sachidananda M. and D. S. Zrnčić, 2002: An Improved Clutter Filtering and Spectral Moment Estimation Algorithm for Staggered PRT Sequences. *J. Atmos. Oceanic Technol.*, **19**, 2009–2019.
- Sirmans, D., D. Zrnčić, and B. Bumgarner, 1976: Extension of maximum unambiguous Doppler velocity by use of two sampling rates. Preprints, *17th Conf. on Radar Meteorology*, Seattle, WA, Amer. Meteor. Soc., 23-28.
- Torres, S., 2005: Range and velocity ambiguity mitigation on the WSR-88D: Performance of the SZ-2 phase coding algorithm. Preprints, *21st International Conf. on IIPS*, San Diego, CA, Amer. Meteor. Soc., Paper 19.2.
- Torres, S., 2006: Range and velocity ambiguity mitigation on the WSR-88D: Performance of the staggered PRT algorithm. Preprints, *22nd International Conf. on IIPS*, Atlanta, GA, Amer. Meteor. Soc., Paper 9.9.
- Torres, S. M., Y. F. Dubel, and D. S. Zrnčić, 2004: Design, implementation, and demonstration of a staggered PRT algorithm for the WSR-88D, *J. Atmos. Oceanic Technol.*, **21**, 1389-1399.
- Zrnčić, D. and R. Cook, 2002: Evaluation of techniques to mitigate range and velocity ambiguities on the WSR-88D. Preprints, *18<sup>th</sup> International Conf. on IIPS*, Orlando, FL, Amer. Meteor. Soc., paper 5.13.

David A. Warde\* and Sebastián M. Torres  
 Cooperative Institute for Mesoscale Meteorological Studies, The University of Oklahoma, and  
 NOAA/OAR National Severe Storms Laboratory, Norman, Oklahoma

## ABSTRACT

Limitations in resolving both range and velocity unambiguously arise from uniform sampling as is typically done in Doppler weather radars. If the sampling period or pulse repetition time (PRT) is made large for extended range coverage, no overlaid conditions occur, but Doppler velocity measurements become ambiguously aliased. Conversely, if the PRT is made small to unambiguously resolve velocities, range-overlaid signals become more likely. Staggered Pulse Repetition Time (SPRT) has been shown (Sirmans 1976, Sachidananda and Zrnić 2003, Torres et al. 2004) to mitigate range and velocity ambiguities by decreasing velocity aliasing while extending the radar coverage. In other words, with the proper choice of PRTs, SPRT can eliminate the occurrence of overlaid echoes without sacrificing velocity aliasing. However, the performance of the SPRT algorithm to accurately dealias Doppler velocities deteriorates as the spectrum width of the weather signal increases in relation to the Nyquist interval. By allowing some overlaid signals to occur, shorter PRTs can be used to increase the SPRT dealiasing performance.

In this paper, we explore the use of range-overlaid SPRT as a means to improve the quality of Doppler velocity estimates. Additionally, we present a method to recover velocities beyond the unambiguous range of the standard SPRT algorithm.

## 1. INTRODUCTION

In Doppler weather radar systems like the WSR-88D, it is desirable to unambiguously track weather at long distances while estimating the velocity unambiguously. However, when uniform sampling is utilized, unambiguous resolution in both range and velocity is generally not realized. That is, the mitigation of range (velocity) usually results in the ambiguity of the weather velocity (range). The relationship is such that the product of unambiguous range ( $r_a$ ) and unambiguous velocity ( $v_a$ ) is constant for a specified radar wavelength:

$$r_a v_a = c\lambda / 8 \quad (1)$$

---

\* Corresponding Author Address: David A. Warde, CIMMS/University of Oklahoma, National Severe Storms Laboratory, National Weather Center, 120 David L. Boren Blvd. Norman, OK, 73072; [David.A.Warde@noaa.gov](mailto:David.A.Warde@noaa.gov)

where  $c$  is the speed of light and  $\lambda$  is the wavelength of the transmitted pulse.

Because of the large range extent and significant velocities associated with weather conditions, SPRT has been suggested (Sirmans 1976) as a viable means to reduce the ambiguity that arises in both range and velocity. Zrnić and Mahapatra (1985) showed that when SPRT is used, the range and velocity product can be extended:

$$r_a v_a = \left( \frac{c\lambda}{8} \right) \left( \frac{1+\kappa}{1-\kappa} \right) \quad (2)$$

where  $\kappa$  is the constant of proportionality between  $T_1$  and  $T_2$  (i.e.  $T_1 / T_2$ ) with  $T_2 > T_1$ . Thus, with the proper choice of  $T_1$  and  $T_2$ , both range and velocity can be unambiguously determined.

Practical limits exist for any system. For the WSR-88D, Torres et al. (2004) evaluated the system limitations and provided a general SPRT algorithm description that realizes the theoretical maximum extent in velocity utilizing velocity difference transfer functions for any choice of the constant of proportionality  $\kappa$ . The SPRT algorithm described assumes that the weather extent does not exceed the unambiguous range of the longest PRT ( $T_2$ ) guaranteeing that reflectivity (power) can be estimated without any overlaid echoes. Additionally, the algorithm allows recovery of Doppler moments (velocity and spectrum width) within the shortest PRT ( $T_1$ ) but allows overlaid echoes to occur. This algorithm is being implemented into the WSR-88D system (Torres et al. 2009) with a  $\kappa$  of 2/3.

Since weather signals are allowed to overlay, an overlay determination is needed to recover Doppler moments in regions where overlays could occur. If weather signals overlay, the stronger signal dominates the Doppler estimates. These Doppler estimates can be recovered if the power ratio (stronger-to-weaker) exceeds a level such that the bias and standard deviation are reasonably low. Sirmans studied the Doppler moment bias associated with overlaid occurrences in a uniformly sampled environment (Sirmans 1990 and Sirmans 1998). He found that biases in velocity estimates can be maintained below 1 m/s for the stronger weather signal when the power ratio exceeds 5 dB; whereas, the weaker weather signal is unrecoverable. Later, he found that spectrum width overlaid power ratio needed to be about 20 dB to provide useful spectrum width estimates for the stronger weather signal. The focus of this paper is to provide overlaid threshold values such that the Doppler

moments can be reliably estimated to some accuracy for the SPRT algorithm.

## 2. OVERLAID ECHOES IN SPRT

The SPRT uses alternate pulses transmitted at two PRTs ( $T_1$  and  $T_2$ ). For this paper, the algorithm described by Torres et al. (2004) with  $\kappa = 2/3$  ( $T_1 = \kappa T_2$ ) is used. With the proper choice of  $T_1$  and  $T_2$ , overlaid weather echoes can be avoided as shown in figure 1a. The algorithm allows overlaid echoes to extend beyond the receive time of  $T_1$  (figure 1b), but not beyond the receive time of  $T_2$  (figure 1c). The receive times can be broken into regions that are half of the receive time of  $T_1$ . Thus, two regions are created for  $T_1$  (I and II), and three regions are created for  $T_2$  (I, II, and III). Note in figure 1b that during receive time for region II in both  $T_1$  and  $T_2$  there are no overlaid echoes. Additionally, in figure 1b, there are no overlaid echoes in region I for  $T_1$  and region III for  $T_2$ . As mentioned before, this allows the reflectivity (power) to be recovered unambiguously in all three regions. That is, the reflectivity estimate is recoverable to the maximum extent of the unambiguous range of  $T_2$  ( $r_{a2} = cT_2 / 2$ ) without overlaid echoes biasing the estimates. Thus, the reflectivity (power) becomes a useful means of determining the amount of overlay that occurs in region I and region III.

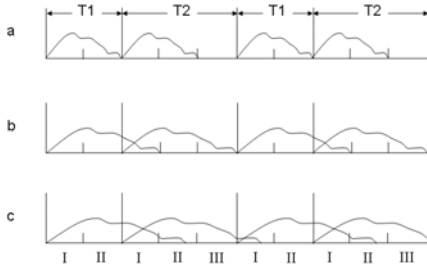


**Figure 1. Overlaid Weather in SPRT.**

In the algorithm, Doppler moments for region I are calculated from the lag-one autocorrelation between pulses  $T_1$  and  $T_2$ . In fact, the difference of two lag-one autocorrelations is used for the final velocity estimate. The two autocorrelations are constructed as:

$$R_{12}(n,1) = \frac{2}{M} \sum_{m=0}^{M/2-1} V^*(n,2m)V(n,2m+1) \quad (3)$$

$$R_{21}(n,1) = \frac{2}{M-2} \sum_{m=0}^{M/2-2} V^*(n,2m+1)V(n,2m+2) \quad (4)$$

Where the  $xx$  in  $R_{xx}$  is the lag-one autocorrelation from pulse to pulse (i.e., equation 3 is from  $T_1$  to  $T_2$  and equation 4 is from  $T_2$  to  $T_1$ ),  $n$  is the range gate index within  $T_1$ ,  $M$  is the number of pulse samples,  $V$  is the voltage measured, and  $m$  is the pulse index. For the sake of simplicity, we assume that the sequence of

pulses starts with  $T_1$  and  $M$  is even. For a generalized approach, the reader is referred to Torres et al. (2004).

Region III Doppler moments are not recovered using the algorithm described by Torres. However, another set of lag-one autocorrelations can be constructed in range from only the  $T_2$  pulses:

$$R_{22}(n,1) = \frac{2}{M-2} \sum_{m=0}^{M/2-2} V^*(n,2m+1)V(n+N_1,2m+1) \quad (5)$$

$$R_{22}(n,1) = \frac{2}{M-4} \sum_{m=0}^{M/2-3} V^*(n+N_1,2m+1)V(n,2m+3) \quad (6)$$

Here, all variables are as before, except that  $n$  is restricted to range gates occurring in the first half of  $T_1$  and  $N_1$  is the number of range gates in  $T_1$ .

From figure 1b, it is seen that only the region I pulses from  $T_2$  can be overlaid. In equations 3 and 4, the odd pulses ( $2m$  and  $2m+2$  with index starting at 0) are from region I of  $T_1$  and the even pulses are from region I of  $T_2$ . In equations 5 and 6, all the pulses are from  $T_2$ . Thus, overlaid echoes can only occur in the range gates for  $n$  and not for  $n+N_1$ .

At this point, it becomes necessary to introduce the SPRT kernel [10100]. The SPRT kernel represents the smallest periodic sampling of the sequences of voltages from  $T_1$  and  $T_2$  when placed in their appropriate time slots in the uniform sampling  $T_u = T_2 - T_1$  (e.g. Sachidananda and Zrnić 2003). In the kernel, a 1 represents the presence of a pulse and a 0 represents the absence of a pulse. In this way, the SPRT sequence can be seen as the product of the periodic extension of the SPRT kernel with a sequence of uniformly sampled voltages at a PRT equal to  $T_u$ .

Following the previous discussion, let's introduce the overlaid kernels. The overlaid kernel from equations 3 and 5 is [00100] and the overlaid kernel from equation 4 and 6 is [10000]. The overlaid kernels result from the occurrence of overlaid echoes from region I of  $T_2$  in the above lag-one autocorrelations. A 1 in the overlaid kernels represents the presence of an overlaid echo; whereas, a 0 represents no overlaid echo or the absence of a pulse.

Comparing the overlaid kernels to the SPRT kernel it is easy to see that only half the power of the overlaid echoes contaminates the Doppler estimates (i.e. every other pulse is contaminated by overlaid echoes). There is an additional benefit that is not readily seen, but is very apparent when comparing the power spectra of the three kernels. That is, both overlaid spectra are evenly distributed across the SPRT spectrum. In figure 2, the SPRT kernel spectrum (blue) is shown against the overlaid kernel spectra (red). Note that both overlaid cases have the same power spectrum and that the power in the central coefficient of the SPRT kernel is 6 dB greater than any of the overlaid kernel coefficients.

Finally, consider the correlation between the overlaid signal and the true signal. Zrnić and Mahapatra (1985) convincingly argue that overlaid echoes will not

coherently contribute to the bias of the Doppler estimates, but they warn that the overlaid echoes will increase the standard error of estimates.

The lack of correlation between the overlaid and true signal along with the preceding overlaid kernel discussion suggest that SPRT can tolerate overlaid echoes better than with uniform sampling. Specifically, the power ratio for SPRT can be at least 6 dB lower than the power ratio for uniform sampling as formulated by Sirmans (1990, 1998).

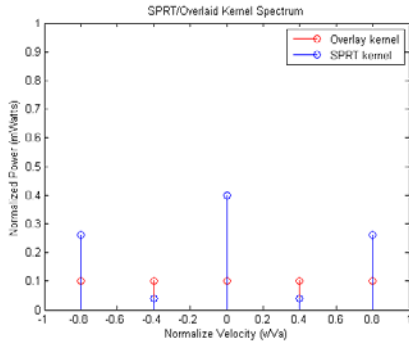


Figure 2. Comparison of kernel spectra.

### 3. EVALUATION METHOD

The standard model for weather simulations is a Gaussian spectrum (e.g. Doviak and Zrnić 1993). To construct the simulation of overlaid echoes in region I and III of SPRT, two uncorrelated uniform time series ( $V_a$  and  $V_b$ ) are created at a PRT ( $T_U = T_1/2$ ) as described by Sachidananda and Zrnic (2003). A third time series ( $V_c$ ) is created as the composite of delayed  $V_a(t+2)$  and  $V_b(t)$ . For region I,  $V(n,m)$  ( $n \leq N_1/2$ ,  $m=0:2:M-2$ ) is created from every fifth pulse of  $V_a$  starting with the first pulse. Then, using every fifth pulse of  $V_c$  starting with the first pulse, fill in  $V(n,m)$  ( $n \leq N_1/2$ ,  $m=1:2:M-1$ ). For region III,  $V(n+N_1,m)$  ( $n \leq N_1/2$ ,  $m=1:2:M-1$ ) is created from every fifth pulse of  $V_b$  starting with the third pulse. For region II,  $V_a$  is used to create  $V(n,m)$  ( $N_1/2 < n \leq N_1$ ,  $m=0:M-1$ ) by taking only those samples that match the ones in the periodic extension of the SPRT kernel ( $\kappa=2/3$ ), all other pulses are dropped. In figure 3, each region is shown along with the time series that is used in the region. To summarize,  $V_a$  is used in regions I and II (not necessarily the same  $V_a$ ),  $V_b$  is used in region III, and  $V_c$  (delayed  $V_a + V_b$ ) is used in region I.

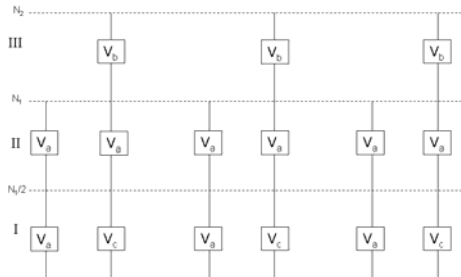


Figure 3. SPRT time series construction.

With this construction, a set of time series simulations were created and passed to the algorithm described by Torres et al. (2004) with the addition of the lag-one autocorrelations (equations 5 and 6) to recover Doppler moments in region III. The parameters for the simulation are listed in table 1. The true velocity was varied over the range from -100 m/s to 100 m/s across regions I and II; while, the true velocity was varied from 50 m/s to -50 m/s in region III. Since the unambiguous velocity is only 50 m/s, the true velocity in regions I and II aliases. The signal-to-noise (SNR) was held constant at 20 dB in regions I and II. In region III, the SNR was varied from 0 dB to 40 dB.

Table 1. Simulation Parameters

Parameter	Value
$\lambda$	~10 cm
$T_1$	1002 $\mu$ s
$T_2$	1503 $\mu$ s
$N_1$	600 bins
$N_2$	900 bins
$r_{a1}$ (for $T_1$ )	150 km
$r_{a2}$ (for $T_2$ )	225 km
$V_a$	50 m/s
$V_{true}$	-100 m/s to 100 m/s (bins 1 to 600) 50 m/s to -50 m/s (bins 601 to 900)
$SNR_1$	20 dB
$SNR_2$	20 dB
$SNR_3$	0 dB to 40 dB
$\sigma_v$	4 m/s
$\kappa$	2/3

Figures 4 through 9 show three plots: SNR (top), velocity (middle), and spectrum width (bottom). The solid green lines in regions I and II are the true values; whereas, the solid red line in region III represents the true values. The overlaid signals are shown with dashed lines. The dashed green line in region III is the overlaid signal from region I, and the dashed red line in region I is the overlaid signal from region III. There are no overlaid signals in region II. Note that the dashed green line for velocity shows the true velocity as being aliased. The blue line represents the estimates of the moments.

In figure 4, the power ratio ( $S_1/S_2$ ) is 20 dB. As mentioned, the power estimate is never overlaid and should provide quality estimates regardless of the power ratio. However, the Doppler moments are influenced severely by the overlaid echoes with a power ratio of 20 dB. The velocity and spectrum widths are recoverable in region I but not in region III. Note that the velocity is aliased in region I and II. This behavior is expected and will occur if the true velocity exceeds the unambiguous velocity (50 m/s).

The power ratio is reduced to 10 dB in figure 5. Note that the velocity is very good (low variance) in region I; whereas the spectrum width is starting to deteriorate. At a power ratio of 0 dB in figure 6, the velocity is completely recoverable in all regions, but the spectrum width has high variance in both regions I and III. By decreasing the power ratio to -5 dB in figure 7

(i.e. region III has the stronger signal), the velocity exhibits low variance and is still recoverable in all regions. However, the spectrum width has a high variance in regions I and III, but is starting to improve in region III. As the region III signal becomes more dominant in figures 8 and 9 with power ratios of -10 dB and -20 dB respectively, the region III Doppler moments experience less influence from the region I overlaid signal. Consequently, the Doppler moments exhibit less variance in region III.

#### 4. SUMMARY

An improvement to the SPRT algorithm is shown that allows recovery of Doppler moments beyond the unambiguous range of the shortest PRT. For a given dwell time, moment estimates are better when using a shorter PRT because more pulses are collected. This is true in SPRT as well. With the implementation of the new lag-one autocorrelations, the range coverage for Doppler moments is increased by 50 percent allowing the use of a shorter PRT for the same Doppler coverage. In turn, the use of a shorter PRT provides improved estimates.

Although the analysis is preliminary, it is evident that acceptable recovery of Doppler estimates (velocity and spectrum width) in the presence of overlaid echoes is possible. In fact, the simulations indicate that velocity recovery in both regions I and III is possible if the strongest signal is not more than 5 dB stronger than the weakest signal. This suggests that there is a 10 dB overlap region where the power ratio (strongest signal to weakest signal) is between 0 dB and 5 dB allowing recoverable velocities for both regions. In the uniform sampling reported by Sirmans (1990) the stronger signal velocity is unrecoverable when the power ratio is below 5 dB. Additionally, spectrum width is shown to be recoverable if the power ratio (strongest signal to weakest signal) is above 10 dB indicating about a 10 dB improvement over uniform samples at 20 dB as reported by Sirmans (1998).

Part of the reason for the better performance of SPRT is because only half of the overlaid signal is contaminating the Doppler spectrum. Other factors that improve the recovery of overlaid echoes are the incoherency and even distribution of the overlaid signal in the SPRT spectrum. It was shown in figure 2 that the SPRT spectrum is 6 dB above the overlaid spectrum. Nevertheless, the simulations show that about 10 dB of improvement over uniform sampling is achieved.

#### 5. ACKNOWLEDGEMENTS

This conference paper was prepared by David Warde and Sebastián Torres with funding provided by NOAA/Office of Oceanic and Atmospheric Research under NOAA-University of Oklahoma Cooperative Agreement #NA17RJ1227, U.S. Department of Commerce. The statements, findings, conclusions, and recommendations are those of the authors and do not necessarily reflect the views of NOAA or the U.S. Department of Commerce.

#### 6. REFERENCES

- Doviak, D. and D. Zrnić, 1993: Doppler Radar and Weather Observations, 2<sup>nd</sup> edition. Academic Press pp 87-105, 125.
- Sachidananda, M., D. Zrnić, 2003: Unambiguous range extension by overlay resolution in staggered PRT technique. *J. Atmos. Oceanic Technol.*, **20**, 673-684.
- Sirmans, D., D. Zrnić, and B. Bumgarner, 1976: Extension of maximum unambiguous Doppler velocity by use of two sampling rates. *Preprints 17<sup>th</sup> Conf. on Radar Meteorology*, Seattle, WA, Amer. Meteor. Soc., pp. 23-28.
- \_\_\_\_\_, and W. Bumgarner, 1990: Velocity estimate bias due to range overlaid echoes. *Operational Support Facility internal report*, November, 1990.
- \_\_\_\_\_, 1999: Note on spectrum width calculation in the WSR-88D and recommended software changes. *Operational Support Facility internal report*, February, 1998.
- Torres, S. M. and Y. Dubel, 2004: Design, Implementation, and demonstration of a staggered PRT algorithm. *J. Atmos. Oceanic Technol.*, **21**, 1389-1399
- \_\_\_\_\_, S., D. Zittel and D. Saxion, 2009: Update on deployment of staggered PRT for the NEXRAD network. *Preprints 25<sup>th</sup> Conf. on IIPS for Meteorology, Oceanography, and Hydrology*, Phoenix, AZ, Amer. Meteor. Soc.
- Zrnić, D. and P. Mahapatra, 1985. Two methods of ambiguity resolution in pulse Doppler weather radars. *IEEE Trans. Aerosp. Electron. Syst.*, **21**, 470-483.

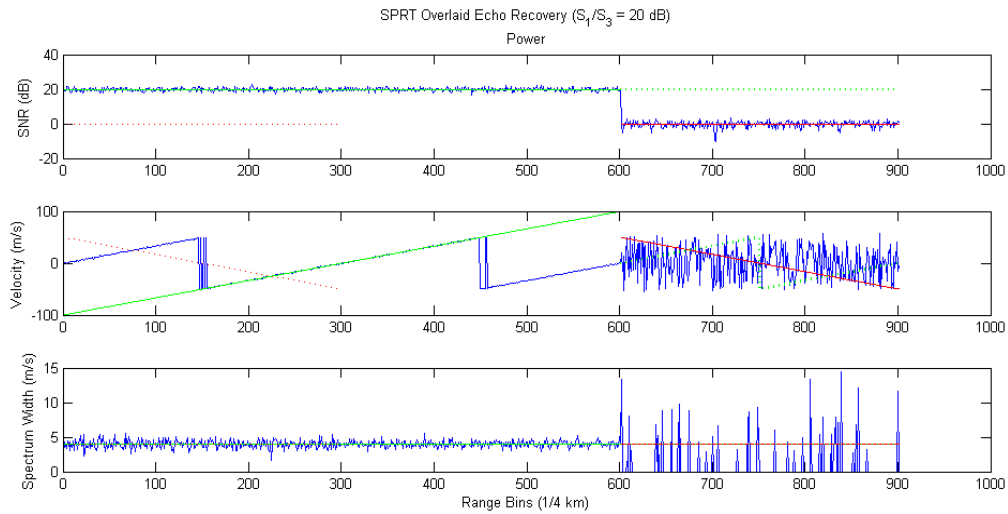


**Figure 4. SPRT overlaid echo recovery with a power ratio of 20 dB.**

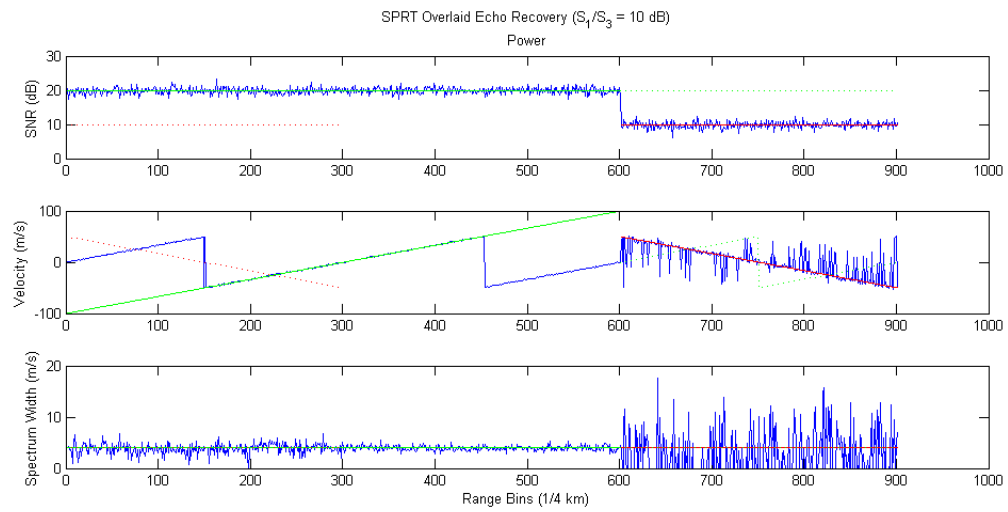


**Figure 5. SPRT overlaid echo recovery with a power ratio of 10 dB.**

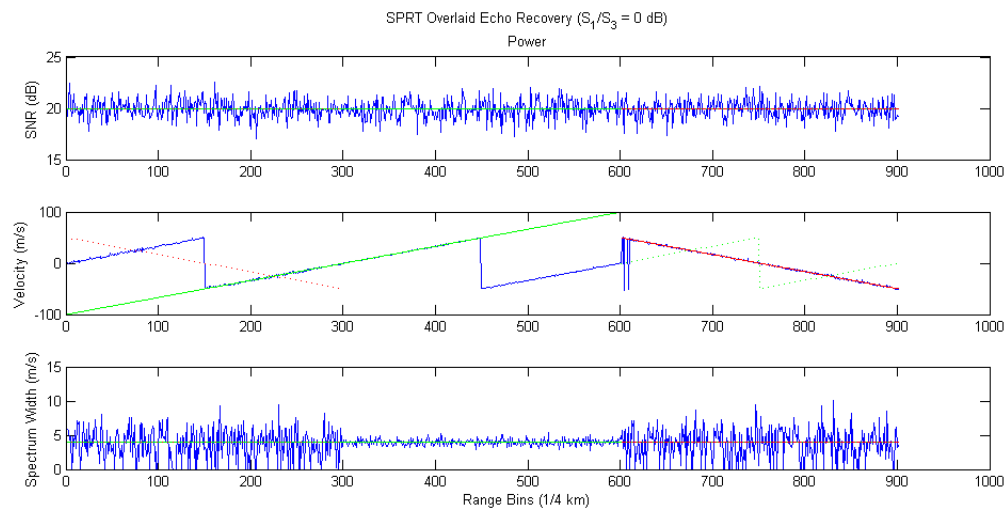


**Figure 6. SPRT overlaid echo recovery with a power ratio of 0 dB.**

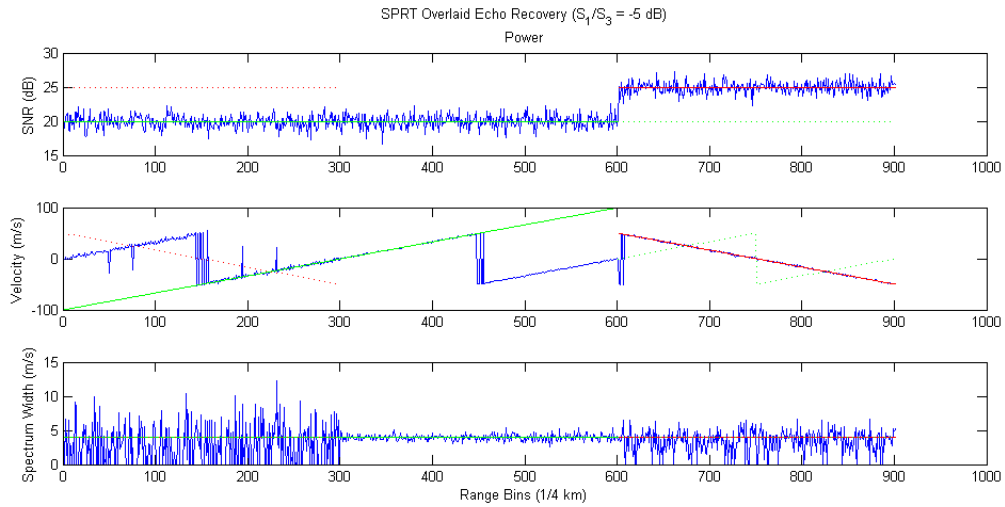


Figure 7. SPRT overlaid echo recovery with a power ratio of -5 dB.

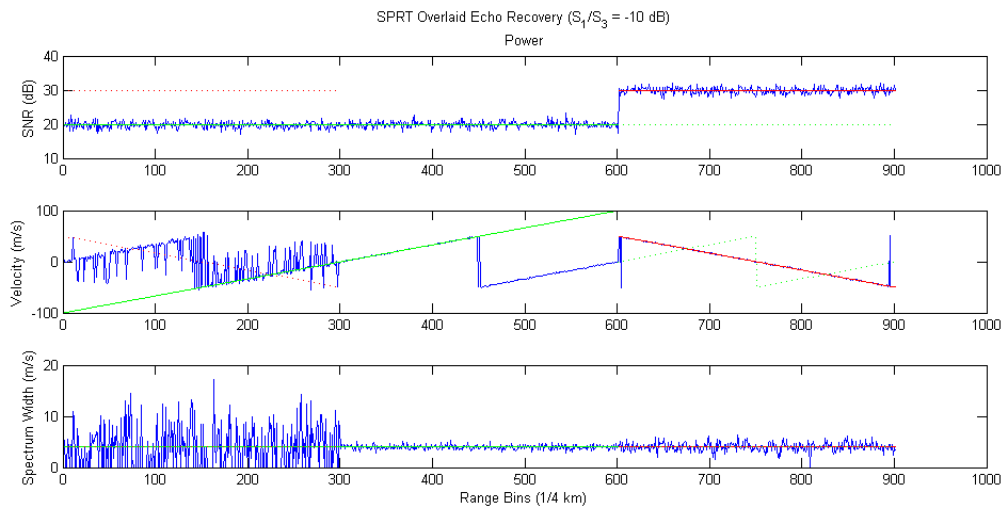


Figure 8. SPRT overlaid echo recovery with a power ratio of -10 dB.

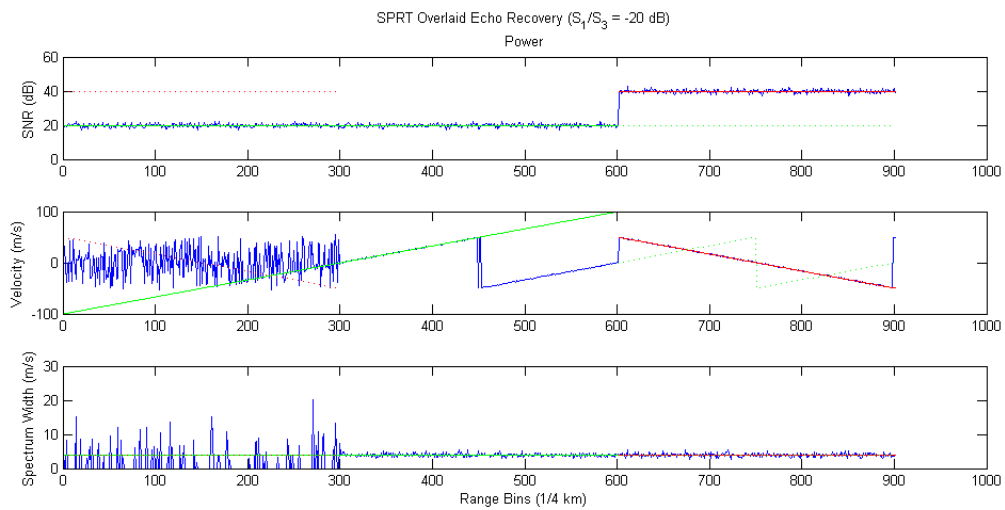


Figure 9. SPRT overlaid echo recovery with a power ratio of -20 dB.

## P5.10 GENERALIZED SZ PHASE CODES TO MITIGATE RANGE AND VELOCITY AMBIGUITIES

Sebastian M. Torres<sup>1,2</sup> and Dusan S. Zrnić<sup>2</sup>

<sup>1</sup>Cooperative Institute for Mesoscale Meteorological Studies, The University of Oklahoma and

<sup>2</sup>NOAA/OAR National Severe Storms Laboratory  
Norman, Oklahoma

### 1. INTRODUCTION

It is well known that for Doppler radars transmitting uniformly spaced pulses there is a coupling between the maximum unambiguous range and velocity. That is, one can only be increased at the expense of a proportional decrease of the other. Because this fundamental limitation hinders observation of severe weather phenomena, the Radar Operations Center of the US National Weather Service has undertaken the implementation of evolutionary signal processing techniques to mitigate the effects of velocity and range ambiguities on the NEXRAD network. The first technique that was targeted for operational implementation is referred to as Sachidananda-Zrnić (SZ)-2 and has been in use since 2007.

The SZ-2 algorithm is based on systematic phase coding of the transmitted pulses with the SZ(8/64) code (Torres 2005). Although the SZ(8/64) phase code results in a very effective recovery of weak overlaid signals, it leads to optimum performance only if the overlaid signal trip numbers differ by one. However, in the current operational implementation of the SZ-2 algorithm, overlaid signals can exhibit trip differences of up to three.

This paper introduces a family of systematic phase codes of the form SZ( $n/64$ ). A closer look into the performance of these generalized codes reveals a number of omissions in the early research work. Further, no single code is optimum for all overlay cases, and, surprisingly, the best overall phase code in the SZ family is not the SZ(8/64).

### 2. THE PHASE CODING TECHNIQUE

In the phase coding technique, the transmitted pulses are phase shifted using a systematic code sequence given by  $\psi(m)$ , where  $m = 0, 1, \dots, M-1$ . If received echo samples are multiplied by  $\exp[-j\psi(m-k+1)]$ , intrinsic phases of the signal from trip  $k$  are restored. Consequently, the  $k$ -trip signal is made coherent and out-of-trip overlaid signals are phase-modulated by the code  $\psi(m-k+1) - \psi(m-k+1)$ , where  $k'$  is the trip number of the overlaid signal. In general, any one of the overlaid trip signals can be cohered leaving the rest modulated by different codes. This is the fundamental principle behind these techniques.

### 2.1. SZ Phase Codes

Sachidananda and Zrnić (1999) proposed the SZ phase code as a better alternative to random codes (e.g., Laird 1981). SZ phase coding is similar to random phase coding except that the transmitted pulses are phase-modulated with a systematic code consisting of  $M$  phases that repeat periodically. These codes exhibit properties that make them attractive for the separation of overlaid signals in the spectral domain. That is, if the received signal is cohered for a given trip, the spectra of all out-of-trip echoes are split into evenly spaced replicas and have zero lag-one autocorrelation. Hence, out-of-trip echoes do not bias the mean Doppler velocity estimate of the coherent signal. Once the velocity is recovered for the strong-trip, the coherent signal is notched out such that the two least contaminated “replicas” of the out-of-trip (i.e., the weak trip) echo remain. These two replicas are sufficient to reconstruct (or “recohere”) the weak-trip echo and recover its mean Doppler velocity. From the family of SZ( $n/M$ ) codes, the SZ(8/64) code was selected for NEXRAD as it gives the best performance in terms of recovery of overlaid signals that are separated by one trip (Sachidananda et al. 1998).

### 2.2. The SZ-2 Algorithm

Recovery of strong and weak trip overlaid signals can proceed in a stand-alone manner (referred to as the SZ-1 algorithm) or with the aid of an extra scan at the same elevation angle using a long pulse repetition time (PRT) (referred to as the SZ-2 algorithm). Although the latter results in longer acquisition times due to the extra scan, long-PRT data provides non-overlaid power information that is essential in the determination of the location and strength of overlaid trips for the short-PRT scan. Having the long-PRT information available makes the SZ-2 algorithm computationally simpler and more effective than its stand-alone counterpart. Whereas the long-PRT data provides the reflectivity free of range ambiguities, the short-PRT data is used to compute Doppler velocities associated with the two strongest overlaid signals.

The SZ-2 algorithm, which has been implemented on the US network of weather surveillance radars since the Spring of 2007 (Saffle et al. 2007), incorporates a set of censoring rules to maintain data quality under situations that preclude the recovery of one or more overlaid echoes (Saxion et al. 2007, Ellis et al. 2005). Meteorological data displays characterize this failure by encoding those range locations where overlaid powers

---

Corresponding *author address*: Sebastian M. Torres, NSSL, 120 David L. Boren Blvd., Norman, OK 73072; email: Sebastian.Torres@noaa.gov

are present with a purple color, normally referred to as the “purple haze”.

### 3. GENERALIZED PHASE CODES

As mentioned before, the SZ-2 algorithm is based on the SZ(8/64) phase code, which was deemed optimum in the early stages of this project. However, the methodology used to make this determination did not consider overlay situations with trip differences of more than one. With the current implementation of the SZ-2 algorithm, overlaid signals can exhibit trip differences of one, two, or three. Hence, it is natural to question whether the assessment done using only one overlay case still holds when we allow other overlay cases to occur. The main motivation for this work is the need to determine which phase codes might lead to better performance for overlay cases not considered before. In addition, we would like to explore the ability of other phase codes to extend the recovery of weak overlaid echoes to more trips, since the operational SZ-2 algorithm only provides recovery of weak overlaid signals up to four trips. Although this is not a limitation within the NEXRAD network, other radar systems, especially those operating at shorter wavelengths, might benefit from an approach that extends the recovery of overlaid echoes to more trips.

Herein, we look at switching codes in the SZ( $n/64$ ) family, where  $n$  is a positive integer. These are of the form

$$\psi(m) = -\sum_{p=0}^m \frac{n\pi p^2}{64}, \quad m = 0, 1, 2, \dots \quad (1)$$

These codes are attractive because they exploit the WSR-88D phase shifter resolution to the maximum. That is, because the WSR-88D phase shifter is controlled with 7 bits, its phase resolution is  $\pi/64$ . Hence, the phase shifter can realize any phase that is an integer multiple of  $\pi/64$ , and this is the exact same form of the code given in (1).

As with the SZ(8/64) code, the modulation codes for the family of SZ( $n/64$ ) codes are different for different overlay cases. Without loss of generality, assume that  $k = 1$  (the first trip is coherent) and  $t = k' - k$  is the trip difference between the modulated and coherent overlaid signals. Hence, the modulation code for an overlay trip difference  $t$  is given by

$$\phi(m) = \psi(m-t) - \psi(m) = \frac{n\pi}{64} \sum_{l=0}^{t-1} (m-l)^2 \quad (2)$$

which for  $t = 1$  (i.e.,  $k' = 2$ , which was the only case analyzed in the previous work) reduces to

$$\phi(m) = \frac{n\pi m^2}{64}. \quad (3)$$

#### 3.1. Periodicity and performance of SZ( $n/64$ ) codes

In general, the performance of systematic phase codes is measured by the ability of recovering the velocity of the weaker overlaid signal after removing most of the stronger signal. In Sachidananda et al. (1998), it was established that recovery of weak-trip

velocity is possible from at least two replicas of the modulated weak-trip signal. Thus, a contradiction arises. On one hand, a modulation code producing more replicas (i.e., one with shorter periodicity) allows for a wider processing notch filter (PNF) and therefore a more efficient suppression of the strong-trip signal. On the other hand, a modulation code producing fewer replicas (i.e., one with longer periodicity) would result in more accurate weak-trip velocity estimates since less overlap of the weak-trip replicas occurs. It would seem that the periodicity (or the number of replicas) of the modulation code determines its performance in terms of weak-trip velocity recovery. However, it can be shown with a simple counterexample that the performance of these codes is not dictated solely by their periodicity.

Let's first consider the codes SZ(8/64) and SZ(56/64). The spectra of the corresponding modulation codes are shown in Fig. 1, where it is evident that both would lead to the same number of replicas. The performance of these codes in terms of weak-trip velocity recovery is shown in Fig. 1 as the standard deviation of velocity estimates on the power-ratio/strong-trip spectrum width plane for a weak-trip spectrum width of 4 m/s and high signal-to-noise ratios. Evidently, these two codes have the same periodicity and the same performance.

Consider now the codes SZ(8/64) and SZ(24/64). Again, the modulation code spectra and performance charts are shown below in Fig. 2, where it is now obvious that same periodicity does not lead to same performance.

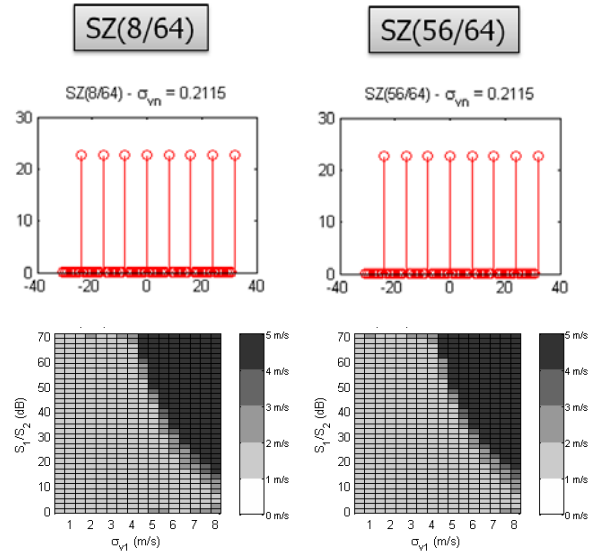


Fig. 1. (top) Spectra of the SZ(8/64) and SZ(56/64) modulation codes. (bottom) Statistical performance of weak-trip recovery corresponding to the SZ(8/64) and SZ(56/64) codes. The plots show the standard deviation of weak-trip velocity estimates as a function of the strong-to-weak trip power ratio and the strong-trip spectrum width. Strong and weak trips differ by one.

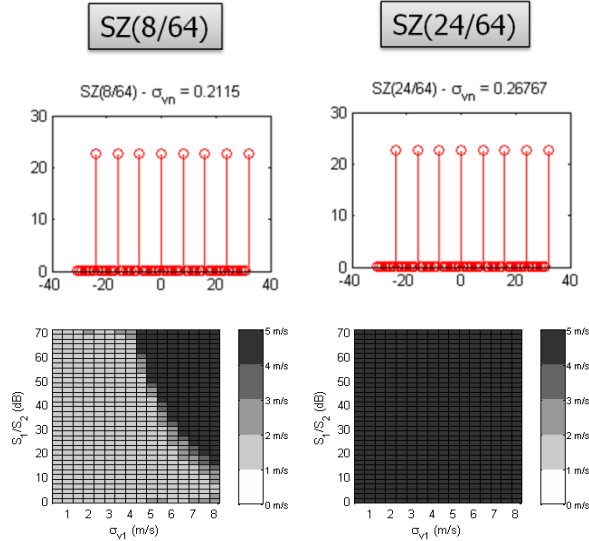


Fig. 2. Same as Fig. 1 for the SZ(8/64) and SZ(24/64) modulation codes.

Although the periodicity of the modulation code plays an important role in the performance of these codes, it is not enough to predict it. The reader might be wondering what is different between the two examples presented above. It is important to remember that weak-trip velocities are recovered after applying the PNF and re-cohering the weak trip signal. So it would make sense to look at the spectra of the modulation codes after the same process. Fig. 3 shows the spectra of the modulation codes after the SZ-2 process for the codes in the examples above. Note that the codes with the same performance have the same code spectrum after notching and re-cohering. This is not the case for the SZ(24/64) code, which, as shown above, does not exhibit the same performance.

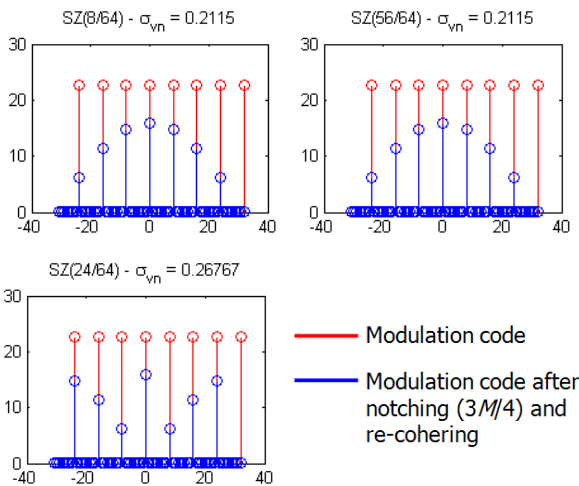


Fig. 3. Spectra of the SZ(8/64), SZ(56/64), and SZ(24/64) modulation codes (red) and same after notching and re-cohering (blue).

Therefore, not all codes with the same period (i.e., leading to the same number of modulated replicas) exhibit the same performance in terms of weak-trip velocity recovery. The performance of a given code depends on the structure of the sidebands after notching and re-cohering. But it is not clear at this time if there is a way to predict the performance of a given code based on its sideband structure.

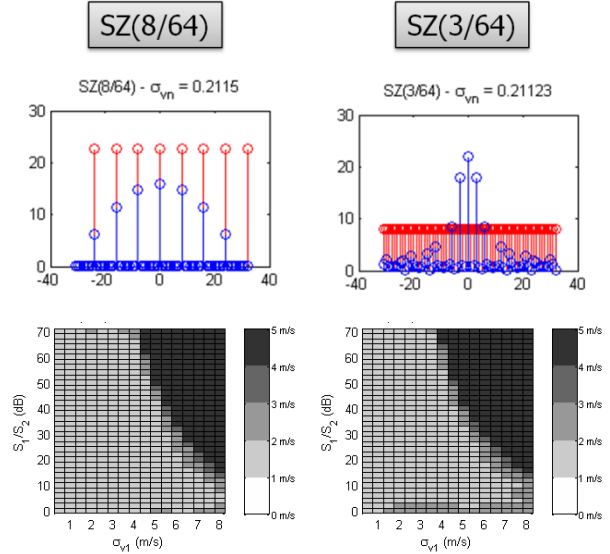


Fig. 4. Same as Fig. 1 for the SZ(8/64) and SZ(3/64) modulation codes.

The previous examples showed codes with the same periodicity and different performance. Are there codes with the same performance but different periodicity? Consider now the SZ(8/64) and SZ(3/64) codes. These codes have a periodicity of 8 and 64, respectively. Although the periodicity of these codes is very different, their performance in terms of weak-trip velocity recovery is very similar! (see Fig. 4) This example reinforces the idea that the performance of systematic phase codes is not uniquely related to the number of spectral “replicas” (or periodicity) of the code. In other words, as the modulation code exhibits more “replicas”, the performance in terms of weak-trip velocity recovery does not necessarily get worse as previously suspected. Another consideration is that the PNF width must be tailored to the specific code and cannot be designed with the idea of retaining spectral replicas since this concept of “replicas” stops working for longer code periodicities (i.e., when the number of “replicas” increases with respect to the normalized spectrum width of the modulated signal).

### 3.2. Performance of SZ(n/64) codes

Next, simulations are used to evaluate the performance of this family of codes in a systematic way. Once again, performance is gauged in terms of weak-trip velocity recovery, which depends on the switching

code and the PNF width. The performance for any given code-PNF width combination is quantified in terms of the size of the “recovery region”. That is, on the power ratio vs. strong-trip spectrum width plane, we count the number of cases for which the standard deviation of weak-trip velocity estimates is less than 2 m/s for a true weak-trip spectrum width of 4 m/s (see Fig. 5). Note that the relaxed 2 m/s error benchmark reflects the recently established requirements for weak-trip velocity estimates obtained with the SZ-2 algorithm.

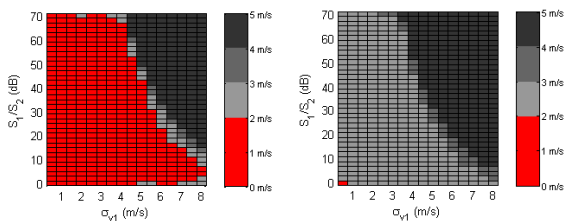


Fig. 5. Examples of good (left panel) and bad (right panel) phase code-PNF width combinations in terms of weak-trip recovery.

The simulation tested all codes in the  $SZ(n/64)$  family with two overlaid echoes and trip differences ranging from one to four. For each case, the PNF width was varied from 25% to 75% of the Nyquist co-interval. Signal parameters were varied as follows: the strong-to-weak signal overlaid ratio from 0 to 70 dB in steps of 2 dB; the strong-trip spectrum width from 0.5 to 8 m/s in steps of 0.5 m/s, and the overlaid signal velocities were chosen randomly in the Nyquist co-interval for each realization. The number of samples was  $M = 64$ , the weak-trip spectrum width was fixed at 4 m/s, the radar frequency was  $f = 2.8$  GHz, the PRT was  $T = 780 \mu\text{s}$ , and the signal-to-noise ratio was high (more than 20 dB).

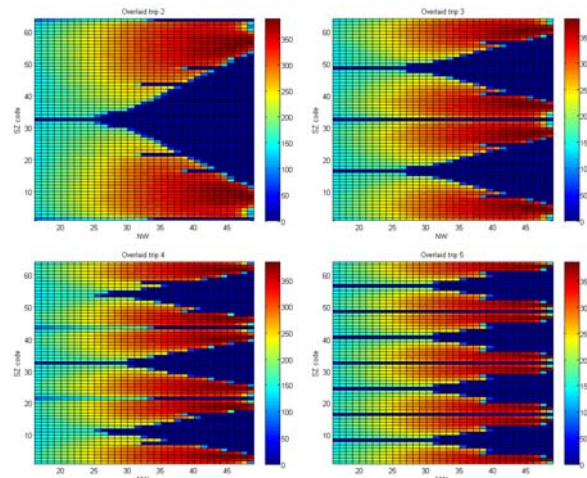


Fig. 6. Performance of  $SZ(n/64)$  codes for different PNF widths ( $NW$ ) and overlaid cases with trip differences of 1 (top left), 2 (top right), 3 (bottom left), and 4 (bottom right). “Warmer” colors represent better performance.

The performance for every phase code-PNF width combination is plotted in Fig. 6 for overlaid signals with

1, 2, 3, and 4 trip differences. Larger numbers (“warmer” colors) represent better performance (i.e., a larger weak-trip velocity recovery region). Many interesting properties can be inferred from these plots. For example, the vertical symmetry about  $n = 32$  implies that codes of the form  $SZ(n/64)$  and  $SZ[(64-n)/64]$  are equivalent in terms of performance. Also, it is easy to spot codes that are not suitable for weak-trip velocity recovery, such as the  $SZ(32/64)$ , which has a null recovery region for all PNF widths and overlay cases.

The performance of the SZ-2 algorithm can be obtained from Fig. 6 by looking at the rows with  $n = 8$ . For an overlaid trip difference of one, two, and three, the SZ-2 PNF width is set at 48, 32, and 32, respectively. As expected, for an overlaid trip difference of four, no PNF width leads to recovery of the weak-trip velocity. Note that, as introduced earlier,  $SZ(8/64)$  is not the optimum phase code for all overlay situations. The question arises then as to which codes are the best for each overlay case. Table 1 lists the best code-PNF width combinations for each overlay case and compares their performance to the current SZ-2 algorithm. For overlaid signals with one trip difference, the best code is  $SZ(56/64)$ , which is statistically equivalent to the familiar  $SZ(8/64)$  (symmetry property). For other overlay cases, the optimum code-PNF width combinations can extend the size of the recovery region by more than 50%! However, there is no single switching code that is optimum for all overlaid cases.

$t$	$n$	$SZ(n/64)$		$SZ(8/64)$		Improv.
		NW	SRR	NW	SRR	
1	56	48	388	48	382	2
2	28	47	384	32	298	29
3	3	47	384	32	246	56
4	62	47	386	N/A	0	$\infty$

Table 1. Comparison of best  $SZ(n/64)$  codes-PNF width combinations and SZ-2 for different overlay cases. The table lists the PNF width ( $NW$ ), the corresponding size of the weak-trip recovery region ( $SRR$ ) and the improvement with respect to the SZ-2 algorithm.

$t$	$SZ(4/64)$		$SZ(8/64)$		Improv.
	NW	SRR	NW	SRR	
1	41	343	48	382	-10
2	47	382	32	298	28
3	43	363	32	246	48
4	35	310	N/A	0	$\infty$

Table 2. Same as Table 1 but comparing single-code best combinations and SZ-2 for different overlay cases.

Although the performances of the best combinations are appealing, it is not practical to consider different phase codes for different overlay cases. Hence, we are interested in finding the best set of combinations based on a single phase code. These are listed in Table 2, where the phase code with best overall performance is  $SZ(4/64)$ . For a trip difference of 1, the  $SZ(4/64)$  code is about 10% worse than the

operation SZ(8/64). This is expected since the SZ(8/64) was chosen for this situation. However, for all other situations, SZ(4/64) results in significant improvements over the SZ(8/64). It is important to mention that the determination of single-code best combinations was done considering overlay cases with trip differences of 1, 2, and 3 only. A trip difference of 4 is not possible with the WSR-88D PRTs. Still, the SZ(4/64) code can handle the overlay case with a trip difference of 4, which might be of interest for shorter-wavelength radars, such as the TDWRs.

#### 4. CONCLUSIONS

This paper introduced a family of systematic phase codes of the form SZ( $n/64$ ). A closer look into the performance of these generalized codes revealed a number of omissions in the early research work. Further, no single code is optimum for all overlay cases, and, surprisingly, the best overall phase code in the SZ family is not the SZ(8/64), which is currently used operationally on the NEXRAD network.

This analysis is by no means comprehensive. However, these preliminary results justify further exploration of generalized phase codes. For example, performance should be assessed using the actual levels and types of phase errors encountered operationally on the NEXRAD network, which have not been measured systematically. Also, we plan to complement a simulation-based study with the analysis of multiple real-data cases collected with the KOUN research radar.

In summary, this work is not complete yet but has the potential to lead to an even greater improvement with respect to previous "legacy" algorithms to effectively mitigate range and velocity ambiguities on the US network of weather surveillance radars.

#### ACKNOWLEDGMENT

This conference paper was prepared by Sebastián Torres and Dusan Zrnić with funding provided by NOAA/Office of Oceanic and Atmospheric Research under NOAA-University of Oklahoma Cooperative Agreement #NA17RJ1227, U.S. Department of Commerce. The statements, findings, conclusions, and recommendations are those of the author(s) and do not necessarily reflect the views of NOAA or the U.S. Department of Commerce.

#### REFERENCES

- Ellis, S. M., M. Dixon, G. Meymaris, S. Torres, and J. Hubbert, 2005: Radar range and velocity ambiguity mitigation: Censoring methods for the SZ-1 and SZ-2 phase coding algorithms. Preprints, *21st International Conf. on Interactive Information and Processing Systems (IIPS) for Meteorology, Oceanography, and Hydrology*, San Diego, CA, Amer. Meteor. Soc., Paper 19.3.
- Laird, B. G., 1981: On ambiguity resolution by random phase processing. Preprints, *20th Conf. on Radar Meteorology*, Boston, MA, Amer. Meteor. Soc., 327–331.
- Sachidananda, M., D. S. Zrnić, R. J. Doviak, and S. M. Torres, 1998: Signal design and processing techniques for WSR-88D ambiguity resolution, Part 2. NOAA/NSSL Report.
- Sachidananda, M. and D. S. Zrnić, 1999: Systematic phase codes for resolving range overlaid signals in a Doppler weather radar, *J. Atmos. Oceanic Technol.*, **16**, 1351–1363.
- Saffle, R. E., M. J. Istok, and G. Cate, 2007: NEXRAD product improvement – update 2007. Preprints, *23rd International Conference on Interactive Information and Processing Systems (IIPS) for Meteorology, Oceanography, and Hydrology*, San Antonio, TX, Amer. Meteor. Soc., Paper 5B.1.
- Saxion, D. S., R. D. Rhoton, R. L. Ice, D. A. Warde, O. E. Boydston, S. Torres, G. Meymaris, and W. D. Zittel, 2007: New science for the WSR-88D: implementing a major mode on the SIGMET RVP8. Preprints, *23rd International Conference on Interactive Information and Processing Systems (IIPS) for Meteorology, Oceanography, and Hydrology*, San Antonio, TX, Amer. Meteor. Soc., Paper P2.9.
- Torres, S., 2005: Range and velocity ambiguity mitigation on the WSR-88D: Performance of the SZ-2 phase coding algorithm. Preprints, *21st International Conf. on IIPS*, San Diego, CA, Amer. Meteor. Soc., Paper 19.2.